Thermal Transport in Polymer Colloidal Assemblies

DISSERTATION

Zur Erlangung des Grades eines Doktors der Naturwissenschaften
(Dr. rer. nat.)
im Promotionsfach Chemie

Fakultät für Biologie, Chemie und Geowissenschaften
der Universität Bayreuth

Vorgelegt von
Fabian A. Nutz
Geboren in Tegernsee

Bayreuth, 2017

Die vorliegende Arbeit wurde in der Zeit von April 2014 bis September 2017 in Bayreuth am Lehrstuhl Physikalische Chemie I unter Betreuung von Herrn Professor Dr. Markus Retsch angefertigt.

Vollständiger Abdruck der von der Fakultät für Biologie, Chemie und Geowissenschaften der Universität Bayreuth genehmigten Dissertation zur Erlangung des akademischen Grades eines Doktors der Naturwissenschaften. (Dr. rer. nat.)

Dissertation eingereicht am: 13.09.2017

Zulassung durch die Promotionskommission: 28.08.2018

Wissenschaftliches Kolloquium: 28.03.2018

Amtierender Dekan: Prof. Dr. Stefan Peiffer

Prüfungsausschuss:

Prof. Dr. Markus Retsch (Erstgutachter)
Prof. Dr. Georg Papastavrou (Zweitgutachter)
Prof. Dr. Peter Strohriegl (Vorsitz)
Prof. Dr. Sven Hüttner

Moni & Toni

Marco, Julia, Sasha & Kian

Sandra

Contents

Danksagung

Bevor sich diese Arbeit dem eigentlichen Thema zuwendet, möchte ich die nächsten Zeilen dazu nutzen, um mich bei Allen zu bedanken, die mich beim Anfertigen dieser Arbeit unterstützt haben.

An erster Stelle bedanke ich mich bei meinem Doktorvater Prof. Markus Retsch für die Möglichkeit diese Arbeit in seinem Arbeitskreis anzufertigen. Besonders möchte ich mich hier für die interessante Themenstellung sowie das offene und menschliche Betreuungsverhältnis bedanken. Sie hatten zu jeder Zeit ein offenes Ohr für mich und waren wirklich immer für meine, mehr oder weniger wichtigen, Fragen erreichbar. Das habe ich nie als selbstverständlich betrachtet. Vor allem aber die Vielzahl an Aktivitäten mit dem Arbeitskreis außerhalb der Uni rechne ich ihnen hoch an. Ganz herzlich will ich mich auch für das Ermöglichen zahlreicher Auslandsreisen sowie die jährlichen Ausflüge mit der gesamten Gruppe nach Freiburg bedanken. für mich waren diese Reisen immer ein Highlight. Weiterhin werde ich diverse Paperparties und Gruppenausflüge in guter Erinnerung behalten. Vielen lieben Dank für alles!

Ebenfalls bedanken möchte ich mich bei Elisabeth Düngfelder und Jenny Hennessy für die (nötige) Hilfe bei verschiedensten Anträgen, Bestellungen etc. Es war immer wieder schön, bei euch im Sekretariat vorbei zu kommen.

Ich möchte mich auch bei allen jetzigen und ehemaligen Mitgliedern der Physikalischen Chemie I für die tolle Zeit im Labor und den freundschaftlichen Umgang bedanken. Hervorheben möchte ich vor allem die zahlreichen Grill- und Kochabende, optional verlängert mit Salsa im Glashaus.

Ich bedanken mich auch sehr herzlich bei allen Mitgliedern der Retsch Gruppe, vor allem bei meinen Labor- und Büropartnern Pia, Anna, Alex, Bernd, Patrick sowie Christian für die hilfsbereite und freundschaftliche Arbeitsatmosphäre. Mir hat es immer Spaß gemacht mit euch zu arbeiten und auch abseits der Uni Zeit mit euch zu verbringen. Ich werde mich ich immer gerne an die Zeit mit euch erinnern!

Zuletzt geht ein ganz besonders großer Dank an meine Familie, vor allem an meine Eltern. Vielen Dank für die jahrelange Unterstützung während meines Studiums und meiner Promotion. Ohne euch wär‘s schlicht nicht gegangen!

Vielen Dank!

Summary

The dissipation of heat is a crucial parameter e.g. in the field of modern electronic devices and circuits, caused by an ongoing miniaturization and concomitant increase in energy density. The nanostructuring of matter represents a promising route to address these arising challenges. This necessitates a full understanding of heat transport in nano-, and mesoscale materials, wherefrom it is possible to develop novel concepts for specific device design. Therefore, in this thesis, polymer colloidal crystals are used as a versatile platform to study heat transport in nanostructured materials fundamentally. The highly-defined structure, combined with the possibility to control the thermal properties of these structures, allows studying thermal transport systematically, as well as to develop novel concepts for thermally functional materials. The investigated system is based on monodisperse polymer particles, consisting of either polystyrene or statistic copolymers of acrylate monomers. The chosen monomers allow to control the size, as well as to adjust the glass transition temperature T_g of the obtained particles, respectively. These particles can self-assemble into open-porous nanostructures, possessing pore sizes in the range of several tens up to hundreds of nanometers. The thermal transport through these colloidal structures is governed by the high interface density and the small interface areas between adjacent particles, serving as geometrical constrictions for heat to travel through the material.

It is first demonstrated that the investigated polymer colloidal assemblies show a comparatively low thermal conductivity at still high densities. Additionally, these assemblies are hardly affected by the surrounding atmosphere due to the small pore sizes in the range of the mean free path of the gas-phase. Furthermore, the particle-particle interface can be manipulated by inducing dry sintering of the particles, based on the glass transition temperature T_g of the polymer particles. During the sintering, the contact areas enlarge and the porosity vanishes, leading

to an almost *three-fold increase in the thermal conductivity* during film formation. Secondly, the dry sintering is further studied in more detail by the time-dependent evolution of the thermal transport properties of polymer assemblies at temperatures near T_g. Combining time-dependent thermal transport characterization and UV-vis spectroscopy, it is possible to separate volume- and interface-driven effects. This allows to extract apparent activation energies for the film formation process by a size-independent and label-free characterization technique. Thirdly, the unique increase of the thermal conductivity by exceeding T_g is used to specifically tailor the temperature-dependent thermal conductivity of the particle assemblies. Taking advantage of various established assembly methods, it is shown how to fabricate crystalline, binary co-assemblies from particles possessing different T_gs, as well as multilayer structures, in which every layer consists of one specific T_g. This enables to i) adjust the transition at the desired temperature, ii) tune the transition range between two temperatures, iii) introduce multiple discrete transition steps, iv) control the degree of transition change, as well as to combine these approaches as desired. Finally, the influence of ordering in colloidal assemblies is demonstrated by investigating the thermal transport properties of binary assemblies from various mixing ratios of two differently sized particles. The thermal conductivity of disordered, binary assemblies is found to be reduced experimentally by roughly 40 %. Using complementary molecular dynamics and finite element modeling, it is demonstrated that this reduction is not only based on the reduced pathways for heat to travel through the structure due to the random packing of the particles, but additionally depends on a broadening of the number of next neighbor distribution in the high number region. This can be rationalized with the formation of particle clusters, leading to an even further geometrical extension of the thermal path and thus, to a further reduction of the thermal conductivity.

This thesis provides novel and conceptual insights into thermal transport in particulate systems. It specifically demonstrates the significant influence of nanoscopic constriction to the effective thermal transport properties. Building on this concept, clear structure-property relationships could be established, which will be of high value for the development of nanostructured materials possessing tunable thermal transport properties.

Zusammenfassung

Das Abführen von Wärme ist ein entscheidender Parameter, z. B. auf dem Gebiet moderner elektronischer Bauteile und Schaltungen. Dies ist vor allem auf eine fortlaufende Miniaturisierung und gleichzeitige Erhöhung der Energiedichte dieser Materialien zurückzuführen. Das Nanostrukturieren von Materialien eröffnet eine vielversprechende Möglichkeit diesen neuen Herausforderungen zu begegnen. Daraus ergibt sich die Notwendigkeit den Wärmetransport in nano- und mesoskaligen Materialien vollständig zu verstehen, um neuartige Konzepte für eine gezielte Materialsynthese abzuleiten. Daher werden in dieser Arbeit polymere Kolloidkristalle als vielseitige Plattform verwendet um den grundsätzlichen Wärmetransport in nanostrukturierten Materialien zu untersuchen. Die hoch definierte Struktur ermöglicht die systematische Untersuchung des thermischen Transports durch diese Materialien. Weiterhin eröffnet die Kontrolle über die thermischen Eigenschaften dieser Strukturen anhand der Partikelsynthese und der Partikelassemblierung, die Möglichkeit neue Konzepte für thermisch funktionelle Materialien zu entwickeln. Das untersuchte System basiert auf monodispersen Polymerpartikeln, die entweder aus Polystyrol oder statistischen Acrylat-copolymeren bestehen. Die gewählten Monomere erlauben es, die Größe sowie die Glasübergangstemperatur der erhaltenen Partikel gezielt einzustellen. Diese Partikel selbst-assemblieren in offenporöse Nanostrukturen mit Porengrößen im Bereich von einigen zehn bis zu hunderten Nanometern. Der Wärmetransport durch diese kolloidalen Strukturen wird durch die hohe Grenzflächendichte und die Größe dieser Grenzflächen zwischen benachbarten Partikeln dominiert. Die Partikel-Partikel Grenzflächen verhalten sich wie geometrische Verengungen für den Wärmefluss. Es wird zunächst gezeigt, dass die untersuchten Polymer-Kolloidkristalle eine vergleichsweise geringe Wärmeleitfähigkeit bei vergleichbar hohen Dichten aufweisen. Aufgrund

der geringen Porengrößen im Bereich der mittleren freien Weglänge der vorliegenden Gasphase wird der Wärmetransport durch diese Strukturen nur wenig von der umgebenden Atmosphäre beeinflusst. Weiterhin ist es möglich die Partikel-Partikel-Grenzfläche durch Sintern der Polymerpartikel bei Temperaturen über ihrer Glasübergangstemperatur T_g zu manipulieren. Während des Sinterns vergrößern sich die Kontaktflächen, die Porosität verschwindet, was in einer fast dreifachen, stufenartigen Erhöhung der Wärmeleitfähigkeit während der Filmbildung resultiert. In einem zweiten Schritt wird die zeitabhängige Entwicklung der thermischen Transporteigenschaften polymerer Kolloidkristalle bei Temperaturen nahe T_g untersucht. Durch die Kombination von zeitabhängiger Charakterisierung der thermischen Transporteigenschaften und UV-vis Spektroskopie, ist es möglich volumen- und grenzflächengetriebene Effekte getrennt voneinander zu untersuchen. Das ermöglicht es, apparente Aktivierungsenergien für den Filmbildungsprozess durch eine größenunabhängige und Labelfreie Charakterisierungstechnik zu berechnen. In einem dritten Schritt wird die einzigartige Erhöhung der Wärmeleitfähigkeit während des Sinterns ausgenutzt, um die Temperaturabhängigkeit der Wärmeleitfähigkeit dieser Partikelstrukturen gezielt maßzuschneidern. Mit Zuhilfenahme verschiedener, etablierter kolloidaler Assemblierungsmethoden wird gezeigt, wie man aus Partikeln mit verschiedenen T_gs kristalline, binäre Co-Assemblies sowie mehrschichtige Strukturen herstellt. Dies ermöglicht es, i) den Anstieg auf die gewünschte Temperatur einzustellen, ii) einen kontinuierlichen Anstieg zwischen zwei Temperaturen zu realisieren, iii) mehrere diskrete Übergangsschritte einzuführen, iv) die Höhe des Anstiegs bei einer bestimmten Temperatur zu kontrollieren und diese Einstellmöglichkeiten zu kombinieren. Schließlich wird der Einfluss der Partikelordnung in kolloidalen Strukturen auf deren thermischen Transporteigenschaften anhand von binären Partikelassemblies zweier Partikel mit unterschiedlichen Durchmessern

untersucht. Basierend auf der eingeführten Unordnung zeigen binäre Assemblies eine reduzierte thermische Leitfähigkeit um ~40 %. Mit Hilfe von komplementären Molekulardynamik und Finite-Elemente Simulation wird gezeigt, dass diese Reduktion nicht nur auf eine geringere Anzahl an Partikel-Partikel Kontaktpunkten in diesen Strukturen zurückzuführen ist. Zusätzlich führt eine Verbreiterung der Verteilung der Anzahl der nächsten Partikelnachbarn zu einer weiteren Reduzierung. Dies kann anhand der Bildung von Partikelclustern verstanden werden, die zu einer weiteren, geometrischen Verlängerung der thermischen Weglänge und damit in eine weitere Reduktion der Wärmeleitfähigkeit resultiert.

Diese Arbeit liefert konzeptionelle Einblicke in den thermischen Transport in Partikelsystemen. Sie zeigt den signifikanten Einfluss der nanoskopischen Verengung auf die effektiven thermischen Transporteigenschaften. Auf diesem Konzept können klare Struktur-Eigenschafts-Beziehungen aufgebaut werden, die für die Entwicklung von nanostrukturierten Materialien mit abstimmbaren thermischen Transporteigenschaften von hohem Wert sein werden

Abbreviations and Symbols

2D	two-dimensional
3D	three-dimensional
AA	acrylic acid
AMM	acoustic mismatch model
C_p	specific heat capacity
C_v	volumetric heat capacity
DMM	diffusive mismatch model
fcc	face-centered cubic
FEM	finite element modeling
hcp	hexagonal close-packed
IR	infrared radiation
KPS	potassium peroxodisulfate
LCST	lowest critical solution temperature
MD	molecular dynamics
MFP	mean free path
MMA	methyl methacrylate
n-BA	n-butyl acrylate
NIPAM	n-isopropylacrylamide
nm	nanometer
PS	polystyrene
PSS	styrene sulfonic acid
SAM	self-assembled monolayers
SEM	scanning electron microscopy
SiO_2	siliciumdioxid, silica
T	temperature
TEM	transmission electron microscopy

T_g	glass transition temperature
UV	ultra violet
v.d.W.	van der Waals
v_g	sound velocity
Vis	visible
α	thermal diffusivity
κ	thermal conductivity
ρ	density

Publications and Conference Contributions

Publications

[1] **F. A. Nutz**, P. Ruckdeschel, M. Retsch, J. Colloid Interface Sci., 2015, 457, 96-101. Article.
Polystyrene Colloidal Crystals: Interface Controlled Thermal Conductivity in an Open-Porous Mesoparticle Superstructure.

[2] P. Ruckdeschel, T. Kemnitzer, **F. A. Nutz**, J. Senker, M. Retsch, Nanoscale, 2015, 7 (22), 10059-10070. Article.
Hollow Silica Sphere Colloidal Crystals: Insights into Calcination Dependent Thermal Transport.

[3] **F. A. Nutz** and M. Retsch, Phys. Chem. Chem. Phys., 2017, 19 (24), 16124-16130. Article.
Interfacial and Volumetric Sensitivity of the Dry Sintering Process of Polymer Colloidal Crystals: a Thermal Transport and Photonic Bandgap Study.

[4] **F. A. Nutz**, P. Ruckdeschel, M. Retsch. Review. Submitted.
Thermal Transport in Colloidal Crystals and Assemblies.

[5] **F. A. Nutz** and M. Retsch. Article. Submitted.
Tailor-Made Temperature-Dependent Thermal Conductivity: The Power of Interparticle Constriction.

[6] **F. A. Nutz**, A. Philipp, M. Dulle, M. Retsch. Article. Submitted.
Constricted Thermal Conductivity through Dense Particle Packings with Optimum Disorder.

[7] M. E. J. Mauer, C. Stelling, B. A. F Kopera, **F. A. Nutz**, M. Karg, M. Retsch, S. Förster. Article. Submitted.
Solution-based Fabrication of ordered Particle Arrays for All Two-Dimensional Bravais Lattices.

Conference Contributions

[1] 2016 Conference of the European Colloid and Interface Society, ECIS, Rom, Poster: *„Polymer Colloidal Assemblies: From Film Formation to Order-Disorder Thermal Transport Properties“*

[2] 2016 Makromolekulares Kolloquium Freiburg, Poster: *"Time- and Temperature-Dependent Thermal Transport Properties of n-BA-co-MMA Colloidal Crystals"*

[3] 2015 MRS Spring Meeting and Exhibition Material Research Society, San Francisco, Poster: *„Thermal Transport of a Polystyrene Colloidal Crystal“*

[4] 2015 Summer School: Concepts and Methods of Soft Matter, IRTG Freiburg, Mittelwihr, France, Poster: *„Polymer Colloidal Crystals: Insights in Their Temperature-Dependent Thermal Transport Properties“*

[5] 2015 Bayreuther Polymer Symposium, Poster: *"Time- and Temperature-Dependent Thermal Transport Properties of n-BA-co-MMA Colloidal Crystals"*

1 Motivation

Heat – as physical term describes the energy, exchanged between two systems which reside themselves outside their thermodynamic equilibrium due to a difference in temperature. According to the second law of thermodynamics, heat always flows from the hot to the cold side, until both systems reach their thermal equilibrium. Whereas this behavior is commonly known and appears to be trivial, it has strongly influenced our past developments and is constantly affecting our daily life. The irrevocable behavior of the flow of heat from hot to cold has always been a major concern e.g. for wildlife within the process of adaptation to nature. Animals have steadily been under the constraint to evolve highly insulating furs or feathers to resisted cold temperatures. These adoptions have influenced how fast energy is exchanged between the animal's skin and the ambient environment, enabling the animal to save energy. The property "how fast" thermally energy is exchanged is commonly known as the thermal conductivity. Still, not only animals were forced to adapt to the intrinsically defined direction of the flow of heat, but also human society has been forced to protect itself from energy exchange to the environment, leading to the inhabitation of caves and the fabrication of clothing. Even nowadays, thermal insulation of buildings plays a central role within the construction sector to protect ourselves from undesired energy exchange and thus, to save waste heat and scarce resources.

Today, the focus of current research is not only laid on how to create highly insulating or conducting systems but is more and more narrowed to fabricate novel strategies, which allow to mold the flow of heat as desired and to create space-saving, functional materials. This is based on the ongoing miniaturization of devices and their steadily increasing operation speeds, in combination with an increasing worldwide energy consumption. Whereas dissipation of thermal energy is a crucial parameter e.g. for the efficiency of electronics, the possibility to control the flow of thermal energy may also lead to novel materials possessing unique properties. Several examples exist in literature, already pointing out the great potential of such materials, describing dynamic insulation materials,[1,2] thermal diodes,[3,4] thermal rectifiers[5-7] or thermal memories,[8-10] to name a few. Still, the challenges of controlled thermal transport are active topics of current research, and tremendous effort has been done within the field over the past two decades.[11,12]

Nanostructuring of matter represents a promising route to overcome the challenges of controlled heat transport since it allows to realize functionality in very small dimensions, as well as to manipulate heat on a structural level. Still, the fundamentals of thermal transport in nanostructures need to be fully explored to develop novel concepts for specific material design. Within the field, heat transport is mostly studied within bulk crystalline materials. This originates from the ballistic transport behavior of heat carriers present in such highly ordered materials. Therefrom, it is possible to derive the underlying mechanisms of heat transport and fundamentally manipulate heat transport. To name a short example, by nanostructuring on the right length scale it is possible to introdue thermal band gaps,[13] similar to the concept known for photonics.[14] This can help to mold the flow of heat as desired. However, the realization of full band gap materials is still a great challenge, and up to now thermal band gaps do not cover the whole amount of heat carriers present in the material.[15,16]

In contrast, thermal transport in well-defined mesostructures has only been poorly in the focus of thermal transport studies yet. This is even more surprising since there is a material class which obviously provides several advantages to investigate thermal transport: *Colloidal crystals*. A qualitative overview of the benefits of colloidal assemblies is given in Figure 1.

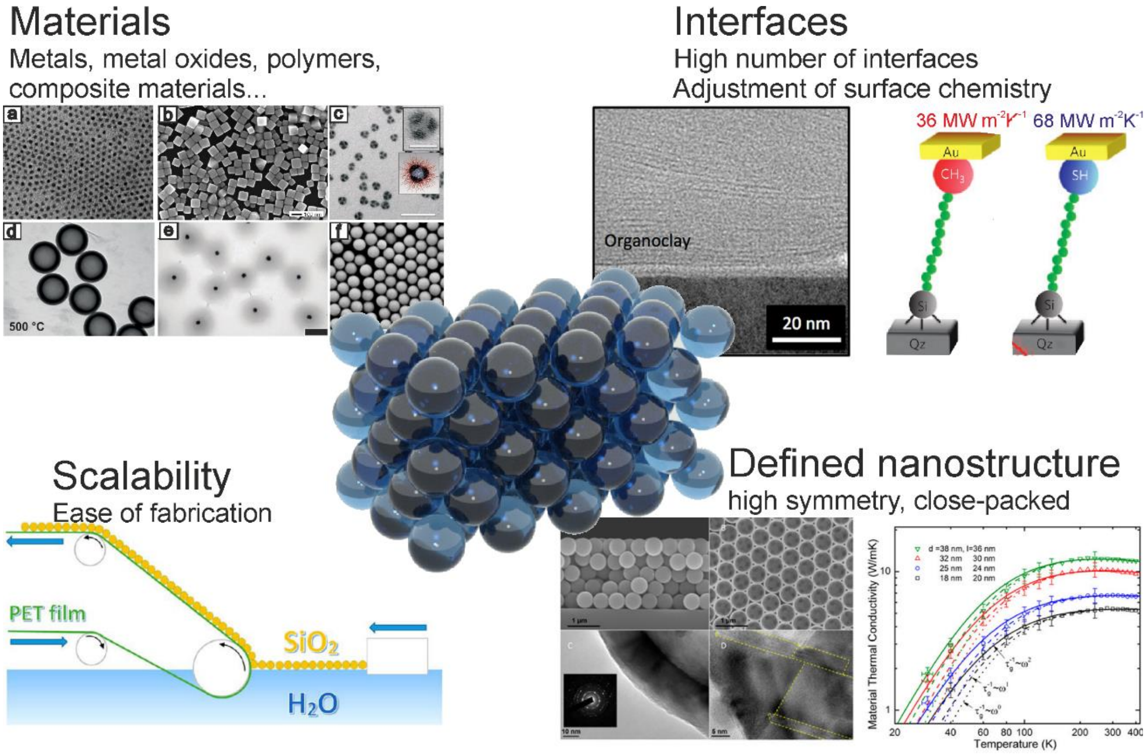

Figure 1: Advantages of a colloidal assembly related to thermal transport. A variety of hard and soft colloids is accessible to fabricate these assemblies.[17-22] Colloidal assemblies possess a high interface density.[23] Interface chemistry is crucial for thermal transport.[24] Based on their highly defined nanostructure, systematic investigations of thermal transport are possible.[25] Colloidal assembly fabrication is easily scalable.[26]

The building blocks of colloidal crystals are *easily accessible* by common synthesis techniques and can be synthesized from *various materials* and in various shapes, allowing to introduce an as desired functionality into the assembly (Chapter 2.1).[27-29] Their *high amount of interfaces* offers the potential of application as ultra-low conducting, solid thin film materials.[23,30,31] Furthermore, these interfaces can be *chemically functionalized*.[32] This is favorable since the thermal interface conductance strongly depends on the surface chemistry of the interfaces (Chapter 2.4).[24,33] Additionally, the size of the particles is variable during the synthesis (Chapter 2.2). This allows addressing a *large length scale* from several hundred nanometers up to a few micrometers. Moreover, their *defined nanostructure* is highly favorable to systematically study the influence of structural parameters on the thermal transport in mesostructured matter.[25,34]

Furthermore, *molding of the heat flux* is potentially possible by manipulating the colloidal structure to realize thermally functional, space-saving materials.

This thesis contributes to the investigations of the thermal transport properties of nanostructured materials, choosing polymer colloidal assemblies as a model platform. The investigated assemblies are fabricated from monodisperse polymer nanospheres. Polymer particles have been chosen as building blocks due to their versatile synthesis, allowing the full control over the size and glass transition temperature of the particles.[35,36] Furthermore, various self-assembly methods are established,[37,38] enabling a precise control over the desired, final colloidal architecture. The particles can self-assemble into open-porous, highly ordered colloidal crystals, possessing a high interface density, small pore size as well as thermally inducible functionality due to the glass transition temperature T_g of the polymer particles. On the one hand, the crystalline packing of the particles allows drawing fundamental structure-property conclusions from the experiments. On the other hand, the thermally inducible dry sintering of the assemblies at temperatures above T_g strongly increases the thermal conductivity of the assembly due to the loss of porosity and interfaces. This behavior can be specifically exploited to tailor the material's temperature-dependent thermal conductivity by advanced colloidal assembly strategies of polymer particles possessing various T_gs. Therefrom, novel concepts can be established to design novel materials specifically. A controllable temperature dependence of the thermal conductivity is of great importance in the field of thermally functional devices e.g. thermal switches and diodes.[3,4,7,39]

2 Fundamentals

2.1 Colloidal Particles and Crystals

Colloidal crystals are commonly assembled from monodisperse building blocks in the size range between one nanometer and several micrometers. Particles of this size are generally termed as colloids. The colloidal domain, therefore, closes the gap from the nanometer to the micrometer scale. Colloidal particles already find application in various fields such as paints, coatings, and packing,[40,41] and can also be found within current research, e.g. as anisotropic clays and minerals or in biology as viruses, proteins, and cells.[42] The colloidal domain is accessible by either top-down or bottom up approaches. Top-down approaches refer to the removal of excess material from a bulk material until the desired size and shape is obtained. Bottom-up approaches describe the construction of the desired material from smaller entities, which can reach down to the single molecule level. The following section will give an idea of the variety of colloids and colloidal architectures that have been reported in literature, starting with a selection of transmission- and scanning electron microscope (TEM, SEM) images of hard and soft colloidal particles fabricated from various materials (Figure 2).

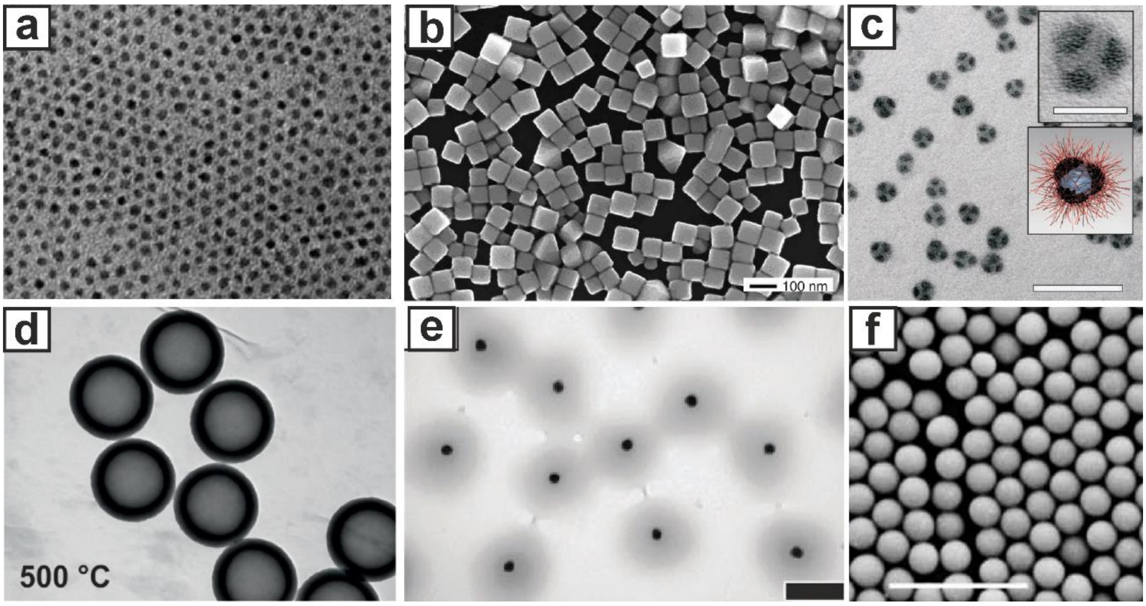

Figure 2: Several soft and hard colloidal particles possessing different functionality. a) TEM image of spherical CdSe nanocrystals.[17] b) Scanning electron micrograph of Ag nanocubes.[18] c) TEM image of multi-compartment polymer particles.[19] d) TEM image of hollow silica nanospheres.[20] e) TEM image Core-shell particles possessing a silver core and a thermos-responsive PNIPAAM shell.[21] f) SEM images of conjugated polymer particles prepared by Suzuki-Miyaura dispersion polymerization.[22]

To point out the different shapes and sizes which are accessible, Figure 2a, b show SEM and TEM micrographs of semiconductor (CdSe) and metal (Ag) nanoparticles. Several other metal compounds can be used for the fabrication of such nanoparticles,[43] and various other shapes are also possible.[44-47] TEM images of multi-compartment polymer colloidal particles are illustrated in Figure 2c. The particles are assembled from ABC triblock terpolymers by selective dialysis. Due to the well-defined polymer patches on the surface of the particles, they can assemble into segmented, supracolloidal polymers on a micrometer length scale with a defined interface design.[19,48] Figure 2d shows TEM images of hollow silica (SiO_2) nanospheres fabricated using polystyrene (PS) spheres as templates.[20] Based on the low thermal conductivity of this materials, they may find application as nano-insulation materials.[49] Figure 2e shows plasmonic silver nanoparticles (black), embedded in a stimuli-responsive shell consisting of poly n-isopropyl acrylamide (poly-NIPAAM). By exceeding the lowest critical solution temperature (LCST) of the poly-NIPAAM shell, the hydrogel shell collapses allowing to manipulate the plasmonic resonance of the silver particle. Conjugated polymer particles are illustrated in Figure 2e. Such materials could act as both, an optical filter due to the photonic bandgap, and as frequency converter based on the photoluminescence.[22]

From this variety of particles, it is possible to fabricate colloidal crystals, possessing additional properties, based on the colloidal structuring. In general, it is possible to assemble colloidal crystal from particles with a polydispersity below 1.05.[43] Therefrom, colloidal structures are obtainable, owning a second level of structural hierarchy.[50] Assuming a sufficiently narrow size distribution, these building blocks arrange into highly crystalline symmetries, similar as found for atoms. Therefore, colloidal assemblies can be used as a model platform, e.g. to study crystal growth processes.[46,51-53] They offer the great advantage of a much larger length compared to their atomic counterpart. This allows a much easier experimental observation. To give an idea of the wide variety of architectures accessible by colloidal assembly, some exemplary colloidal structures are summarized in Figure 3.

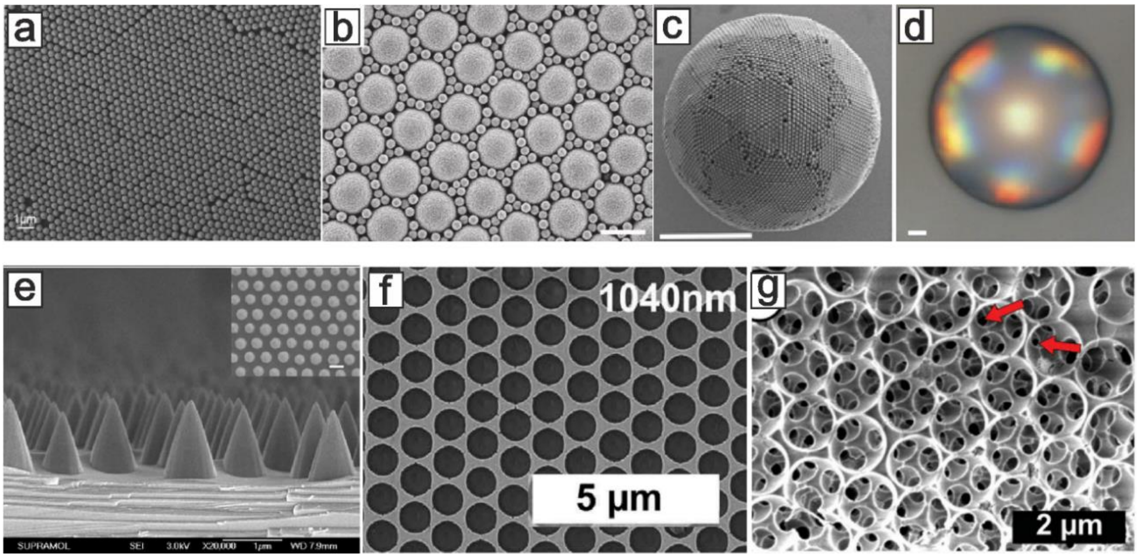

Figure 3: Exemplary structures accessible by colloidal crystallization. (a) A colloidal monolayer of close-packed, monodisperse SiO_2 spheres.[54] (b) Ordered binary PS colloidal monolayer.[55] c,d) SEM and optical micrograph of a microsphere decorated with 400 nm colloidal particles. Grating colors arise from the periodic arrangement of the particles at the surface.[56] e) Silicon cone array obtained via reactive ion etching using a 2D colloidal crystal as mask.[57] f) Gold nanohole array fabricated by colloidal lithography.[58] g) SiO_2 inverse opals from infiltrating a 3D PS colloidal crystal with SiO_2 nanoparticles followed by pyrolysis of the polymer template particles.[59]

Figure 3a and b show SEM images of two examples of 2D colloidal monolayers, which find application as potential anti-reflective coatings[60,61] or as template structures for surface patterning.[62-64] Figure 3c and d exhibit SEM and optical micrographs of a photonic ball assembled from 400 nm colloidal particles. Based on the internal and external particle structure within the photonic ball a variety of optical effects is present.[56,65-67]

The bottom row of Figure 3 indicates structures accessible using colloidal assemblies as sacrificial templates, starting with a periodical array of silicon cones (Figure 3e). The cones are fabricated by reactive ion etching using a monolayer of SiO_2 spheres as a mask.[68] Figure 3f shows gold nanohole arrays prepared by the evaporation of gold on a plasma etched 2D hexagonally close-packed PS colloidal monolayer, which may serve as a transparent electrode material in organic solar cells[58] or as a platform to study particle-substrate interactions.[69] Figure 3d illustrate a SiO_2 inverse opal made from a 3D PS colloidal crystal representing the inverse structure of the former crystals.[70,71] Due to their high surface area these structures are suitable as a framework for catalysts,[72] or to investigate diffusion process through interconnected networks.[73]

Whereas the property of the single particle is still present within the assembly, additional functionality can be achieved by the further structural hierarchy of the assembly.[74-78] Most common is the evolution of photonic band gaps, leading to a complete reflection of light of a specific wavelength.[14,79] In this thesis, monitoring the Bragg reflection during the colloidal film formation process of polymer colloidal crystals is used as a complementary method to thermal transport characterization of the film formation process (see Chapter 4.2). To observe a photonic bandgap, two requirements are necessary i) the particles have to be arranged in a periodic lattice, and ii) the lattice spacing is about the size of a specific wavelength of the incident light. The periodic arrangement of the particles leads to a periodic refractive index contrast and thus, to a periodic variation of the dielectric constant within the materials. This variation is responsible for the manipulation of electromagnetic waves. The incident light is then reflected according to Bragg's law:[80]

$$\mathrm{m}\lambda_{\mathrm{m}} = \lambda_{\mathrm{B}} = 2\mathrm{n}_{\mathrm{e}}\mathrm{d}_{\mathrm{hkl}}\sin\alpha_{\mathrm{B}} \tag{1}$$

where m corresponds to the diffraction order, λ_B is the Bragg diffraction wavelength and n_e the effective refractive index of the assembly. d_{hkl} represents the distance between two lattice planes with Miller indices (h,k,l) and α_B is the angle of incidence of the light beam. Since colloidal crystals behave similar to atoms, this behavior is well-known from X-ray diffraction at atomic lattices. Therefore, indicated by Equation 1, the reflected wavelength depends on the size of the particles defining the lattice spacing and on the angle of the incident light, normal to the crystal planes. The angle dependence is illustrated by a photograph of a SiO_2 colloidal crystal monolayer, displayed in Figure 4a.

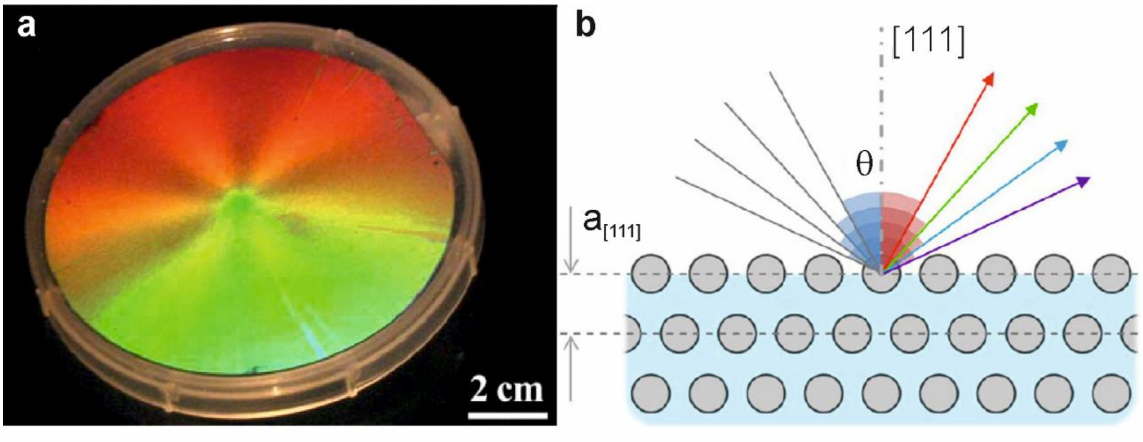

Figure 4: Bragg reflection of colloidal assemblies. a) Photograph of a colloidal crystal monolayer consisting of hexagonal close-packed SiO_2 nanospheres with a diameter of 315 nm.[81] b) Core-shell particles arranged in a colloidal crystal lattice. The shell (blueish) is responsive to the ionic strength. From this, the interplanar spacing can be varied, leading to a shift of the Bragg reflection peak.[32]

The varying angle of the observer relative to the crystal plane shifts the wavelength of the Bragg reflectivity peak, leading to the observed rainbow colors. This behavior offers great potential of colloidal materials acting as optical filters and switches,[82] or as chemical sensors.[83-85] By chemically modifying the particle surfaces, a stimuli-responsive behavior can be further introduced to the assembly,[32,86] e.g. in photonic crystals from core-shell particles possessing a PS core forming the crystal lattice, and a poly (styrene sulfonic acid) shell layer (Figure 4b). In the swollen state, the polyelectrolyte shell is responsive to the ionic allowin to vary the lattice spacing.

As pointed out in this chapter, a great toolbox of particles and assemblies is present in literature, and a large number of articles can be found exploring their unique properties. Still, only little work has been done to investigate thermal transport in colloidal structures, and fundamental studies are necessary. Therefore, this thesis is narrowed to a relatively simple and common system: *polymer colloidal crystals.* The methods used for particle synthesis are described in the following chapter.

2.2 Polymer Particle Synthesis

A countless number of approaches and variations exist in literature to fabricate polymer colloidal particles,[42,87] including emulsion[35,88-90] and dispersion polymerization,[91-93] seed growth techniques[94-96] and mini-emulsion polymerization.[97,98] In this work, emulsifier-free emulsion polymerization has been used exclusively to obtain highly monodisperse polymer particles from styrene, methyl methacrylate (MMA) and n-butyl acrylate (n-BA) as monomer source. This method provides some advantages compared to other techniques. Firstly, the synthesis is carried out in a single batch synthesis, which reduces experimental complexity. Secondly, the synthesis is scalable, allowing to synthesize a sufficient number of particles in only one batch. Therefore, the same particle type can be used throughout the entire experiments, ensuring a necessary sample's consistency. Furthermore, no surfactant is used within this type of emulsion polymerization, since the amphiphilic species is formed during an early stage of the synthesis. This strongly facilitates the purification of the particle after the synthesis because surfactants are generally hard to remove from the final particle dispersion. Additionally, different monomers are accessible wherefrom colloidal particles can be synthesized. Moreover, the size of the particles is adjustable by the experimental parameter,[99,100] e.g. temperature, initiator concentration, the addition of charged co-monomers or the amount of monomer. Besides, using a mixture of MMA and n-BA as the monomer source, it is further possible to accurately adjust the glass transition temperature of the resulting polymer particles.[36] A schematic sketch of the reaction mechanism of an emulsifier-free emulsion polymerization is shown in Figure 5.

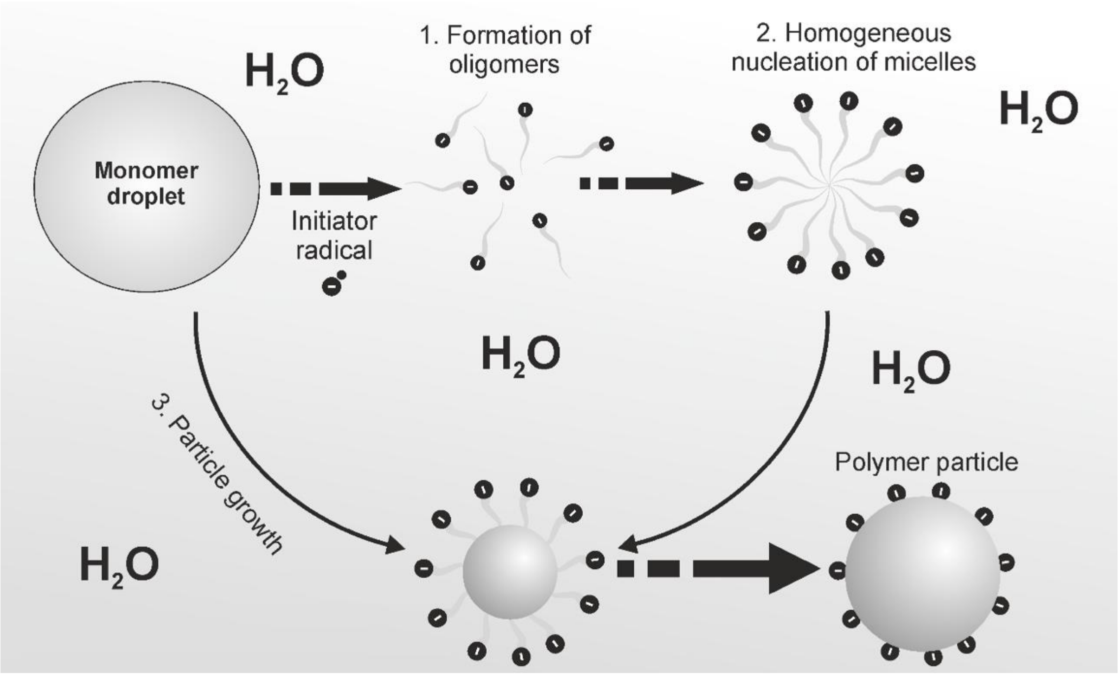

Figure 5: Sketch of the mechanism of an emulsifier-free emulsion polymerization.

The monomer droplets are dispersed in a continuous water phase. Whereas the initiator is water-soluble, the monomer component is poorly soluble in the aqueous phase. Still, some monomer molecules will be dissolved in the water phase and therefore, are able to react with the dissolved initiator. This leads to the formation of oligomers possessing a charged head group, based on the initiator, and a nonpolar tail due to chain growth of the monomer (Figure 5.1). These charged oligomers are now capable to homogeneously nucleate micelles, as known from amphiphiles (Figure 5.2).[101] A constant particle growth is then observed by a continuous diffusion of monomer molecules from the monomer droplets to the micelles (Figure 5.3) until the entire amount of monomer is consumed. In general, the number of nucleated micelles fairly exceeds the number of monomer droplets present in the water phase. Thus, the polymerization is predominantly conducted within the micelles. This results in monodisperse polymer particles possessing a charged surface.

2.3 Colloidal Self-Assembly

Typically, a small amount of charged co-monomer, e.g. styrene sulfonic acid (PSS) or acrylic acid (AA) is added to the reaction mixture. This is necessary to obtain a sufficiently high electrostatic repulsion of the particles, preventing them from agglomeration. In general, aqueous colloidal dispersions are thermodynamically unstable due to their high surface energies. Therefore, these systems tend to reduce their large interface area by the formation of agglomerates. The attractive force between two colloidal particles can be quantified by the Hamaker constant.[102] If two charged colloids approach each other as close as their counterion layers start to interpenetrate, a repulsive potential arises as a function of particle-particle distance.[100] The concept of attraction and repulsion of charged particles has been introduced by Derjaguin, Landau, Verwey and Overbeek in the 1950s.[103,104] The DLVO potential U of two individual particles versus the particle-particle distance d is displayed in Figure 6.

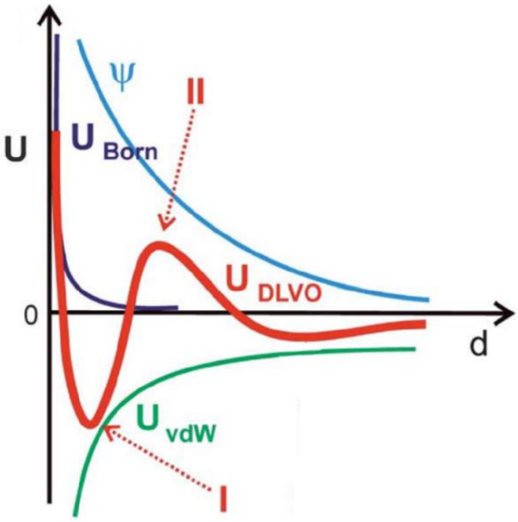

Figure 6: DLVO potential versus the particle-particle distance. (blue) Born repulsion prevents particles from overlapping. (I) Primary minimum based on van der Waals interactions. (II) Electrostatic repulsion causes a primary maximum.[105]

At a sufficiently small distance, a primary minimum is visible (Figure 6.I) based on van der Waals attraction. This minimum is ascribed to irreversible particle agglomeration and must be prevented for stable colloidal dispersions. Agglomeration can be surpressed by a sufficiently strong electrostatic repulsion potential (Figure 6.II). This is why the addition of charged co-monomers is essential to receive stable colloidal dispersions.

Besides electrostatic repulsion, functionalizing the particle surface with a water-soluble polymer layer is another common approach to sterically stabilize aqueous particle dispersions. Here, the interpenetration of the polymer chains of two approaching particles leads to an increasing polymer concentration between the particles. This, in turn, causes an osmotic pressure due to local concentration differences of the polymer layer. The solvent tends to diffusive into the regions of highly concentrated polymers, forcing the particles to separate from each other.[106]

A sufficient particle repulsion is crucial to obtain crystalline colloidal ensembles. Nowadays, a large amount of assembly methods for spherical colloidal particles has been established.[37,38,51,107] Most common for colloidal crystal fabrication are the Langmuir Blodgett technique,[108-110] vertical deposition from aqueous particle dispersions,[111,112] and floating techniques.[113,114] Attractive and repulsive interactions of the particles such as capillary forces, electrostatic interactions and van der Waals forces play a key role during the self-assembly into highly ordered colloidal crystals. Typically, monodisperse hard spheres crystallize in a face-centered cubic (*fcc*) symmetry, since this is the thermodynamically favored crystalline phase, compared to hexagonally closed packings (*hcp)*.[115,116] The various interaction forces, which can occur during the assembly of colloidal particles are schematically illustrated in Figure 7.

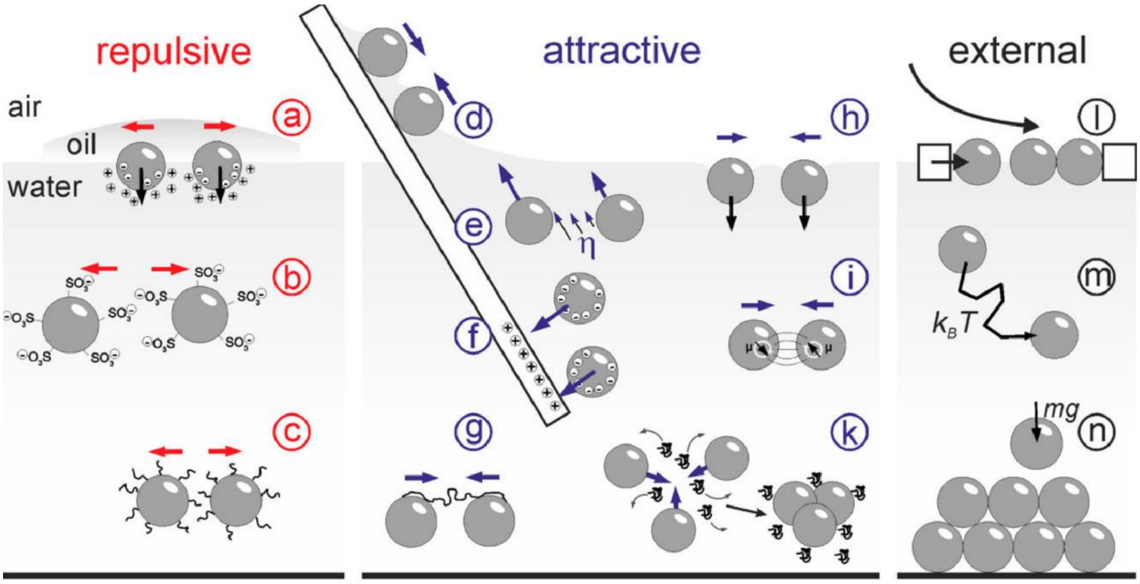

Figure 7: Sketch of interactions and forces during colloidal assembly. (red) Repulsive interactions. (blue) Attractive interactions and (black) external forces applied to the particles. a) Dipolar, b) Coulomb (electrostatic) and c) steric repulsion. d,h) Capillary forces, e) drag forces, f) Coulomb attraction, g) agglomeration, i) v.d.W attraction, k) depletion attraction. i) Barrier compression, m) Brownian motion, n) gravitational sedimentation.[37]

Repulsive interactions are summarized in Figure 7, red, showing electrostatic (Figure 7a,b) and steric interactions (Figure 7c), as discussed above. A stronger particle-particle repulsion based on dipolar repulsion at an oil-water interface is additionally displayed. In this case, the stronger particle repulsion is due to an only partial ion dissociation in the water phase. Attractive forces are pointed out in Figure 7, blue. From the various attractive interactions, capillary attraction (Figure 7d) plays the most important role in the vertical deposition and floating assembly techniques, as well as for simple evaporation-induced self-assembly. Here, during the evaporation of the aqueous phase, the dispersed particles approach each other due to capillary attractions. Based on the electrostatic repulsion between the particles, the particles will be oriented into their energetically minimum position. This results in a crystalline structure, representing the most energetically preferable particle arrangement. Figure 7, black indicates different external forces, which can be used to conduct colloidal assembly e.g. compression (Figure 7l), as it is applied by the Langmuir Blodgett technique, or gravitational force leading to the sedimentation of the particles (Figure 7n), e.g. for assembly by filtration or centrifugation

In this thesis, colloidal crystals and assemblies were fabricated by either evaporation-induced self-assembly, vertical deposition (dip-coating) or filtration. Evaporation-induced self-assembly yields highly crystalline colloidal monoliths of a uniform thickness of several hundred micrometers, preferably for thermal transport characterization. From vertical deposition, highly crystalline assemblies are obtainable, possessing thicknesses of tens of micrometers. Based on the preparation on a substrate of choice, this technique is preferable for determining the optical properties of the investigated assemblies. Assembly by filtration allows fabricating multi-layer colloidal assemblies with precise control over the thicknesses of the individual layers. Therefore, the properties of different particles can be combined in only one colloidal ensemble. Noteworthy, assemblies received from filtration do not possess an as high crystallinity, due to the fast assembly process.

2.4 Thermal Transport in Bulk Materials

The manipulation of electrons and photons is commonly known in semiconducting materials, or in optical fibers or photonic crystals, respectively. Besides, another quasi-particle exists, which is responsible for the transmission of sound and heat in dielectric materials: *The Phonon*. As known from the concept of wave-particle duality for photons and electrons, phonons can also be described as particles or as waves. Phonons can be understood as cooperative, mechanical vibrations, transmitted through the atomic lattice. Whether a phonon is resposible for the transmission of sound or heat depends on its oscillation frequency. The phononic spectrum is shown Figure 8.

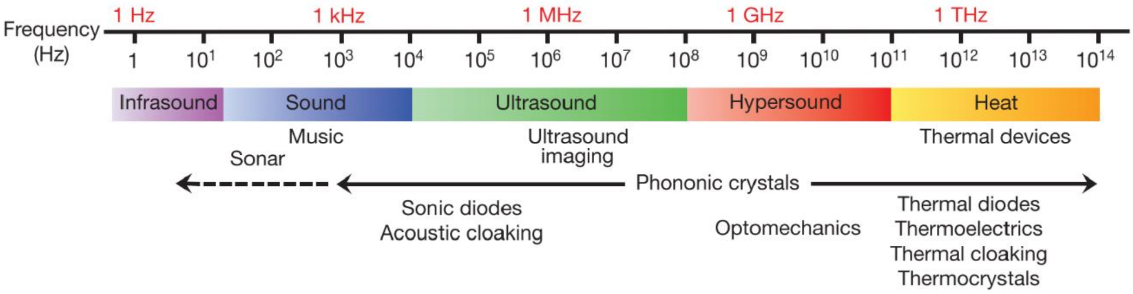

Figure 8: The phononic spectrum.[13]

Whereas sound waves oscillate at low frequencies (kilohertz) and can propagate over long distances, as known for sonar systems, high-frequency phonons (terahertz) are responsible for the transport of heat and can only propagate over short distances. Since phonons can be treated as quasi-particles, the thermal conductivity κ of a dielectric solid is describable by the Debye equation according to the kinetic theory:

$$\kappa = \frac{1}{3} C_v v_g \Lambda \tag{2}$$

Here, C_v is the volumetric heat capacity, describing how much thermal energy can be stored in the material. v_g represents the sound group velocity of the phonons, excited at a specific temperature T, and Λ is the average phonon mean free path (MFP), giving the characteristic length that a phonon can travel freely between two scattering events. The thermal conductivity is a quantity how much energy is conducted through a material per unit time. To give an impression of the thermal conductivity, the values of some highly conducting, and insulating materials are summarized in Table 1.

Table 1: Thermal conductivity of several selected materials.

	Thermal conductivity at 25 °C [$Wm^{-1}K^{-1}$]
Diamond (crystalline)	>3000[117,118]
Diamond (amorphous)	~4[119]
Copper	~400[120]
Silica	~1.4[120]
Polymers	~0.1 - 0.5[121,122]

As easily seen by the comparison of the thermal conductivity of crystalline and amorphous diamond, the thermal conductivity strongly depends on the atomic structure of a material. Whereas crystalline materials generally possess high thermal conductivities, this is reversed for disordered/amorphous solids.[123] That behavior is based on the long phonon MFPs present in crystalline materials, in contrary to very short MFPs present in disordered materials. The length of the phonon MFP is influenced by various scattering events which may occur during the propagation process. Important phononic scattering processes are summarized in Figure 9a.

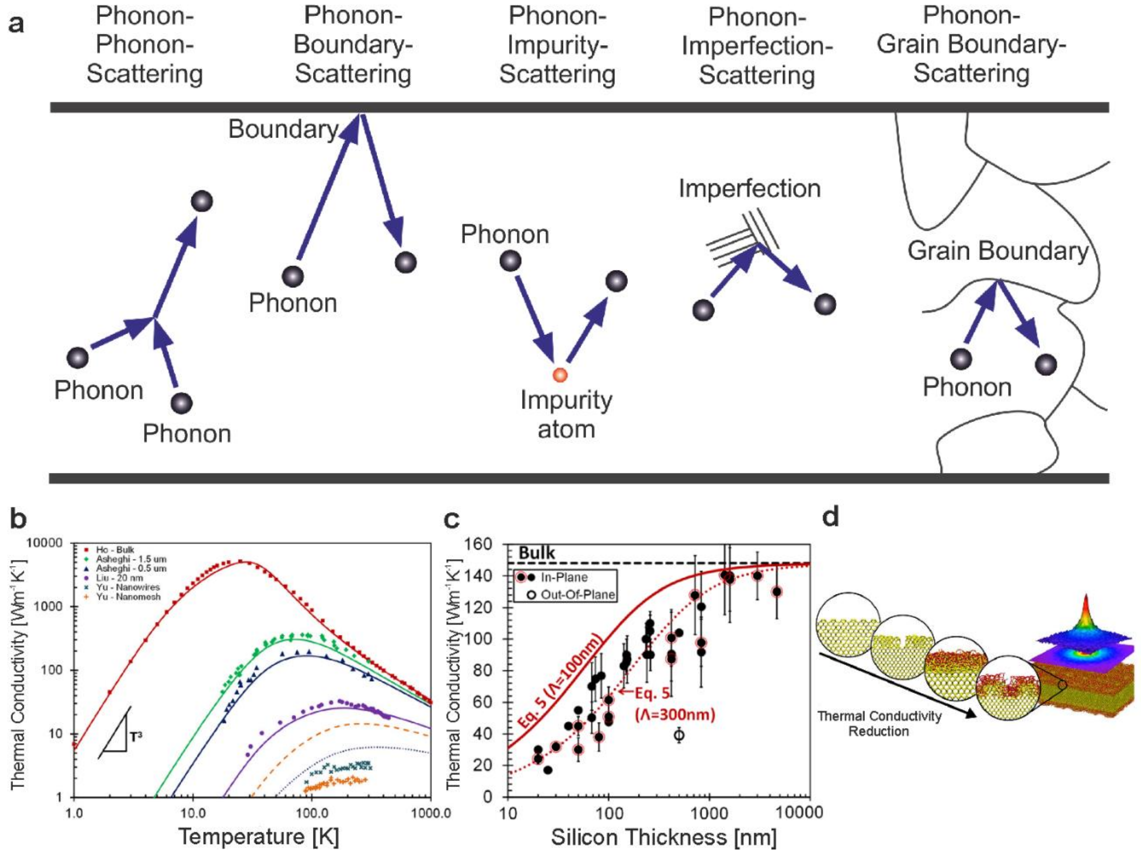

Figure 9: Scattering events in dielectric materials. a) Schematic sketch of several scattering mechanisms i) Phonon-phonon scattering occurs from the anharmonicity of the atomic lattice. ii) Scattering at the boundaries is observed in materials which thickness is in the range of the MFP. iii) Scattering of phonons at impurities or iv) imperfections. v) Scattering at grain boundaries e.g. differently oriented crystallites.[124] b) Temperature-dependent thermal conductivity of crystalline silicon materials.[125] c) Thickness-dependency of the thermal transport in silicon membranes.[125] d) Influence of surface roughness on the thermal conductivity.[126]

Phonon-phonon scattering occurs due to the anharmonic oscillation character of the lattice potential.[127] Noteworthy, phonon-phonon scattering is the main reason why the thermal conductivity of an ideally crystalline material is finite with temperature and does not steadily increase due to the increase of the heat capacity. Below the Debye temperature, only few phonon modes exist, enabling long mean free paths. Above the Debye temperature, the full phonon population is excited, leading to an increasing phonon-phonon scattering and thus, to a finite thermal conductivity. Therefore, the thermal conductivity of crystalline material increases with a ~T^3 dependence of the heat capacity below the Debye temperature and decreases with ~T^{-1} at higher temperatures (Figure 9b).[125]

Furthermore, boundary scattering can occur, which is of interest in thin film materials, where the thickness of the samples is in the range of the phonon MFP (Figure 9c). Besides, scattering at the surface roughness (Figure 9d), impurities, imperfections and grain boundaries will certainly reduce the thermal transport through a material.[124,128-130]

In particular, for materials possessing a high interface density, e.g. colloidal structures, the transport of heat across these interfaces plays a crucial role for their thermal transport properties, since these systems are dominated by their interfaces. Quite obvious, the size of interface area is decisive for the thermal transport across the interface.[131,132] With increasing interface area, the thermal conductivity is increased and vice versa.[133]

Additionally, the bonding strength between the interfaces strongly influences the thermal transport across an interface, described by thermal interface conductance. Heat transmission by phonons across an interface can be rationalized by two models: i) the acoustic mismatch model (AMM),[134] considering differences in the speed of sound on each side of the interface. Here, phonons are expected to cross the interface elastically without being scattered. ii) the diffusive mismatch model (DMM),[135] where differences in the density of states are assumed. In this model, a complete and random scattering of phonons occurs by crossing the interface. The influence of the bonding strength on the thermal interface conductance has been experimentally studied by Losego et al.[24] on self-assembled monolayers (SAMs), sandwiched between a quartz substrate and a transfer-printed gold film. The SAM head group binding to the transfer-printed gold layer is varied, allowing to control the bonding strength at the SAM-gold interface. The experimental system is schematically sketched in Figure 10a, as well as the different head groups.

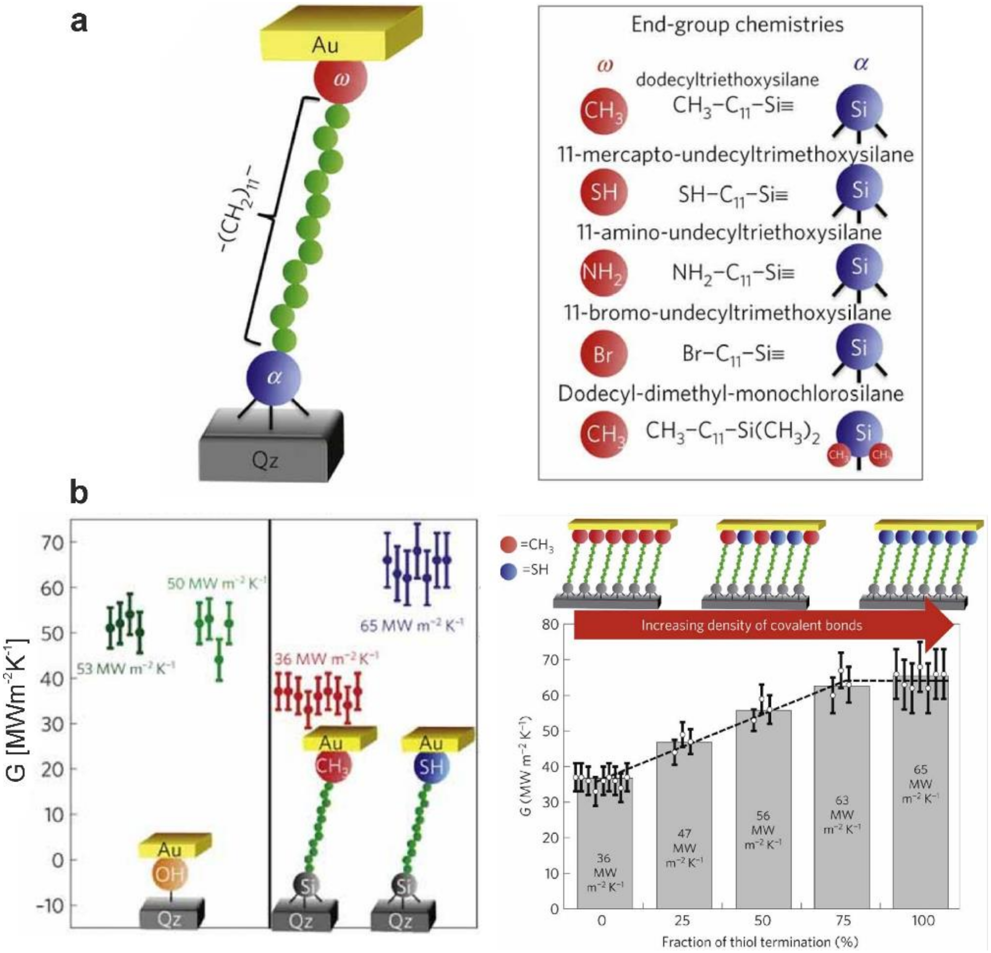

Figure 10: Influence of bonding strength on the interface conductance. a) Sketch of the experimental system and possible end groups (red). b, left) Interface thermal conductance of SAMs, differently bonded to a gold layer. b, right) Influence of increasing SH-group content on the thermal conductance of a SAM, allowing to tailor the thermal interface conductance.[24]

Based on the chosen head group, the interface thermal conductance increases from methyl to hydroxyl groups, and possesses the highest value for thiol terminated SAMs (Figure 10b, left). This correlates well with the increasing bonding strength. Furthermore, the mixture of methyl and thiol terminated SAMs allows to directly tune the interface thermal conductance, depending on the mixing ratio (Figure 10b, left).

The depicted concept of phonons, outlined in the previous section, is valid to describe heat conduction in crystalline solids, but it becomes less applicable to describe heat conduction in disordered materials e.g. silica or amorphous polymers. This is based on the lack of translational symmetry of the atomic lattice within these materials. In an ideal crystalline material heat conduction can be described as ballistic transport of phonons, in which their mean free path largely exceeds the unit cell size and phonons transverse the systems with minimum scattering. In contrary, diffusive transport is present in amorphous matter. Here, the mean free path is reduced to less than the interatomic distances, due to a strong scattering at the disordered atomic structure. For this reason, it is challenging to predict the thermal transport behavior of amorphous materials. Einstein theoretically described heat conduction in amorphous solids as a random walk of independent oscillators, termed as diffusion modes (diffusons).[136] The picture of a random walk of interacting, but independent oscillators already point out the complexity to accurately describe heat conduction in these materials. Allen and Feldman[137,138] extended the theoretical descriptions of Einstein by introducing two further vibrational modes termed as locons and propagons. Propagons represent propagating, wave-like vibrational modes with MFPs longer than the interatomic spacing. Whereas propagons and diffusion can contribute to heat transport due to their delocalized, propagating character, locons represent localized, non-propagation vibrational modes which therefore do not contribute to heat transport but to the specific heat capacity.[139]

2.5 Thermal Transport in Polymers

Since this thesis deals with the thermal transport of polymer based colloidal materials, heat transport in polymers is briefly discussed in the following. In general, polymers are known to be thermal insulators due to several occurring scattering events, resulting in diffusive heat transport. Thermal transport in polymers is slightly different than known for other material classes. This is based on their chain-like structure, as well as their ability to form crystalline and amorphous regions, in which the chains are either extended and highly oriented, or possess a random-coiled structure. The transmission of vibrational energy in an extended and a randomly coiled polymer chain is schematically compared in Figure 11.

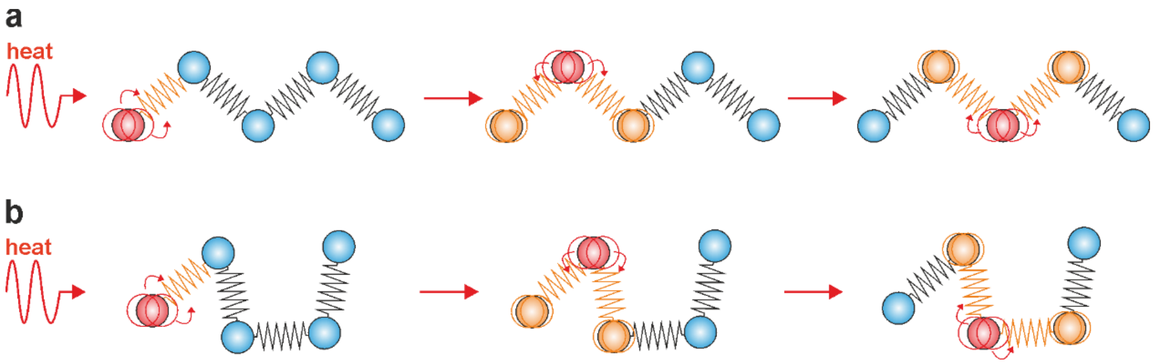

Figure 11: Transmission of thermal vibrations along a polymer chain. a) Phonon propagation along an extended polymer chains. b) Propagation along a random-coiled chain.

Thinking about an extended polymer chain, e.g. in the crystallite regions of a semi-crystalline polymer, the transmission of thermal vibrations along the oriented chain axis is favorable, due to a reduced curvature of the chain (Figure 11a). Therefore, less structural scattering occurs at the chain backbone structure, leading to an efficient transport of vibrational energy along the chain. In contrary, structural scattering of vibrational modes is strongly increased within a random-coiled chain, based on its strong curvature (Figure 11b). Therefore, the alignment of the polymer chain can strongly affect the polymer's thermal conductivity. Noteworthy, thermal transport perpendicular to the chain alignment is less efficient, leading to a strong anisotropic thermal conductivity of crystalline polymer regions. [140,141] This is based on a less efficient transmission of heat from chain to chain due to weak bonding forces present between the chains.

Since chain ends, mass and boundary variations within the backbone, as well as the interfaces between amorphous and crystalline regions can act as additional scattering events,[142,143] it is apparent why bulk polymers are commonly known as thermal insulators. Still, several examples can be found in literature, describing exceptionally high thermal conductivity along the chain axis for highly oriented, crystalline polymer fibers.[144-149] This is achieved by stretching the polymer fibers to increase the crystallinity of the fibers towards the crystallinity of a polymer single crystal. Therefore, phonon scattering is strongly suppressed, leading to thermal conductivity of nearly ~100 $Wm^{-1}K^{1}$.[144]

2.6 Thermal Transport in Porous Materials

In this thesis, thermal transport is investigated in nanoporous colloidal structures, fabricated from amorphous polymer particles. Here the structural size strongly exceeds the phonon MFP of high frequent phonons. Thus, diffusive thermal transport is present within the investigated structures. The effective thermal conductivity κ_{eff} of such open-porous particle networks can be expressed by the following contributions:

$$\kappa_{eff} = \kappa_{solid} + \kappa_{gas} + \kappa_{conv} + \kappa_{rad} \tag{3}$$

Where κ_{solid} represents the contribution of heat transport by conduction through the solid phase and depends on the bulk thermal conductivity. κ_{conv} describes heat transport by mass transport and convection, and κ_{rad} is the ratio of thermal energy transmitted by infrared (IR) radiation. Convective gas transport in colloidal structures is negligible since it primarily emerges at pore diameters larger than 4 mm.[150] Radiative transport increases with temperature and is influenced by the density and emissivity of the investigated porous material.[151] κ_{gas} expresses the contribution of heat transport by conduction through the gas phase and depends on the pore sizes present within the structure. By reducing the pore size to sizes in the range of the mean free path of the gas phase, gas-gas molecule collisions are replaced by a higher probability of the gas-interface collisions within the constraining geometry. The probability of a molecule-molecule or molecule-interface collision in a porous material is described by the Knudsen-number K_{N}.[152]

$$K_N = \frac{l_G}{L_{ch}} \qquad (4)$$

The Knudsen-number quantifies the ratio of the mean free path of the gas molecules l_G and the pore size L_{ch}. In the case of $K_N \ll 1$, the molecule-molecule collisions predominate and the thermal conductivity κ_G of the cell gas can be calculated according to the kinetic theory of free gases.[153] In contrary, when $K_N \gg 1$, the pore size is much smaller than the mean free path of the gas molecules. This is the case for low pressures (long MFP of gas phase) or in very small cavities. Therefore, molecule-interface collisions predominate. Here, the thermal energy of the molecule is not completely transferred to the interface based on a partial elastic reflection of the molecule. This results in a reduction of the thermal conductivity with decreasing sizes of the cavities.[152]

2.7 Thermal Transport in Colloidal Materials

The thermal transport within a colloidal material is mainly affected by the following four key parameters, which are related to the previous chapters:

- The chosen bulk material
- The colloidal architecture
- The interface density
- The interface thermal conductance

The colloidal structure can be either fabricated from highly conducting materials, e.g. metals, or it consists of low conducting materials, e.g. silica or polymers (see Chapter 2.1). This obviously will affect the thermal transport properties of the resulting colloidal material and can be decisive if thermal transport within a colloidal material is either ballistic[25,34] and influenced by the structuring on the colloidal length scale, or diffusive.

Furthermore, the thermal transport is affected by the structuring itself. The material can be fully dense, as it is for polymer nanocomposites or organoclays,[28,29,154] or it possesses a more or less well-defined porous structure, known from the assembly of spherical particles, or inverse opals and aerogels.[155-158] Here, the introduction of porosity will affect the density of the material and, therefore, its thermal conductivity (see Chapter 2.6). In general, colloidal materials further possess a high interface density, leading to a large number of phonon scattering sites. The higher the interface density, the more scattering sites are present in the material. This is favorable for the development of highly insulating thin films. Due to their high interface density, colloidal materials are additionally strongly influenced by the thermal interface conductance, as briefly discussed in Chapter 2.4.

In the following, the potential of colloidal structuring in the field of heat transport is emphasized, related to the four key parameters mentioned above. Colloidal structuring is only rarely used to study phonon heat transport fundamentally. Noteworthy, polymer colloidal crystals from particles with a diameter of ~250 nm have been used as phononic crystals. These crystals possess a phononic bandgap, at which the propagation of acoustic waves of a certain frequency is forbidden.[159] Still, the introduced band gaps only cover low phonon frequencies, which mainly do not contribute to heat transport.

To mention one example for a fundamental study of heat transport using colloidal structures, Barako et al.[34] took advantage of highly ordered colloidal nanostructures investigating thermal transport in metal inverse opals. Here, the MFP of heat carries is long enough to interfere with the metallic colloidal structure. Figure 12a shows the investigated metal opals and the results of their thermal transport characterization.

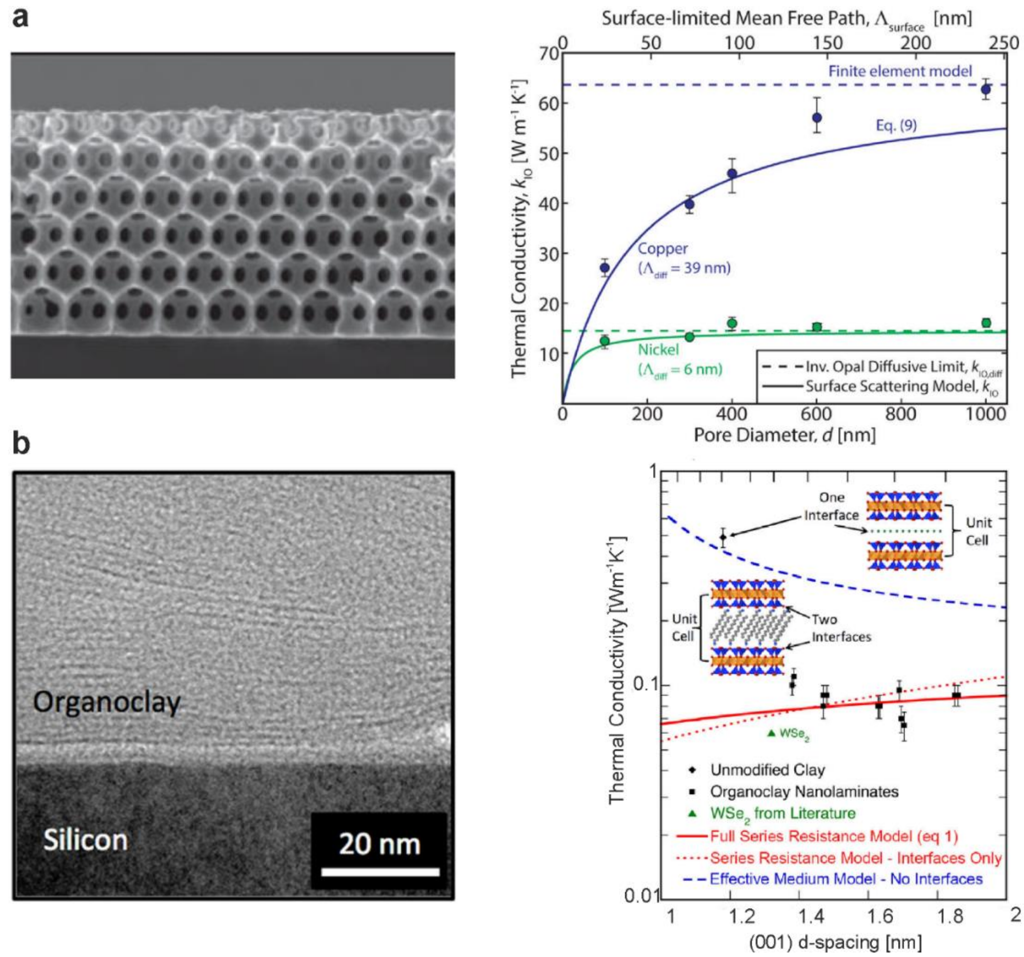

Figure 12: Thermal transport in metal inverse opals and influence of a high interface density. a) SEM side-view of a nickel inverse opal with a pore size of about 600 nm and thermal conductivity of a copper and nickel inverse opal in dependence of the pore size.[34] b) SEM image of an organoclay nanolaminate supported on a silicon substrate and thermal conductivity of these laminates in dependence of the d-spacing.[23]

They demonstrate quasi-ballistic thermal transport present within the investigated metal inverse opals. Noteworthy in this work, thermal transport is governed by electrons, since the fabricated inverse opals consist of electrically conducting materials. They were able to observe the transition between diffusive to ballistic transport behavior by adjusting the pore sizes of the opal structures during the colloidal fabrication. Metal inverse opals were also used to study coherent grain boundary scattering of phonons.[25]

To point out the influence of a high interface density, Figure 12b, left exhibit a SEM cross-section of organoclay nanolaminates on a silicon substrate. Due to the low thickness of only a few nanometers of these anisotropic colloids, a high interface density of 1-1.5 interfaces/nm is reached. Therefore, an ultra low thermal conductivity of < 0.1 Wm^{-1}K^{-1} is obtained, still in a fully dense thin film.[23,30]

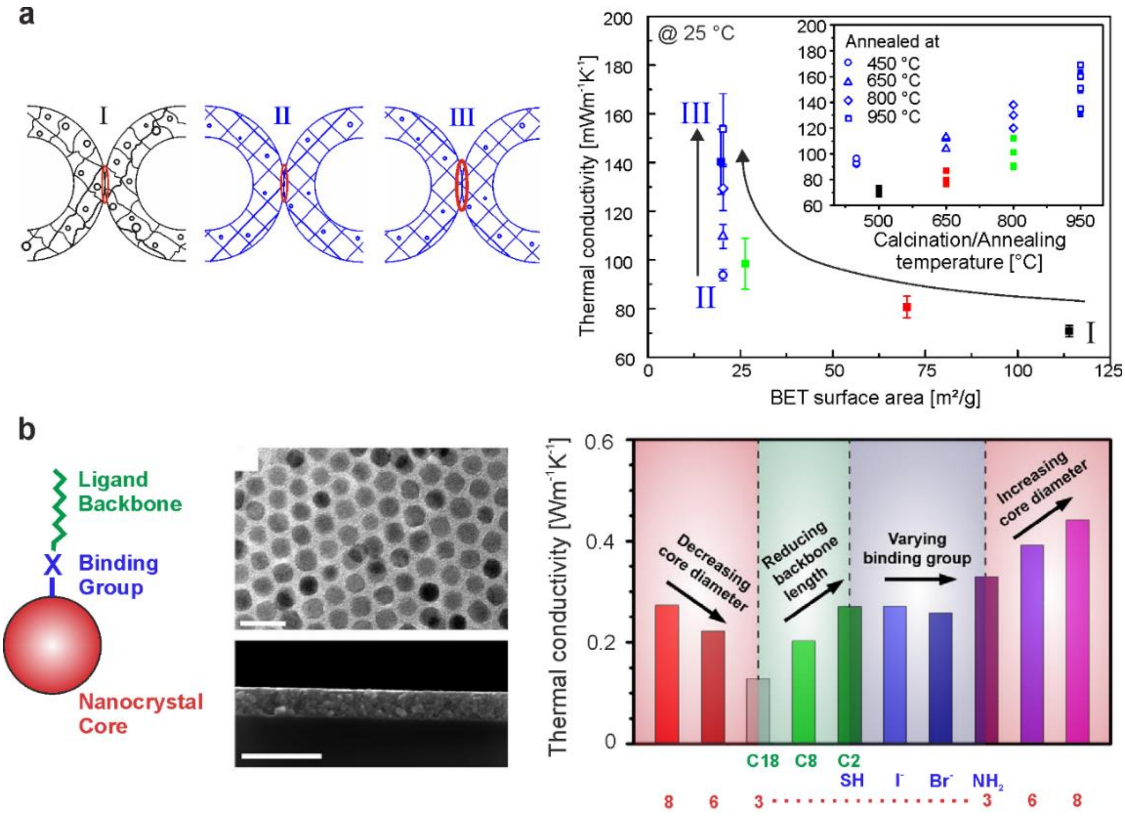

Figure 13: Influence of interfacial bonding and surface chemistry. a) Thermal transport in silica hollow sphere colloidal crystals. Based on the calcination temperature, the interfacial bonding between the particle and the internal shell structure can be varied.[20] b) Influence of surface chemistry on the thermal conductivity of PbS nanocrystal composites.[160]

As mentioned, the contact strength between two interfaces can be decisive for thermal transport through interface dominated materials. Ruckdeschel et al.[20] studied the influence of the interfacial contact strength on the thermal conductivity of a hollow silica nanosphere colloidal crystals (Figure 13a). The calcination of a colloidal crystal leads to an enhancement of the interfacial bonding between neighboring hollow silica spheres, which in turn results in a drastic increase in the thermal conductivity. This points out the strong influence of the interfacial bonding strength on heat transport through particulate colloidal structures.

Furthermore, the influence of the surface chemistry has been systematically studied for colloidal nanocrystal arrays possessing a semiconducting particle core.[28,29,160] The system used by Liu et al.[160] is schematically sketched in Figure 13b, left. The investigated nanocrystals were sterically stabilized by a thin organic layer, and self-assembled into ordered nanocrystal arrays (Figure 13b, middle). Based on the versatility of this platform, they investigated several parameters such as core diameter, ligand length, and binding group. They found the influence of the binding group to be negligible and that the ligand predominantly dictated the thermal transport properties.

As outlined in this introductory section, a wide variety of colloidal materials and structures are present in literature. Depending on the chosen materials, these structures possess various unique properties, and may be utilized to study different aspects of thermal transport in colloidal architectures. In the following main part, the existing work is extended by detailed studies on the thermal conductivity of polymer colloidal crystals and assemblies.

2.8 References

1. Liu, M., Ma, Y., Wu, H. & Wang, R. Y. Metal matrix–metal nanoparticle composites with tunable melting temperature and high thermal conductivity for phase-change thermal storage. *ACS Nano*, **9**, 1341-1351, (2015).
2. Chau, M. *et al.* Reversible transition between isotropic and anisotropic thermal transport in elastic polyurethane foams. *Materials Horizons*, **4**, 236-241, (2017).
3. Li, Y. *et al.* Temperature-dependent transformation thermotics: From switchable thermal cloaks to macroscopic thermal diodes. *Phys. Rev. Lett.*, **115**, 195503, (2015).
4. Chen, Z. *et al.* A photon thermal diode. *Nat. Commun.*, **5**, 5446, (2014).
5. Wu, G. & Li, B. Thermal rectification in carbon nanotube intramolecular junctions: Molecular dynamics calculations. *Phys. Rev. B*, **76**, 085424, (2007).
6. Zhu, J. *et al.* Temperature-gated thermal rectifier for active heat flow control. *Nano Lett.*, **14**, 4867-4872, (2014).
7. Chang, C. W., Okawa, D., Majumdar, A. & Zettl, A. Solid-state thermal rectifier. *Science*, **314**, 1121-1124, (2006).
8. Kubytskyi, V., Biehs, S.-A. & Ben-Abdallah, P. Radiative bistability and thermal memory. *Phys. Rev. Lett.*, **113**, 074301, (2014).

9. Wang, L. & Li, B. Thermal memory: A storage of phononic information. *Phys. Rev. Lett.*, **101**, 267203, (2008).
10. Wuttig, M. & Yamada, N. Phase-change materials for rewriteable data storage. *Nat. Mater.*, **6**, 824-832, (2007).
11. Cahill, D. G. *et al.* Nanoscale thermal transport. *J. Appl. Phys.*, **93**, 793-818, (2003).
12. Cahill, D. G. *et al.* Nanoscale thermal transport. Ii. 2003-2012. *Appl. Phys. Rev.*, **1**, 45, (2014).
13. Maldovan, M. Sound and heat revolutions in phononics. *Nature*, **503**, 209-217, (2013).
14. Joannopoulos, J. D., Villeneuve, P. R. & Fan, S. Photonic crystals: Putting a new twist on light. *Nature*, **386**, 143-149, (1997).
15. Alonso-Redondo, E. *et al.* Phoxonic hybrid superlattice. *ACS Applied Materials & Interfaces*, **7**, 12488-12495, (2015).
16. Lanzillotti-Kimura, N. D., Fainstein, A., Lemaître, A. & Jusserand, B. Nanowave devices for terahertz acoustic phonons. *Appl. Phys. Lett.*, **88**, 083113, (2006).
17. Zeng, J., Wang, X. & Hou, J. G. in *Nanocrystal* (ed Yoshitake Masuda) Ch. 03 (InTech, 2011).
18. Skrabalak, S. E., Au, L., Li, X. & Xia, Y. Facile synthesis of ag nanocubes and au nanocages. *Nat. Protocols*, **2**, 2182-2190, (2007).
19. Gröschel, A. H. *et al.* Precise hierarchical self-assembly of multicompartment micelles. *Nat. Commun.*, **3**, 710, (2012).
20. Ruckdeschel, P., Kemnitzer, T. W., Nutz, F. A., Senker, J. & Retsch, M. Hollow silica sphere colloidal crystals: Insights into calcination dependent thermal transport. *Nanoscale*, **7**, 10059-10070, (2015).
21. Honold, T., Volk, K., Rauh, A., Fitzgerald, J. P. S. & Karg, M. Tunable plasmonic surfaces via colloid assembly. *Journal of Materials Chemistry C*, **3**, 11449-11457, (2015).
22. Kuehne, A. J. C., Gather, M. C. & Sprakel, J. Monodisperse conjugated polymer particles by suzuki–miyaura dispersion polymerization. *Nat Commun*, **3**, 1088, (2012).
23. Losego, M. D., Blitz, I. P., Vaia, R. A., Cahill, D. G. & Braun, P. V. Ultralow thermal conductivity in organoclay nanolaminates synthesized via simple self-assembly. *Nano Lett.*, **13**, 2215-2219, (2013).
24. Losego, M. D., Grady, M. E., Sottos, N. R., Cahill, D. G. & Braun, P. V. Effects of chemical bonding on heat transport across interfaces. *Nat. Mater.*, **11**, 502-506, (2012).
25. Ma, J. *et al.* Coherent phonon-grain boundary scattering in silicon inverse opals. *Nano Lett.*, **13**, 618-624, (2013).
26. Parchine, M., McGrath, J., Bardosova, M. & Pemble, M. E. Large area 2d and 3d colloidal photonic crystals fabricated by a roll-to-roll langmuir–blodgett method. *Langmuir*, **32**, 5862-5869, (2016).
27. Abad, B., Borca-Tasciuc, D. A. & Martin-Gonzalez, M. S. Non-contact methods for thermal properties measurement. *Renew. Sust. Energ. Rev.*, **76**, 1348-1370, (2017).
28. Ong, W.-L., Majumdar, S., Malen, J. A. & McGaughey, A. J. H. Coupling of organic and inorganic vibrational states and their thermal transport in nanocrystal arrays. *J Phys. Chem. C*, **118**, 7288-7295, (2014).

29. Ong, W.-L., Rupich, S. M., Talapin, D. V., McGaughey, A. J. H. & Malen, J. A. Surface chemistry mediates thermal transport in three-dimensional nanocrystal arrays. *Nat. Mater.*, **12**, 410-415, (2013).
30. Chiritescu, C. *et al.* Ultralow thermal conductivity in disordered, layered wse2 crystals. *Science*, **315**, 351-353, (2007).
31. Costescu, R. M., Cahill, D. G., Fabreguette, F. H., Sechrist, Z. A. & George, S. M. Ultra-low thermal conductivity in w/al2o3 nanolaminates. *Science*, **303**, 989-990, (2004).
32. Nucara, L. *et al.* Ionic strength responsive sulfonated polystyrene opals. *ACS Applied Materials & Interfaces*, **9**, 4818-4827, (2017).
33. Yuan, C., Huang, M., Cheng, Y. & Luo, X. Bonding-induced thermal transport enhancement across a hard/soft material interface using molecular monolayers. *Phys. Chem. Chem. Phys.*, **19**, 7352-7358, (2017).
34. Barako, M. T. *et al.* Quasi-ballistic electronic thermal conduction in metal inverse opals. *Nano Lett.*, **16**, 2754-2761, (2016).
35. Goodwin, J. W., Hearn, J., Ho, C. C. & Ottewill, R. H. Studies on the preparation and characterisation of monodisperse polystyrene latices. *Colloid. Polym. Sci.*, **252**, 464-471, (1974).
36. Still, T. *et al.* Vibrational eigenfrequencies and mechanical properties of mesoscopic copolymer latex particles. *Macromolecules*, **43**, 3422-3428, (2010).
37. Vogel, N., Retsch, M., Fustin, C.-A., del Campo, A. & Jonas, U. Advances in colloidal assembly: The design of structure and hierarchy in two and three dimensions. *Chem. Rev.*, **115**, 6265-6311, (2015).
38. Phillips, K. R. *et al.* A colloidoscope of colloid-based porous materials and their uses. *Chem. Soc. Rev.*, **45**, 281-322, (2016).
39. Li, B., Wang, L. & Casati, G. Thermal diode: Rectification of heat flux. *Phys. Rev. Lett.*, **93**, 184301, (2004).
40. Gregory, J. Basic principles of colloid science - everett,dh. *Nature*, **338**, 182-182, (1989).
41. Keddie, J. L. Film formation of latex. *Mat. Sci. Eng. R.*, **21**, 101-170, (1997).
42. Xia, Y. N., Gates, B., Yin, Y. D. & Lu, Y. Monodispersed colloidal spheres: Old materials with new applications. *Adv. Mater.*, **12**, 693-713, (2000).
43. and, C. B. M., Kagan, C. R. & Bawendi, M. G. Synthesis and characterization of monodisperse nanocrystals and close-packed nanocrystal assemblies. *Annu. Rev. Mater. Sci.*, **30**, 545-610, (2000).
44. Manna, L., Scher, E. C. & Alivisatos, A. P. Synthesis of soluble and processable rod-, arrow-, teardrop-, and tetrapod-shaped cdse nanocrystals. *J. Am. Chem. Soc.*, **122**, 12700-12706, (2000).
45. Ehlert, S. *et al.* Polymer ligand exchange to control stabilization and compatibilization of nanocrystals. *ACS Nano*, **8**, 6114-6122, (2014).
46. Redl, F. X., Cho, K. S., Murray, C. B. & O'Brien, S. Three-dimensional binary superlattices of magnetic nanocrystals and semiconductor quantum dots. *Nature*, **423**, 968-971, (2003).
47. Mehdizadeh Taheri, S. *et al.* Self-assembly of smallest magnetic particles. *Proceedings of the National Academy of Sciences*, **112**, 14484-14489, (2015).
48. Groschel, A. H. *et al.* Guided hierarchical co-assembly of soft patchy nanoparticles. *Nature*, **503**, 247-251, (2013).

49. Gao, T., Jelle, B. P., Sandberg, L. I. & Gustavsen, A. Monodisperse hollow silica nanospheres for nano insulation materials: Synthesis, characterization, and life cycle assessment. *ACS Appl. Mater. Inter.*, **5**, 761-767, (2013).
50. Cheng, Z., Russel, W. B. & Chaikin, P. M. Controlled growth of hard-sphere colloidal crystals. *Nature*, **401**, 893-895, (1999).
51. Li, F., Josephson, D. P. & Stein, A. Colloidal assembly: The road from particles to colloidal molecules and crystals. *Angew. Chem. Int. Ed.*, **50**, 360-388, (2011).
52. Bartlett, P., Ottewill, R. H. & Pusey, P. N. Superlattice formation in binary mixtures of hard-sphere colloids. *Phys. Rev. Lett.*, **68**, 3801-3804, (1992).
53. Chen, M., Cölfen, H. & Polarz, S. Centrifugal field-induced colloidal assembly: From chaos to order. *ACS Nano*, **9**, 6944-6950, (2015).
54. Wu, Y. *et al.* Fabrication of wafer-size monolayer close-packed colloidal crystals via slope self-assembly and thermal treatment. *Langmuir*, **29**, 14017-14023, (2013).
55. Vogel, N., de Viguerie, L., Jonas, U., Weiss, C. K. & Landfester, K. Wafer-scale fabrication of ordered binary colloidal monolayers with adjustable stoichiometries. *Adv. Funct. Mater.*, **21**, 3064-3073, (2011).
56. Vogel, N. *et al.* Color from hierarchy: Diverse optical properties of micron-sized spherical colloidal assemblies. *Proceedings of the National Academy of Sciences*, **112**, 10845-10850, (2015).
57. Zhang, X. *et al.* Morphology and wettability control of silicon cone arrays using colloidal lithography. *Langmuir*, **25**, 7375-7382, (2009).
58. Stelling, C. *et al.* Plasmonic nanomeshes: Their ambivalent role as transparent electrodes in organic solar cells. *Sci. Rep.*, **7**, 42530, (2017).
59. Retsch, M. & Jonas, U. Hierarchically structured, double-periodic inverse composite opals. *Adv. Funct. Mater.*, **23**, 5381-5389, (2013).
60. Stelling, C., Bernhardt, C. & Retsch, M. Subwavelength etched colloidal monolayers: A model system for tunable antireflective coatings. *Macromol. Chem. Phys.*, **216**, 1682-1688, (2015).
61. Zhao, Y., Wang, J. & Mao, G. Colloidal subwavelength nanostructures for antireflection optical coatings. *Opt. Lett.*, **30**, 1885-1887, (2005).
62. Deckman, H. W. & Dunsmuir, J. H. Natural lithography. *Appl. Phys. Lett.*, **41**, 377-379, (1982).
63. Yang, S.-M., Jang, S. G., Choi, D.-G., Kim, S. & Yu, H. K. Nanomachining by colloidal lithography. *Small*, **2**, 458-475, (2006).
64. Hulteen, J. C. & Van Duyne, R. P. Nanosphere lithography: A materials general fabrication process for periodic particle array surfaces. *Journal of Vacuum Science & Technology A: Vacuum, Surfaces, and Films*, **13**, 1553-1558, (1995).
65. Zhao, Y., Shang, L., Cheng, Y. & Gu, Z. Spherical colloidal photonic crystals. *Acc. Chem. Res.*, **47**, 3632-3642, (2014).
66. Rastogi, V. *et al.* Synthesis of light-diffracting assemblies from microspheres and nanoparticles in droplets on a superhydrophobic surface. *Adv. Mater.*, **20**, 4263-4268, (2008).
67. Velev, O. D., Lenhoff, A. M. & Kaler, E. W. A class of microstructured particles through colloidal crystallization. *Science*, **287**, 2240-2243, (2000).
68. Choi, D.-G., Yu, H. K., Jang, S. G. & Yang, S.-M. Colloidal lithographic nanopatterning via reactive ion etching. *J. Am. Chem. Soc.*, **126**, 7019-7025, (2004).

69. Stelling, C., Mark, A., Papastavrou, G. & Retsch, M. Showing particles their place: Deterministic colloid immobilization by gold nanomeshes. *Nanoscale*, **8**, 14556-14564, (2016).
70. Antonietti, M., Berton, B., Göltner, C. & Hentze, H.-P. Synthesis of mesoporous silica with large pores and bimodal pore size distribution by templating of polymer latices. *Adv. Mater.*, **10**, 154-159, (1998).
71. Stein, A. & Schroden, R. C. Colloidal crystal templating of three-dimensionally ordered macroporous solids: Materials for photonics and beyond. *Curr. Opin. Solid State Mater. Sci.*, **5**, 553-564, (2001).
72. Parlett, C. M. A., Wilson, K. & Lee, A. F. Hierarchical porous materials: Catalytic applications. *Chem. Soc. Rev.*, **42**, 3876-3893, (2013).
73. Cherdhirankorn, T., Retsch, M., Jonas, U., Butt, H.-J. & Koynov, K. Tracer diffusion in silica inverse opals. *Langmuir*, **26**, 10141-10146, (2010).
74. Mikosch, A., Ciftci, S. & Kuehne, A. J. C. Colloidal crystal lasers from monodisperse conjugated polymer particles via bottom-up coassembly in a sol–gel matrix. *ACS Nano*, **10**, 10195-10201, (2016).
75. Volk, K., Fitzgerald, J. P. S., Retsch, M. & Karg, M. Time-controlled colloidal superstructures: Long-range plasmon resonance coupling in particle monolayers. *Adv. Mater.*, **27**, 7332-7337, (2015).
76. Fitzgerald, J. P. S. & Karg, M. Plasmon resonance coupling phenomena in self-assembled colloidal monolayers. *physica status solidi (a)*, 1600947, (2017).
77. Ai, B., Yu, Y., Mohwald, H., Zhang, G. & Yang, B. Plasmonic films based on colloidal lithography. *Adv Colloid Interface Sci*, **206**, 5-16, (2014).
78. Farcau, C., Giloan, M., Vinteler, E. & Astilean, S. Understanding plasmon resonances of metal-coated colloidal crystal monolayers. *Appl. Phys. B*, **106**, 849-856, (2012).
79. John D. Joannopoulos, S. G. J., Joshua N. Winn, Robert D. Meade. *Photonic crystals: Molding the flow of light*. Princeton University Press, **2008**.
80. Reculusa, S. & Ravaine, S. Synthesis of colloidal crystals of controllable thickness through the langmuir-blodgett technique. *Chem. Mater.*, **15**, 598-605, (2003).
81. Fang, Y. *et al.* Scalable bottom-up fabrication of colloidal photonic crystals and periodic plasmonic nanostructures. *Journal of Materials Chemistry C*, **1**, 6031-6047, (2013).
82. Pan, G., Kesavamoorthy, R. & Asher, S. A. Optically nonlinear bragg diffracting nanosecond optical switches. *Phys. Rev. Lett.*, **78**, 3860-3863, (1997).
83. Holtz, J. H. & Asher, S. A. Polymerized colloidal crystal hydrogel films as intelligent chemical sensing materials. *Nature*, **389**, 829-832, (1997).
84. Fenzl, C., Hirsch, T. & Wolfbeis, O. S. Photonic crystals for chemical sensing and biosensing. *Angew. Chem. Int. Ed.*, **53**, 3318-3335, (2014).
85. Ge, J. & Yin, Y. Responsive photonic crystals. *Angew. Chem. Int. Ed.*, **50**, 1492-1522, (2011).
86. Chen, M., Zhou, L., Guan, Y. & Zhang, Y. Polymerized microgel colloidal crystals: Photonic hydrogels with tunable band gaps and fast response rates. *Angew. Chem. Int. Ed.*, **52**, 9961-9965, (2013).
87. Matijevic, E. Preparation and properties of uniform size colloids. *Chem. Mater.*, **5**, 412-426, (1993).
88. Tzirakis, M. D. *et al.* Surfactant-free synthesis of sub-100 nm poly(styrene-co-divinylbenzene) nanoparticles by one-step ultrasonic assisted emulsification/polymerization. *RSC Advances*, **5**, 103218-103228, (2015).

89. Goodall, A. R., Wilkinson, M. C. & Hearn, J. Mechanism of emulsion polymerization of styrene in soap-free systems. *Journal of Polymer Science Part a-Polymer Chemistry*, **15**, 2193-2218, (1977).
90. Bolt, P. S., Goodwin, J. W. & Ottewill, R. H. Studies on the preparation and characterization of monodisperse polystyrene latices. Vi. Preparation of zwitterionic latices. *Langmuir*, **21**, 9911-9916, (2005).
91. Barrett, K. E. Dispersion polymerisation in organic media. *British Polymer Journal*, **5**, 259-271).
92. Lok, K. P. & Ober, C. K. Particle-size control in dispersion polymerization of polystyrene. *Can J Chem*, **63**, 209-216, (1985).
93. Kawaguchi, S. & Ito, K. Dispersion polymerization. *Polymer Particles*, **175**, 299-328, (2005).
94. Lee, C.-F., Young, T.-H., Huang, Y.-H. & Chiu, W.-Y. Synthesis and properties of polymer latex with carboxylic acid functional groups for immunological studies. *Polymer*, **41**, 8565-8571, (2000).
95. Slawinski, M., Schellekens, M. A. J., Meuldijk, J., Van Herk, A. M. & German, A. L. Seeded emulsion polymerization of styrene: Influence of acrylic acid on the particle growth process. *J. Appl. Polym. Sci.*, **76**, 1186-1196, (2000).
96. Shim, S. E., Cha, Y. J., Byun, J. M. & Choe, S. Size control of polystyrene beads by multistage seeded emulsion polymerization. *J. Appl. Polym. Sci.*, **71**, 2259-2269, (1999).
97. Asua, J. M. Miniemulsion polymerization. *Prog. Polym. Sci.*, **27**, 1283-1346, (2002).
98. Landfester, K. Miniemulsion polymerization and the structure of polymer and hybrid nanoparticles. *Angew. Chem. Int. Ed.*, **48**, 4488-4507, (2009).
99. Shouldice, G. T. D., Vandezande, G. A. & Rudin, A. Practical aspects of the emulsifier-free emulsion polymerization of styrene. *Eur. Polym. J.*, **30**, 179-183, (1994).
100. Fikentscher, H., Gerrens, H. & Schuller, H. Emulsionspolymerisation und kunststoff-latices. *Angew. Chem.*, **72**, 856-864, (1960).
101. Song, Z. Q. & Poehlein, G. W. Particle nucleation in emulsifier-free aqueous-phase polymerization - stage-1. *J. Colloid. Interf. Sci.*, **128**, 486-500, (1989).
102. Hamaker, H. C. The london—van der waals attraction between spherical particles. *Phy*, **4**, 1058-1072, (1937).
103. Derjaguin, B. & Landau, L. Theory of the stability of strongly charged lyophobic sols and of the adhesion of strongly charged particles in solutions of electrolytes. *Prog. Surf. Sci.*, **43**, 30-59, (1993).
104. Verwey, E. J. W. & Overbeek, J. T. G. Theory of the stability of strongly charged lyophobic sols and of the adhesion of strongly charged particles in solutions of electrolytes. *Acta Physico Chemica USSR*, **14´**, 30-59, (1941).
105. Vogel, N., Weiss, C. K. & Landfester, K. From soft to hard: The generation of functional and complex colloidal monolayers for nanolithography. *Soft Matter*, **8**, 4044-4061, (2012).
106. Napper, D. H. Steric stabilization. *J. Colloid. Interf. Sci.*, **58**, 390-407, (1977).
107. Zhang, J., Li, Y., Zhang, X. & Yang, B. Colloidal self-assembly meets nanofabrication: From two-dimensional colloidal crystals to nanostructure arrays. *Adv. Mater.*, **22**, 4249-4269, (2010).
108. Rauh, A. *et al.* Compression of hard core-soft shell nanoparticles at liquid-liquid interfaces: Influence of the shell thickness. *Soft Matter*, **13**, 158-169, (2017).

109. Reculusa, S. & Ravaine, S. Synthesis of colloidal crystals of controllable thickness through the langmuir−blodgett technique. *Chem. Mater.*, **15**, 598-605, (2003).
110. van Duffel, B., Ras, R. H. A., De Schryver, F. C. & Schoonheydt, R. A. Langmuir-blodgett deposition and optical diffraction of two-dimensional opal. *J. Mater. Chem.*, **11**, 3333-3336, (2001).
111. Dimitrov, A. S. & Nagayama, K. Continuous convective assembling of fine particles into two-dimensional arrays on solid surfaces. *Langmuir*, **12**, 1303-1311, (1996).
112. Goldenberg, L. M., Wagner, J., Stumpe, J., Paulke, B.-R. & Görnitz, E. Ordered arrays of large latex particles organized by vertical deposition. *Langmuir*, **18**, 3319-3323, (2002).
113. Vogel, N., Goerres, S., Landfester, K. & Weiss, C. K. A convenient method to produce close- and non-close-packed monolayers using direct assembly at the air–water interface and subsequent plasma-induced size reduction. *Macromol. Chem. Phys.*, **212**, 1719-1734, (2011).
114. Retsch, M. *et al.* Fabrication of large-area, transferable colloidal monolayers utilizing self-assembly at the air/water interface. *Macromol. Chem. Phys.*, **210**, 230-241, (2009).
115. Woodcock, L. V. Entropy difference between the face-centred cubic and hexagonal close-packed crystal structures. *Nature*, **385**, 141-143, (1997).
116. Bolhuis, P. G., Frenkel, D., Mau, S.-C. & Huse, D. A. Entropy difference between crystal phases. *Nature*, **388**, 235-236, (1997).
117. Wei, L., Kuo, P. K., Thomas, R. L., Anthony, T. R. & Banholzer, W. F. Thermal conductivity of isotopically modified single crystal diamond. *Phys. Rev. Lett.*, **70**, 3764-3767, (1993).
118. Olson, J. R. *et al.* Thermal conductivity of diamond between 170 and 1200 k and the isotope effect. *Phys. Rev. B*, **47**, 14850-14856, (1993).
119. Bullen, A. J., O'Hara, K. E., Cahill, D. G., Monteiro, O. & Keudell, A. v. Thermal conductivity of amorphous carbon thin films. *J. Appl. Phys.*, **88**, 6317-6320, (2000).
120. Lide, D. R. *Handbook of chemistry and physics*. CRC Press,Boca Raton, **2003**.
121. Henry, A. Thermal transport in polymers. *Annu. Rev. Heat Trans.*, 485-520, (2013).
122. Choy, C. L. Thermal conductivity of polymers. *Polymer*, **18**, 984-1004, (1977).
123. Cahill, D. G. & Pohl, R. O. Lattice-vibrations and heat-transport in crystals and glasses. *Annu. Rev. Phys. Chem.*, **39**, 93-121, (1988).
124. Asheghi, M., Kurabayashi, K., Kasnavi, R. & Goodson, K. E. Thermal conduction in doped single-crystal silicon films. *J. Appl. Phys.*, **91**, 5079-5088, (2002).
125. Marconnet, A. M., Asheghi, M. & Goodson, K. E. From the casimir limit to phononic crystals: 20 years of phonon transport studies using silicon-on-insulator technology. *J. Heat Transfer*, **135**, 061601-061601, (2013).
126. Neogi, S. *et al.* Tuning thermal transport in ultrathin silicon membranes by surface nanoscale engineering. *ACS Nano*, **9**, 3820-3828, (2015).
127. Peierls, R. Zur kinetischen theorie der wärmeleitung in kristallen. *Ann. Phys. (Berlin)*, **395**, 1055-1101, (1929).
128. Chavez-Angel, E. *et al.* Reduction of the thermal conductivity in free-standing silicon nano-membranes investigated by non-invasive raman thermometry. *APL Mater.*, **2**, 012113, (2014).

129. Hochbaum, A. I. *et al.* Enhanced thermoelectric performance of rough silicon nanowires. *Nature*, **451**, 163-167, (2008).
130. Zhou, Y. & Hu, M. Record low thermal conductivity of polycrystalline si nanowire: Breaking the casimir limit by severe suppression of propagons. *Nano Lett.*, **16**, 6178-6187, (2016).
131. Gusarov, A. V. & Kovalev, E. P. Model of thermal conductivity in powder beds. *Phys. Rev. B*, **80**, 024202, (2009).
132. Gusarov, A. V., Laoui, T., Froyen, L. & Titov, V. I. Contact thermal conductivity of a powder bed in selective laser sintering. *Int. J. Heat Mass Tran.*, **46**, 1103-1109, (2003).
133. Lu, X., Caps, R., Fricke, J., Alviso, C. T. & Pekala, R. W. Correlation between structure and thermal conductivity of organic aerogels. *J. Non-Cryst. Solids*, **188**, 226-234, (1995).
134. Little, W. A. in *From high-temperature superconductivity to microminiature refrigeration* (eds Blas Cabrera, H. Gutfreund, & Vladimir Kresin) 15-30 (Springer US, 1996).
135. Swartz, E. T. & Pohl, R. O. Thermal boundary resistance. *Rev. Mod. Phys.*, **61**, 605-668, (1989).
136. Einstein, A. Elementare betrachtungen über die thermische molekularbewegung in festen körpern. *Ann. Phys. (Berlin)*, **340**, 679-694, (1911).
137. Allen, P. B. & Feldman, J. L. Thermal conductivity of disordered harmonic solids. *Phys. Rev. B*, **48**, 12581-12588, (1993).
138. Allen, P. B., Feldman, J. L., Fabian, J. & Wooten, F. Diffusons, locons and propagons: Character of atomie yibrations in amorphous si. *Philos. Mag. B*, **79**, 1715-1731, (1999).
139. Wang, X., Liman, C. D., Treat, N. D., Chabinyc, M. L. & Cahill, D. G. Ultralow thermal conductivity of fullerene derivatives. *Phys. Rev. B*, **88**, 075310, (2013).
140. Kurabayashi, K., Asheghi, M., Touzelbaev, M. & Goodson, K. E. Measurement of the thermal conductivity anisotropy in polyimide films. *J. Microelectromech. S.*, **8**, 180-191, (1999).
141. Liu, J. & Yang, R. Tuning the thermal conductivity of polymers with mechanical strains. *Phys. Rev. B*, **81**, 174122, (2010).
142. Liu, J. & Yang, R. Length-dependent thermal conductivity of single extended polymer chains. *Phys. Rev. B*, **86**, 104307, (2012).
143. Liao, Q., Zeng, L., Liu, Z. & Liu, W. Tailoring thermal conductivity of single-stranded carbon-chain polymers through atomic mass modification. *Sci. Rep.*, **6**, 34999, (2016).
144. Shen, S., Henry, A., Tong, J., Zheng, R. & Chen, G. Polyethylene nanofibres with very high thermal conductivities. *Nat. Nanotechnol.*, **5**, 251-255, (2010).
145. Choy, C. L., Fei, Y. & Xi, T. G. Thermal-conductivity of gel-spun polyethylene fibers. *J. Polym. Sci., Part B: Polym. Phys.*, **31**, 365-370, (1993).
146. Gibson, A. G., Greig, D., Sahota, M., Ward, I. M. & Choy, C. L. Thermal-conductivity of ultrahigh-modulus polyethylene. *J. Polym. Sci. Pol. Lett.*, **15**, 183-192, (1977).
147. Wang, X., Ho, V., Segalman, R. A. & Cahill, D. G. Thermal conductivity of high-modulus polymer fibers. *Macromolecules*, **46**, 4937-4943, (2013).
148. Choy, C. L., Luk, W. H. & Chen, F. C. Thermal-conductivity of highly oriented polyethylene. *Polymer*, **19**, 155-162, (1978).

149. Choy, C. L., Wong, S. P. & Young, K. Model calculation of the thermal-conductivity of polymer crystals. *J. Polym. Sci., Part B: Polym. Phys.*, **23**, 1495-1504, (1985).
150. Hrubesh, L. W. & Pekala, R. W. Thermal-properties of organic and inorganic aerogels. *J. Mater. Res.*, **9**, 731-738, (1994).
151. Koebel, M., Rigacci, A. & Achard, P. Aerogel-based thermal superinsulation: An overview. *J. Sol-Gel Sci. Technol.*, **63**, 315-339, (2012).
152. Knudsen, M. Die gesetze der molekularströmung und der inneren reibungsströmung der gase durch röhren. *Ann. Phys. (Berlin)*, **333**, 75-130, (1909).
153. Atkins, P. W. *Physical chemistry*. Oxford University Press,Oxford, **1978**.
154. Losego, M. D., Blitz, I. P., Vaia, R. A., Cahill, D. G. & Braun, P. V. Ultralow thermal conductivity in organoclay nanolaminates synthesized via simple self-assembly. *Nano Lett.*, **13**, 2215-2219, (2013).
155. Dorcheh, A. S. & Abbasi, M. H. Silica aerogel; synthesis, properties and characterization. *J. Mater. Process. Technol.*, **199**, 10-26, (2008).
156. Feng, J., Wang, X., Jiang, Y., Du, D. & Feng, J. Study on thermal conductivities of aromatic polyimide aerogels. *ACS Appl. Mater. Inter.*, **8**, 12992-12996, (2016).
157. Fricke, J. & Emmerling, A. Aerogels. *J. Am. Ceram. Soc.*, **75**, 2027-2035, (1992).
158. Hrubesh, L. W. Aerogel applications. *J. Non-Cryst. Solids*, **225**, 335-342, (1998).
159. Cheng, W., Wang, J., Jonas, U., Fytas, G. & Stefanou, N. Observation and tuning of hypersonic bandgaps in colloidal crystals. *Nat. Mater.*, **5**, 830-836, (2006).
160. Liu, M., Ma, Y. & Wang, R. Y. Modifying thermal transport in colloidal nanocrystal solids with surface chemistry. *ACS Nano*, **9**, 12079-12087, (2015).
161. Moore, R. G. *et al.* A surface-tailored, purely electronic, mott metal-to-insulator transition. *Science*, **318**, 615-619, (2007).
162. Lyeo, H.-K. *et al.* Thermal conductivity of phase-change material ge2sb2te5. *Appl. Phys. Lett.*, **89**, 151904, (2006).
163. Ihlefeld, J. F. *et al.* Room-temperature voltage tunable phonon thermal conductivity via reconfigurable interfaces in ferroelectric thin films. *Nano Lett.*, **15**, 1791-1795, (2015).
164. Chen, R. *et al.* Controllable thermal rectification realized in binary phase change composites. *Sci. Rep.*, **5**, 8884, (2015).
165. Pekcan, O., Winnik, M. A. & Croucher, M. D. Fluorescence studies of polymer colloids .25. Fluorescence studies of coalescence and film formation in poly(methyl methacrylate) nonaqueous dispersion particles. *Macromolecules*, **23**, 2673-2678, (1990).
166. Wang, Y. C. & Winnik, M. A. Polymer diffusion across interfaces in latex films. *J. Phys. Chem.*, **97**, 2507-2515, (1993).
167. Wang, Y. C., Zhao, C. L. & Winnik, M. A. Molecular-diffusion and latex film formation - an analysis of direct nonradiative energy-transfer experiments. *J. Chem. Phys.*, **95**, 2143-2153, (1991).
168. Hahn, K., Ley, G. & Oberthur, R. On particle coalescence in latex films (ii). *Colloid. Polym. Sci.*, **266**, 631-639, (1988).
169. Hahn, K., Ley, G., Schuller, H. & Oberthur, R. On particle coalescence in latex films. *Colloid. Polym. Sci.*, **264**, 1092-1096, (1986).
170. Chen, X. *et al.* Structural reorganization of a polymeric latex film during dry sintering at elevated temperatures. *Langmuir*, **27**, 8458-8463, (2011).

171. Hu, S. S. *et al.* In-situ observation of drying process of a latex droplet by synchrotron small-angle x-ray scattering. *Macromolecules*, **41**, 5073-5076, (2008).

172. Dames, C. Solid-state thermal rectification with existing bulk materials. *J. Heat Transfer*, **131**, 061301, (2009).

173. Ben-Abdallah, P. & Biehs, S.-A. Near-field thermal transistor. *Phys. Rev. Lett.*, **112**, 044301, (2014).

174. Cahill, D. G. *et al.* Nanoscale thermal transport. Ii. 2003-2012. *Appl. Phys. Rev.*, **1**, (2014).

175. Cahill, D. G. *et al.* Nanoscale thermal transport. *J. Appl. Phys.*, **93**, 793-818, (2003).

176. Cahill, D. G., Watson, S. K. & Pohl, R. O. Lower limit to the thermal conductivity of disordered crystals. *Phys. Rev. B*, **46**, 6131-6140, (1992).

177. Nutz, F. A., Ruckdeschel, P. & Retsch, M. Polystyrene colloidal crystals: Interface controlled thermal conductivity in an open-porous mesoparticle superstructure. *J. Colloid. Interf. Sci.*, **457**, 96-101, (2015).

178. Wang, J. *et al.* Structural and optical characterization of 3d binary colloidal crystal and inverse opal films prepared by direct co-deposition. *J. Mater. Chem.*, **18**, 981-988, (2008).

179. Kommandur, S. & Yee, S. K. An empirical model to predict temperature-dependent thermal conductivity of amorphous polymers. *J. Polym. Sci., Part B: Polym. Phys.*, 1160–1170, (2017).

3 Thesis Overview

The main part of this thesis is divided into four Chapters (Chapters 4.1 - 4.4), containing two publications and two submitted manuscripts. In these chapters, polymer colloidal assemblies and their thermal transport properties play the key role. In general, bottom-up self-assembly of spherical polymer colloidal particles has been utilized to obtain highly ordered colloidal crystal monoliths (Chapters 4.1, 4.2 and 4.3), as well as disordered colloidal assemblies by using two differently sized particles during the assembly process (Chapter 4.4). Furthermore, multi-layer colloidal assemblies and binary, crystalline structures have been fabricated by choosing different methods for the assembly (Chapter 4.3). The findings of this thesis are of general relevance to other particulate systems as well. Therefore, it provides an important contribution to better understand and potentially tune thermal transport in nanostructured materials. A survey of the different topics of the subchapters is illustrated in Figure 14.

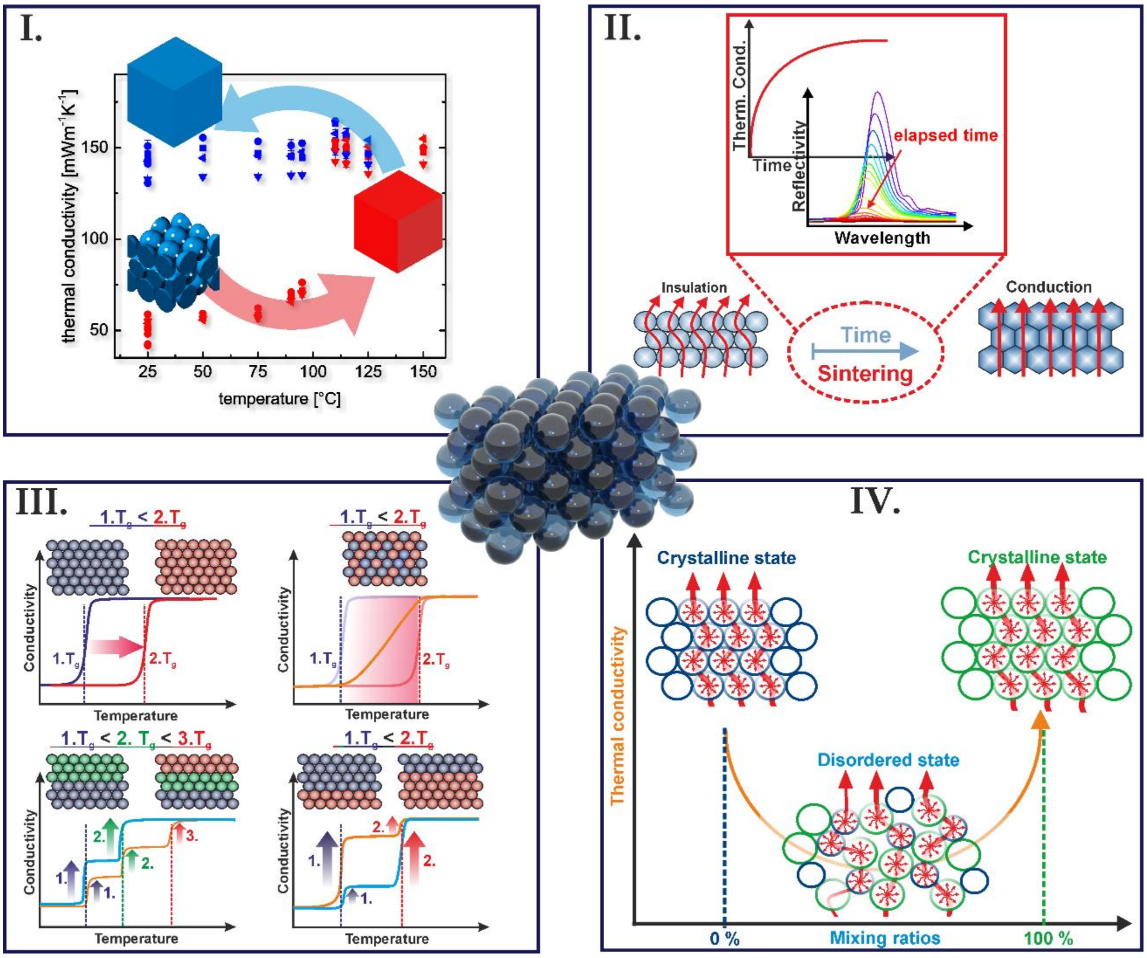

Figure 14: Summary of the different topics presented in this thesis. I.) The thermal conductivity of a polystyrene colloidal crystal. II.) Thermal transport and photonic bandgap study of the dry sintering process. III.) Polymer colloidal assemblies with tunable temperature-dependent thermal conductivity. IV.) Role of order and disorder on the thermal transport properties of colloidal assemblies.

The assembly of the particles results in an open-porous and well-defined nanostructure. The thermal conductivity through these structures is governed by the small interfaces between adjacent particles, serving as bottle necks for heat to travel through the material. This leads to a constriction-controlled heat transport. The sizes of these interfaces can be influenced by *exceeding the glass transition temperature* of the polymer particles (Figure 14. I.). Therefrom, it is possible to induce dry sintering of the colloidal assembly, which drastically increase the thermal conductivity of the structures in a step-like fashion. Such a step-like behavior is known from metal-to-insulator transitions,[161] semiconducting materials,[162] ferroelectric thin films,[163] and binary composites[164] and can contribute to the development of thermal memory or switching materials.

Since thermal transport in these structures is dominated by the interfaces, it is possible to *follow the sintering process* of polymer particle assemblies of any particle size and shape and without specific labeling (Figure **14**. II.). This is different to established experiments, were either labeling/deutering[165-169] or a sufficient particle size is necessary.[170,171]

By taking advantage of the unique temperature-dependent increase, a concept is furthermore presented how to specifically *tailor the temperature-dependent thermal conductivity* of particle assemblies (Figure 14. III.). Therefrom, the temperature-dependent behavior of the thermal conductivity can be adjusted. This is of particular importance since a tunable temperature-dependence is a major challenge in the field of thermal devices, such as thermal diodes and thermal transistors.[172,173]

Moreover, the *influence of order and disorder* within colloidal particle assemblies is investigated on binary colloidal structures (Figure 14. IV.). Here, the basic ideas known from thermal transport in crystalline[13,123,174,175] and amorphous solids[136,176] are extended to larger length scales by investigating the heat flux through ordered and disordered colloidal assemblies.

Whereas chapter 4.1-4.3 mainly focus on the dry sintering of polymer colloidal assemblies, chapter 4.4 clarifies the influence of the symmetry on the thermal transport properties of such assembly. A detailed summary of the chapters is given in the following.

The fundamental basis of this thesis has been laid in chapter 4.1. A significant portion of these result have been obtained during my master thesis in the group of Prof. Retsch from November 2013 to April 2014. Here, the thermal conductivity of a polystyrene colloidal crystal consisting of 366 nm particles has been investigated. The chapter focuses on the crystal's room-temperature thermal conductivity, the thermal conductivity behavior during the dry sintering of the particles by exceeding the glass transition temperature T_g, as well as on the sensitivity of the thermal conductivity to the gas-phase.

On the one hand, these colloidal crystals possess a low thermal conductivity in vacuum. The strong insulation behavior is based on the high interface density due to the nanostructuring, as well as the small contact area of the interparticle contact points, as discussed above. This leads to a material with a low thermal conductivity of 51 $mWm^{-1}K^{-1}$, at a comparatively high density of 750 kgm^{-3} (Figure 15a).

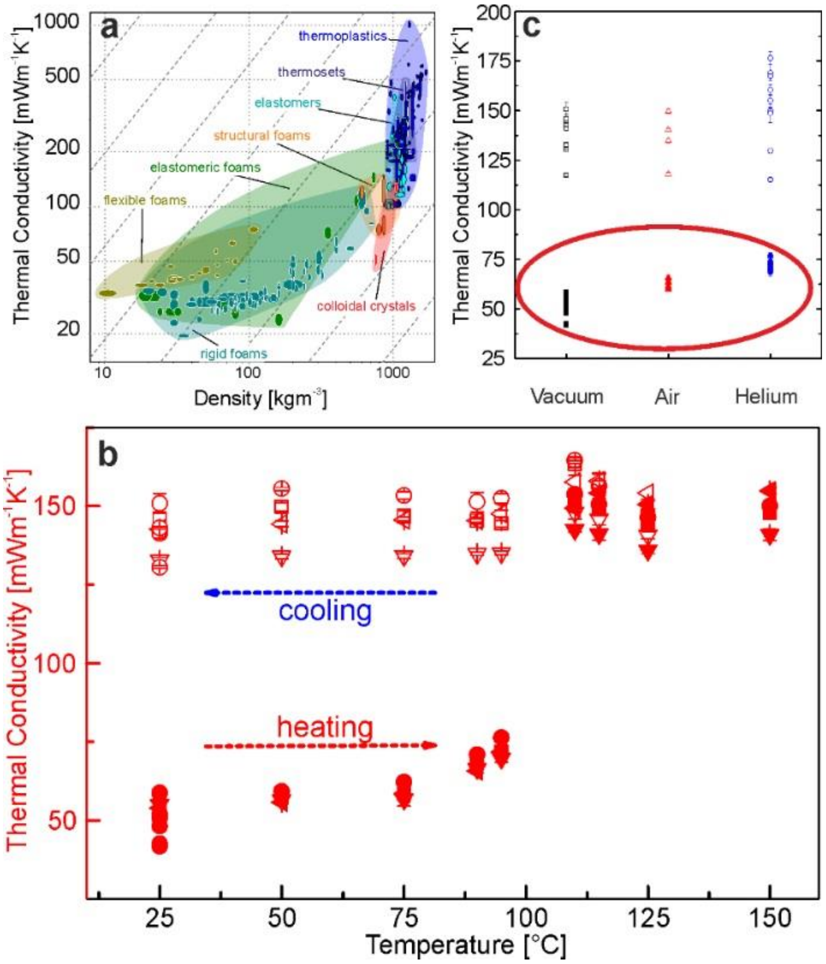

Figure 15: Thermal transport of a polystyrene colloidal crystal. a) Ashby plot of the thermal conductivity versus density. b) Temperature-dependent thermal conductivity measured in vacuum. c) The thermal transport is hardly affected by the surrounding atmosphere (red circle).[177]

Based on the influence of the interfaces, the thermal conductivity of the particle skeleton is even further reduced by ~35 %, compared to theoretical predictions by the Maxwell-Eucken equation.

On the other hand, the temperature-dependent thermal conductivity shows a drastic, irreversible increase by exceeding the T_g (~105 °C) of the polymer (Figure 15b). By exceeding T_g, dry sintering occurs, leading to a loss of porosity and an enlargement of the interparticle contact area. Therefore, the geometrical constriction for heat vanishes, resulting in an increased thermal transport. Still, this increase is irreversible owing to the thermoplastic properties of polystyrene.

Besides, the thermal conductivity of these colloidal structures is hardly sensitive to the surrounding atmosphere (Figure 15c, red circle). This is based on the small pore sizes within the open porous nanostructure. The different pore sizes present within a colloidal crystal from 366 nm spheres are schematically sketched in Figure 16.

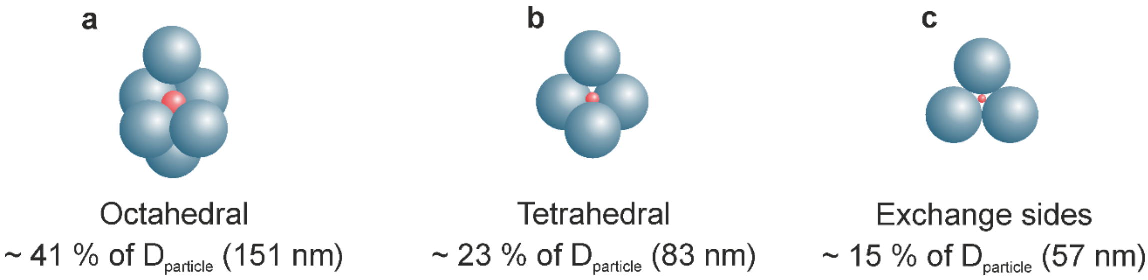

Figure 16: Different pore types present in a colloidal assembly from 366 nm spheres. The different pores can be classified into a) octahedral voids, b) tetrahedral voids and c) exchange sides.[178]

Since the present pore sizes of 151, 83 and 57 nm are in the range of the mean free path of the gas phase (He ~175 nm, Nitrogen ~65 nm), gas-wall collisions dominate, which strongly reduces thermal transport through the gas phase. Thus, the investigated colloidal crystals are nearly insensitive to the surrounding atmosphere.

The unique increase of the thermal conductivity of polymer colloidal crystals is further investigated in more detail in Chapter 4.2. Here, the focus is laid on the kinetics of the film formation process by monitoring changes of the thermal transport properties. Therefore, colloidal particles were fabricated by a statistic copolymerization of methyl methacrylate (MMA) and n-butyl acrylate (n-BA). Based on the n-BA content, the T_g of the polymer particles can be adjusted. The sintering process has been monitored by time-resolved UV-vis reflectivity and thermal transport measurements. Both methods yield a different experimental response during the colloidal film formation process at temperatures near T_g. On the one hand, the thermal transport during the sintering is mainly governed by the size of the interfaces (*constrictions for hea*t). On the other hand, the time-dependent Bragg reflectivity is mainly sensitive to volume changes affecting the refractive index contrast (*loss of porosity*). Therefrom, it is possible to extract different time constants τ, describing the film formation rate, either driven by interface or the volume changes, respectively. Even small interfacial fusion and enlargements of the contact areas strongly facilitate heat transport through the structure. In contrary, for variations in the porosity, the polymer has to flow into the voids of the structure and creeps over longer distances. Thus, less material is necessary to enlarge the interfaces than to fill the porosity of the structure. The decay of the Bragg reflectivity spectra, as well as the increasing thermal diffusivity of an n-BA-co-MMA colloidal crystal possessing a T_g at ~75 °C is illustrated in Figure 17a and b, respectively.

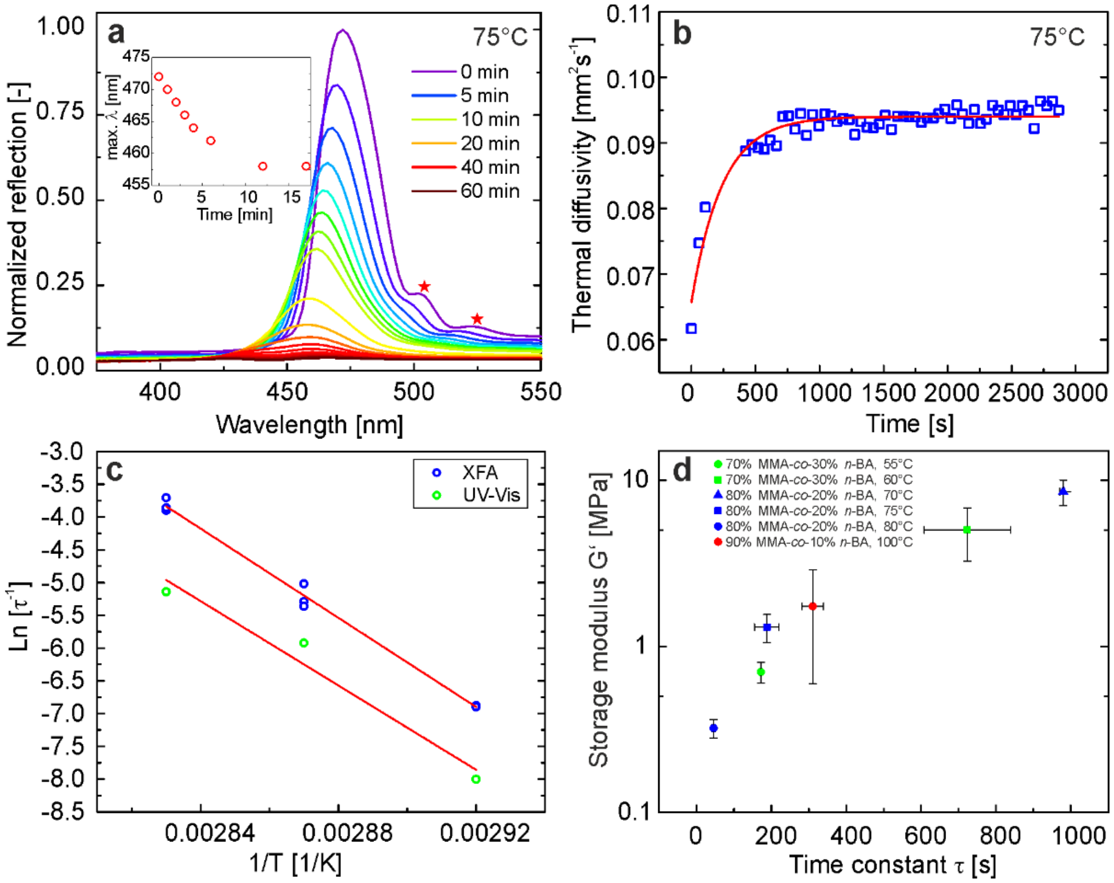

Figure 17: Following the dry sintering process of a polymer colloidal crystal with a T_g of ~72 °C. a) Decay of Bragg reflectivity peak, based on the loss of porosity during sintering. b) The thermal diffusivity increases with elapsing sintering time. (red) Single exponential fit function. c) Arrhenius plot obtained from different time constants from UV-Vis and thermal conductivity measurements. d) Correlation between viscoelastic properties and time constants, extracted from time-dependent thermal conductivity experiments.

Both, the decay of the reflectivity maximum and the increasing thermal transport behavior is well-described by a single-exponential function. Therefrom, it is possible to extract the time constant τ, to quantify the film formation process. Based on the time constants, extracted at various temperatures around T_g, it is possible to set up an Arrhenius plot from both types of experiments (Figure 17c). The offset between both experiments results from the interface or volume driven response of the thermal transport or UV-vis experiments, respectively. Noteworthy, both datasets show a linear behavior with possessing a similar slope. This reflects in similar apparent activation energies of ~270 kJmol^{-1} for the sintering process.

The time-dependent increase of the thermal diffusivity has been additionally performed near the glass transition temperature on different n-BA-co-MMA colloidal crystals with various n-BA contents. The measured time constants of the different polymer colloidal crystals are correlated to their storage modulus, shown in Figure 17d. A master curve is obtained where τ is solely depending on the viscoelastic properties of the various polymers, rather than on the polymer composition.

Whereas the step-like increase of the thermal conductivity has been studied in Chapter 4.1 and 4.2, this unique behavior is utilized to specifically tailor the temperature-dependent thermal conductivity of polymer colloidal assemblies (Chapter 4.3). Here, the precise control over the glass transition temperature of n-BA-co-MMA particles is combined with various assembly methods used for these particles. This allows to realize colloidal architectures with tailor-made temperature-dependent thermal conductivities.

In general, the thermal conductivity of crystalline materials increases with $\sim T^3$ up to the Debye temperature, and decrease at higher temperatures with $\sim T^{-1 \text{ to } -3}$ (details see Chapter 2.4).[172] In contrary, amorphous materials, e.g. polymers, possess a monotonically increasing thermal conductivity across the entire temperature range, possessing one or two plateau regimes.[179] Here, by choosing either evaporation-induced self-assembly or filtration for the assembly process, it is possible to, i) shift the step-like increase of the thermal conductivity of these assemblies to the desired temperature, ii) realize a broad transition between two temperatures, iii) introduce multi-step transitions, and iv) control the transition height of such multi-step assemblies. Furthermore, the flexibility of the presented concept is demonstrated by combining evaporation-induced and filtration assembly. The colloidal structures needed for i) and ii) are schematically sketched in Figure 18a, top row and Figure 18b, left.

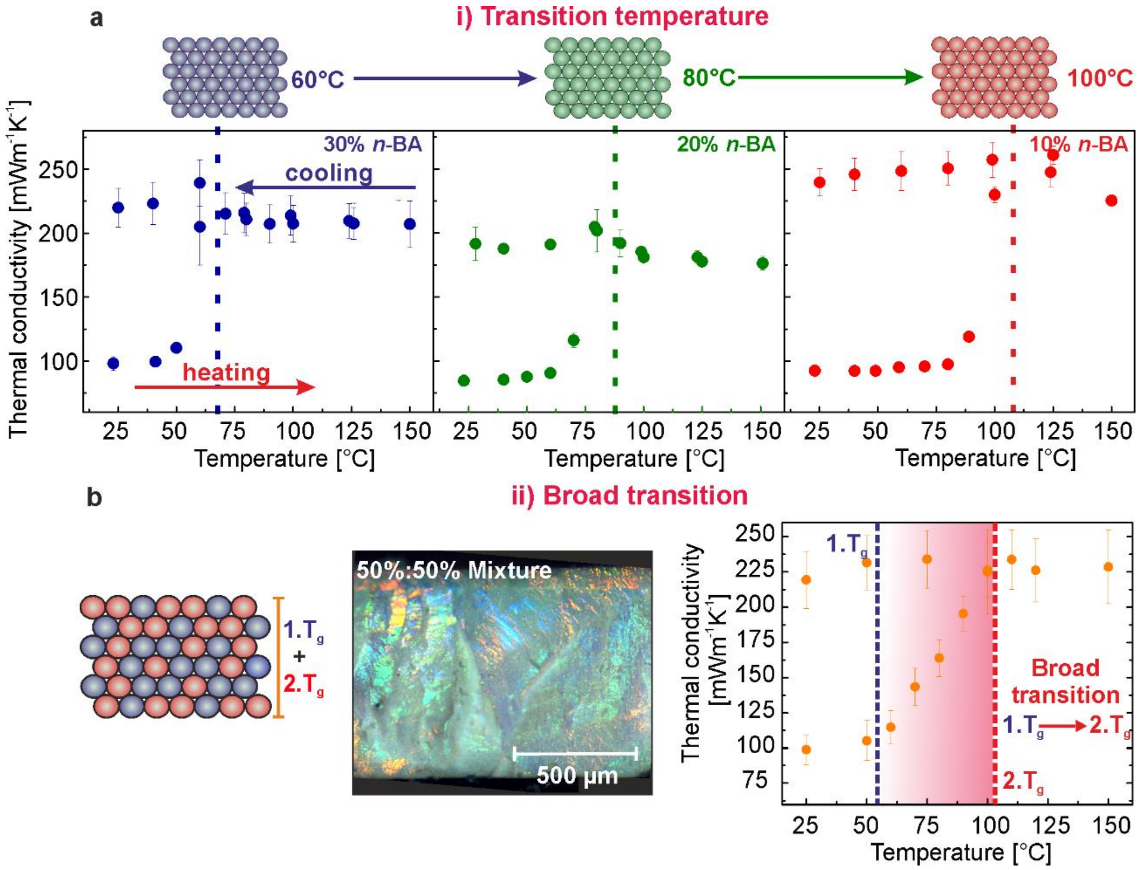

Figure 18: Tuning the transition temperature and broadening of the transition by evaporation induced self-assembly. a) Fabrication of colloidal crystals from particles possessing different T_g allows shifting the temperature-dependent increase of the thermal conductivity along the temperature axis. b) Binary co-assembly of two equal-sized particles with different T_gs. Highly crystalline monoliths are obtained (b,middle), possessing a broad increase of the thermal conductivity between both T_gs (b, right).

i) The T_g of the particles increases from blue (~54 °C) to green (~75 °C) to red (102 °C). For pure assemblies of these particles, the sharp increase of the thermal conductivity can be adjusted to a desired temperature (Figure 18a), as long as the temperatures range between the T_g of pure n-BA (~-55 °C) and pure PMMA particles (~125 °C).

ii) It is further possible to span the transition over a temperature range between two temperatures by assembling two equal-sized particles with different T_gs into a binary colloidal monolith. Based on the equal size, highly crystalline assemblies are obtainable (Figure 18b, middle), indicating a homogeneous distribution of both particle species. By exceeding the T_g of the lower melting particle the thermal conductivity of the binary assembly increases. Still, the higher melting particles partially retain the structure upon heating and therefore prevent a sharp increase in the thermal conductivity. Thus, a broad transition between both T_gs is accessible (Figure 18b, right).

iii) Using filtration as assembly method, it is further possible to fabricate discrete multilayer colloidal assemblies, in which every layer possesses a different glass transition temperature (Figure 19a, top row).

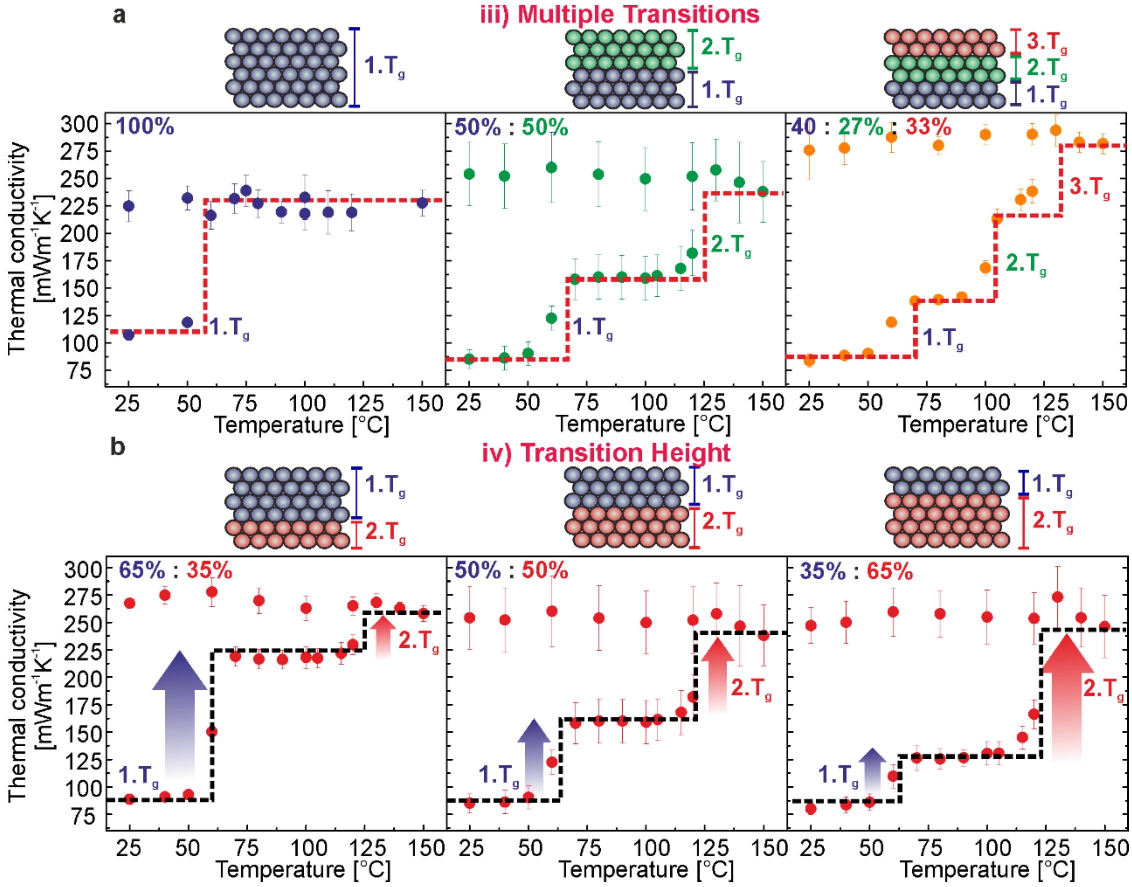

Figure 19: Introduction of multiple transition and control over transition height by filtration assembly. a) Sintering of the individual layers at their T_s leads to a multi-step increase of the thermal conductivity. b) By adjusting the layer thickness, it is possible to control the height of the increase.

By exceeding the T_gs of the individual layers, a step-like increase is observable at that specific temperature (Figure 19a, bottom row). The already molten layer becomes better conducting, resulting in a partial increase in the thermal conductivity of the assembly at that temperature. Depending on the number of different layers, double (Figure 19a, middle), or triple steps (Figure 19a, right) can be realized. In general, even more steps are introducible, as long as their glass transition temperatures are sufficiently separated. iv) Furthermore, the height of the transition at a certain T_g is controllable by adjusting the layer thickness of the specific layer during the assembly process (Figure 19b).

Finally, the flexibility of the presented concept is demonstrated by the combination of evaporation-induced and filtration assembly. The resulting colloidal architecture is sketched in Figure 20.

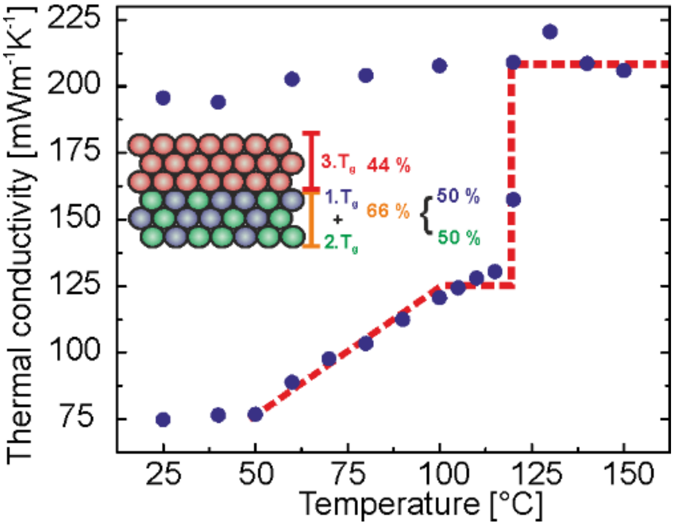

Figure 20: Combination of both assembly approaches. The bottom layer is fabricated by evaporation induced self-assembly, whereas the top layered is assembled by filtration. Therefrom, it is possible to combine a broad and sharp increase of the temperature-dependent thermal conductivity of these colloidal assemblies.

The bottom layer consists of a crystalline, binary co-assembly of particles possessing different T_gs, equal to the binary monoliths displayed in Figure 18b. After the fabrication of the bottom layer by evaporation-induced self-assembly, the top layer is stacked onto the bottom layer by filtration. This allows to combine a broad increase of the thermal conductivity between both T_gs of the bottom layer (Figure 20, between 50 °C to 100 °C), and a sharp, step-like increase of the thermal conductivity at the T_g of the top layer (Figure 20, at 125 °C).

As discussed in Chapter 4.1, the thermal transport properties of polymer colloidal crystals are governed by the small interparticle contact points. Still, the overall heat flux is additionally depending on the structural arrangement of the polymer particles within the assembly. The arrangement of the particles determines the thermal path length, which heat has to travel along through the material. By mixing two differently sized particles, it is possible to introduce disorder into the obtained colloidal monoliths. This allows studying the influence of order and disorder on the thermal transport properties of colloidal assemblies.

Optical micrographs of the edges of split of binary polystyrene colloidal crystals made from particles with D_s = 243 nm and D_l = 305 nm (size ratio ~0.8) are shown in Figure 21a, top row. The composition ranges from 0 vol% to 100 vol% of large particles.

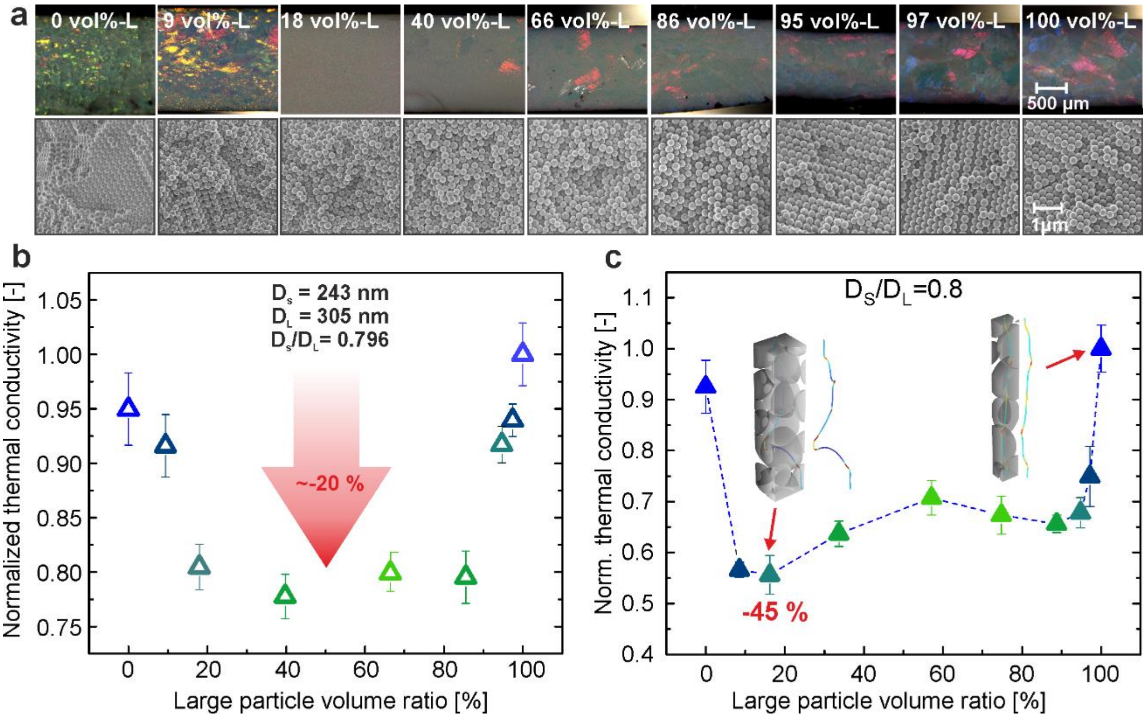

Figure 21: Thermal conductivity of binary PS colloidal assemblies. a) Optical microscopy images of the edges of the split of the colloidal monoliths with varying vol% of the large particle species. b) Thermal conductivity of these monoliths measured in vacuum. The thermal conductivity decrease by ~20 % based on the introduced disorder. c) Next neighbor analysis by FEM simulations.

A strong opalescence is observable for pure 0 vol%-L and 100 vol%-L monoliths, whereas a decreasing opalescence is visible for intermediate mixing ratios, based on a hindered crystallization of both particle species within these monoliths. This indicates a crystalline particle arrangement at the edges of the mixing diagram, and a rather random-packed structure for intermediate mixing ratios. SEM side-view images of the monoliths further prove the impression gained from optical microscopy (Figure 21a, bottom row). The normalized thermal conductivity of binary colloidal assemblies with varying volume fraction of large particles is presented in Figure 21b. High thermal conductivities can be found for crystalline assemblies (0 and 100 vol%-L) as well as for assemblies containing a small amount of differently sized species (9 and 18 vol%-L, 95 and 97 vol%-L). A reduced thermal conductivity of ~80 % of the initial value is observed for intermediate mixing ratio, and can only be partially explained by the reduced density of these assemblies (~90 %). From molecular dynamics (MD) simulations of the assembly process, it is possible to determine the number of next neighbors per particles in dependence of the mixing ratio. The mean number of neighbors rapidly drops from 12 to ~10 for intermediate mixing ratios, based on a more random packing of the particles. Thus, the structure offers less path ways for heat to travel through the assembly. The heat flux has to take a detour, leading to an elongation of the thermal transport path. Furthermore, by using finite element modeling (FEM) to calculate the thermal conductivity of binary assemblies, the random walk behavior can be qualitatively visualized by a bending of the heat flux streamlines along the structure (Figure 21c, insets). Interestingly, from FEM, a global minimum of thermal conductivity is found at mixing ratios of ~18 vol%-L, as well as a further local minimum at ~90 vol%-L (Figure 21c). Still, both mixing ratios possess a comparable mean number of neighbors of ~10. The further reduction at ~18 vol%-L can be attributed to a significantly broadening of the next neighbor distribution. Surprisingly, a maximum number of next neighbors increases at this global minimum, which is counterintuitive to the observed reduction based on a reduced number of neighors. Here, the further reduction is based on the formation particle clusters of a large particle, decorated with small particles. These clusters distort the particle lattice more strongly, leading to a further elongation of the thermal transport path, although the maximum number of next neighbors is increased. This is verified by the next neighbor distribution and the relative streamline lengths of binary mixtures, now possessing different size ratios (Figure 22a). The mixing ratio is kept constant at ~18 vol%-L to demonstrate the influence of the broadening of the next neighbor distribution at the global minimum.

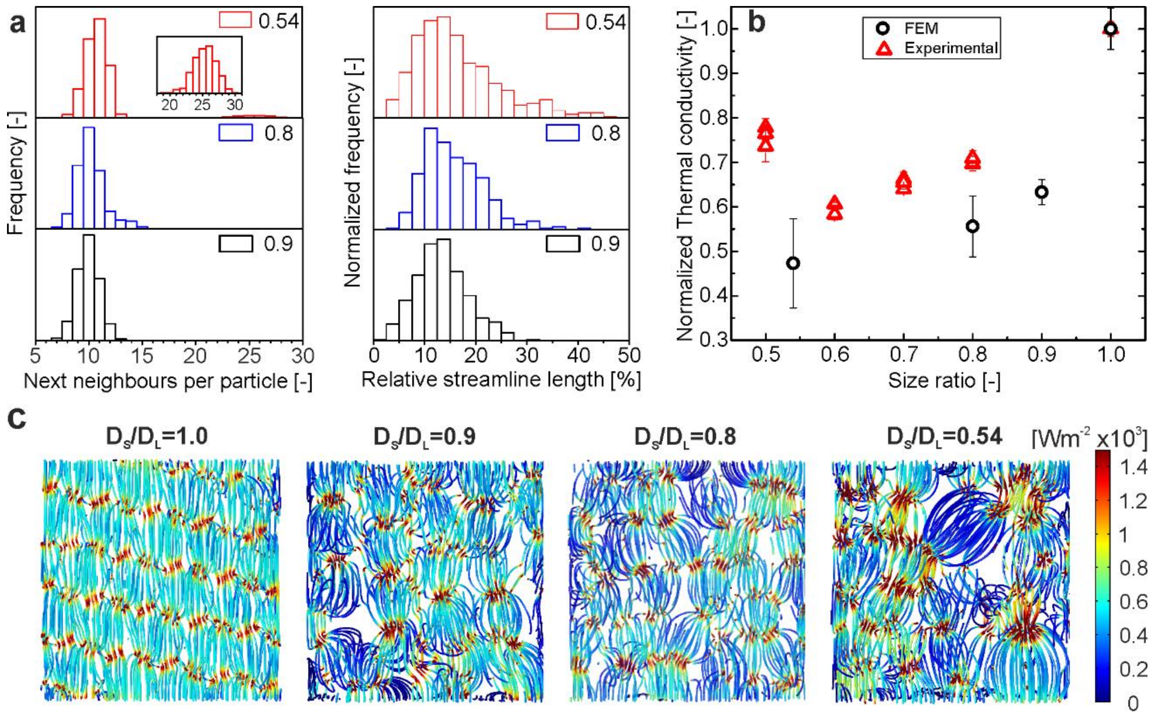

Figure 22: Influence of size ratio on the thermal conductivity of binary assemblies. a) Number of next neighbors and relative streamline length in dependence of the size ratio. Mixing ratio is 18 vol%-L. b) Influence of the size ratio of the thermal conductivity of binary assemblies. c) Heat flux density (FEM) in assemblies possessing different size ratios.

From the number of next neighbors, a further broadening of the distribution is visible with decreasing size ratio. Noteworthy, even a second population of high numbers next neighbors arises for a size ratio of 0.54 (Figure 22a, left, inset), indicating the formation of particle clusters. The relative streamline lengths are systematically shifted to longer lengths with decreasing size ratio (Figure 22a, right). This leads to an even further reduction of the thermal conductivity with decreasing size ratio, proven by experimental data and complementary FEM analysis (Figure 22b). The influence of the elongation of the thermal transport path is visualized by heat flux density images from FEM displayed in Figure 22c. A uniform heat flux density is observable for crystalline assemblies. This uniformity systematically decreases with decreasing size ratio. Based on the less and less favorable size ratio, the heat flux is bent along the particle network. This is especially visible from the heat flux density image for a size ratio of 0.54 (Figure 22c, left), where one large particle heavily constrains the heat flux density through the structure. Thus, the thermal conductivity of the assembly can be further reduced to ~44%, compared to their crystalline counterpart.

3.1 Individual Contributions to Joint Publications

Chapter 4.1: Polystyrene Colloidal Crystals: Interface Controlled Thermal Conductivity in an Open-Porous Mesoparticle Superstructure

This work is published in the Journal of Colloid and Interface Science **457**, 96-101, 2015 by F. A. Nutz, P. Ruckdeschel, M. Retsch

I performed all experiments including, material preparation and material characterization as well as data evaluation. A significant part of this work has been conducted throughout my master thesis. I corrected the manuscript.

Pia Ruckdeschel took part in discussion.

Markus Retsch supervised the work, took part in discussion and wrote the manuscript.

Chapter 4.2: Interfacial and Volumetric Sensitivity of the Dry Sintering Process of Polymer Colloidal Crystals: a thermal transport and Photonic Bandgap Study

This work is published in Physical Chemistry Chemical Physics **19**, 16124-16130, 2017 by F. A. Nutz and M. Retsch

I wrote the manuscript, and I performed all experiments including, material preparation and material characterization as well as data evaluation.

Markus Retsch supervised the work, took part in discussion and corrected the manuscript.

Chapter 4.3: Tailor-Made Temperature-Dependent Thermal Conductivity: The Power of Interparticle Constriction

This work is submitted by F. A. Nutz and M. Retsch

I wrote the manuscript, and I performed all experiments including, material preparation and material characterization as well as data evaluation. Markus Retsch supervised the work, took part in discussion and corrected the manuscript.

Chapter 0: Constricted Thermal Conductivity through Dense Particle Packings with Optimum Disorder

This work is submitted by F. A. Nutz, A. Philipp, M. Dulle, M. Retsch

I wrote the manuscript, and I performed all experiments including, material preparation and material characterization as well as data evaluation.

Alexandra Philipp was responsible for finite element modeling, took part in discussion and corrected the manuscript.

Martin Dulle was responsible for molecular dynamics simulations, took part in discussion and corrected the manuscript.

Markus Retsch supervised the work, took part in discussion and corrected the manuscript.

Main Part

4 Thermal Transport in Polymer Colloidal Assemblies

4.1 Polystyrene Colloidal Crystals: Interface Controlled Thermal Conductivity in an Open-Porous Mesoparticle Superstructure

Fabian A. Nutz, Pia Ruckdeschel, Markus Retsch*

University of Bayreuth, Physical Chemistry 1 – Polymer Systems, Universitaetsstr. 30, 95447 Bayreuth, Germany

Table of Content Figure

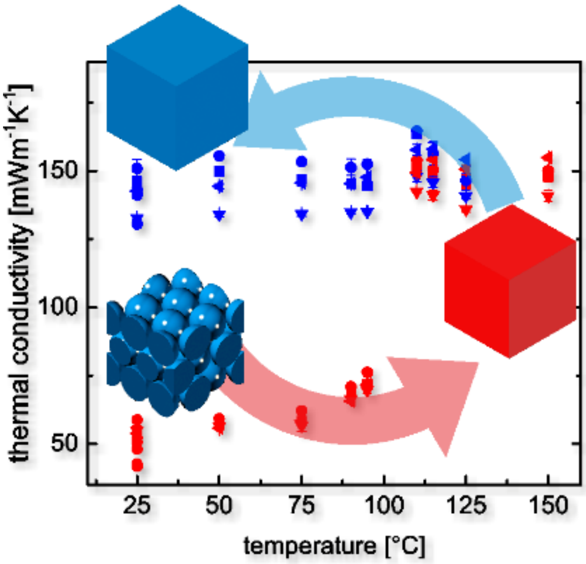

KEYWORDS: colloidal crystal; thermal boundary resistance; thermal conductivity; thermal switch; porous film

Abstract

Colloidal crystals typically consist of sub-micron sized monodisperse particles, which are densely packed on a face-centered cubic lattice. While many properties of this material class have been studied over the past decades, little is known about their thermal transport properties. The high amount of interfaces and their small interparticle contact area should result in efficient thermal insulation. Using Xenon flash analysis we report for the first time on the temperature dependent thermal conductivity of a free-standing 366 nm polystyrene (PS) colloidal crystal. Macroscopic monoliths of these samples were fabricated by colloidal self-assembly. We demonstrate a very low thermal conductivity κ of 51 $mWK^{-1}m^{-1}$ (κ of bulk PS ~140 $mWK^{-1}m^{-1}$). Remarkably, this low thermal conductivity is reached at a comparatively high density of 750 kgm^{-3}. It can be further increased by almost 300 % upon film formation and loss of the colloidal mesostructure. Additionally, this open porous structure is largely independent of the surrounding atmosphere. This can be rationalized by the small size (~100 nm) of the pores present within this colloidal crystal.

Introduction

In the light of the globally increasing energy consumption new materials and concepts are necessary to satisfy the growing demand. Nanostructured materials can become an indispensable component in this emerging field. They combine interfaces and interphases on a length scale and symmetry that can be tuned to specifically mold the flow of heat, quite analogously to the field of photonics or electronics.[1] Consequently, the interest on understanding thermal transport properties on the nanoscale has gained increasing attention over the past decade.[2] Here we investigate the thermal transport properties of polymer based colloidal crystals. The bottom-up self-assembly of these nanostructured materials allows for a good control on many of the most important parameters, i.e. length scale and interfaces. We introduce colloidal crystals as a class of highly insulating matter, however, with added functionality compared to established polymer foams or packed particle beds.

Polystyrene (PS) based materials are widely used in commercial applications for thermal insulation, most prominently as PS foam for construction insulation. Such foams possess a very low thermal conductivity, for instance Neopor® from BASF with 32 $mWm^{-1}K^{-1}$ at a density of 15 kgm^{-3}.[3] Thermal transport in such closed-cell foams is achieved by the additive contributions of solid conduction through the PS network (κ_{solid}), conduction through the gas phase (κ_{gas}), which greatly depends on the dimensions of the cellular structure, and radiation (κ_{rad}) between the hot and the cold side. In order to access even lower thermal conductivities and better insulation properties, one needs to reduce κ_{gas} by the fabrication of smaller cells and κ_{rad} by reflection or absorption of IR radiation at a maintained low density to keep κ_{solid} at a minimum.[4]

Another well-studied class of thermal insulation materials are packed powder beds. These granular materials typically consist of micro- to millimeter sized particles of various materials and shapes. Thermal transport in these materials is governed by the porosity, the mutual contact points and the environment.[5-7] Of major importance is the interfacial contribution, which consist of geometric constriction due to the contact area and the grain boundary thermal resistance.[8] In particular for inorganic powders micro-roughness on the particle interface can severely reduce the actual contact area leading to a reduced effective thermal conductivity.

Compared to state-of-the-art PS foams or powder beds, colloidal crystals have far less degrees of freedom as the three-dimensional structure is determined by the *fcc* symmetry of the crystal. Therefore the crystal density will always be at a rather high value of ~ 74 % of the constituting materials density and the interstitial space, which amounts to 26 vol%, can be considered an open porous structure.

Furthermore, in contrast to micron-sized beads the adhesion between the spheres is governed by van der Waals attraction rather than gravity and external pressure.[9]

Colloidal crystals constitute a highly periodically ordered material class, which has been well investigated over the past 30 years.[10-11] The literature on colloidal crystals offers a wide range of studies, which have been devoted to the constituting materials,[12] the assembly into (hierarchically) structured devices,[13-14] the physics involved in particle-particle interaction,[9, 15] and the usage of such ordered superstructures as templates,[16-17] sensors,[18-19] or waveguides[20] to name a few. The most prominent and well-known property of colloidal crystals is their opalescent color, which is also found in their natural counterpart – opals.[21-22] A very analogous behavior has been observed by Cheng et al. for mechanical waves in refractive index matched colloidal crystals.[23 24] In this case the periodic contrast in density leads to interference of the mechanical waves. This opens a band gap for hypersonic waves in the low GHz regime. While many physical properties of colloidal crystals have been well investigated, little is known about their thermal properties. The coherent phononic stopband observed in previous studies will certainly only play a negligible role for the transport of heat.[23-24] This is due to the very low frequency (GHz) of such phonons compared to the high frequencies necessary for thermal transport (THz). Furthermore, many polymers are glassy materials, in which consequently the mean free path of phonons is reduced to less than one nanometer. Analogously to amorphous silica, one should rather consider diffusons and propagons as well as the anharmonic coupling between localized and delocalized modes to contribute to the heat transfer process.[25-26] While typical colloidal particles in the size range from 100 nm to 1000 nm can be considered "bulk" (i.e. the thermal conductivity of the individual sphere is size-independent), the transport across the particle-particle interfaces will become the rate-determining step. Here colloidal superstructures and crystals in particular represent an excellent model system as the mutual interfaces are defined by the crystal structure. The aim of this work is to characterize the thermal transport properties of a polymer colloidal crystal for the first time, and to compare its thermal conductivity to established materials.

Materials and Methods

Materials: Potassium persulfate (KPS, ≥ 99 % Aldrich), styrene (≥ 99 %, Aldrich), 4 styrenesulfonic acid sodium salt hydrate (NaSS, Aldrich) were used as received. Water was taken from a Millipore Direct Q3UV unit for the entire synthesis and purification steps.

PS particle synthesis: Monodisperse PS nanoparticles were synthesized by emulsifier-free emulsion polymerization adapted from Ottewill.[27] The synthesis was carried out under a slight argon flow. A three-neck flask equipped with a reflux condenser and a gas inlet was charged with 240 ml milliQ water and 30 ml styrene. The mixture was heated up to 75 °C and allowed to equilibrate for 30 minutes at a stirring rate of 850 rpm. Subsequently, 5 mg of NaSS, dissolved in 5 mL milliQ water and 5 mg KPS, dissolved in 5 mL were added to the mixture. The reaction was carried out overnight. To terminate the polymerization, the mixture was exposed to ambient atmosphere. Typically, 100 mL of the received dispersion were purified by dialyzing for 3 days against 2 L of milliQ water, changing water twice a day. Our particles have a hydrodynamic diameter of 393 nm with a PDI ~ 0.008 as determined by DLS measurement. Scanning electron microscopy confirms the monodispersity and yields a dry particle diameter of 366 ± 14 nm. The surface of our PS spheres is smooth and electrostatically stabilized by the sulfate-moieties of the initiator and sulfonate groups from the added co-monomer.

Colloidal crystals: PS colloidal crystals were fabricated by evaporation induced self-assembly of the PS nanospheres. Therefore, 3 mL of a 7.3 wt% aqueous particle dispersion were allowed to slowly evaporate for several days at room temperature in a PTFE beaker. After drying, disk-shaped PS colloidal crystals were obtained with a diameter of ~2 cm.

Characterization: The particle size and size distribution were determined by dynamic light scattering (DLS) on a Malvern Zetasizer with 175° backscattering geometry. Measurements were done on strongly diluted aqueous particle dispersions.

Correlated light and electron microscopy (CLEM) were performed on a Carl Zeiss Axio Imager.A2m light microscope equipped with an AxioCam Icc 1 camera and a motorized stage, and a Zeiss Leo 1530 scanning electron microscope. The samples were transferred on a KorrMik MAT universal B sample holder. Using the shuttle & find module, it was possible to study specific spots on the specimen, which were predetermined on the optical microscope image.

Heat capacity was determined according to the ASTM E1269 standard test method on a Mettler Toledo DSC 2 under a nitrogen flow of 50 $\mathrm{mLmin^{-1}}$ and a heating rate of 20 $\mathrm{°Kmin^{-1}}$. Two heating cycles were conducted to 200°C. Only the second cycle was used for evaluation.

The thermal diffusivity of the PS colloidal crystals was measured by laser flash analysis (LFA) on a Linseis XFA 500 XenonFlash apparatus with InSb infrared detector. Previously, the thickness of the samples was determined with a Mitutoyo Litematic VL-50 and the samples were spray coated with approximately 15 μm of graphite on each side. Data evaluation was done by the software Aprosoft Laser Flash Evaluation v1.06. The received data was fitted with the given radiation fit model and manually adapted.

Results

We base our study on one particle size, namely 366 nm PS spheres (termed PS-366), which are easily accessible by emulsifier-free emulsion polymerization (details are given in the supporting information). For the determination of thermal conductivity using laser flash analysis (LFA), one needs to fabricate freestanding colloidal crystals with a size of several millimeters in lateral dimensions and several hundred micrometer in thickness. We achieved this by very slow drying of the aqueous colloidal dispersion in a PTFE beaker. Figure 1 shows the cross section optical microscope image of a typically obtained, freestanding colloidal crystal monolith. The opalescence of such a photonic crystal is clearly visible by the bright greenish coloration from top to bottom. From this macroscopic impression, one can already deduce the high crystalline order on the few hundred nanometer scale. We used correlative light and electron microscopy to investigate the structure of the colloidal crystal in more detail. Two spots at various locations within the interior of the colloidal crystal are marked in Figure 1. Both demonstrate the high degree of crystallinity with various facets of the *fcc* ordered particles being exposed to the surface. The inset on the top right corner further shows the smooth surface of the individual PS spheres as well as the small contact points between adjacent particles.

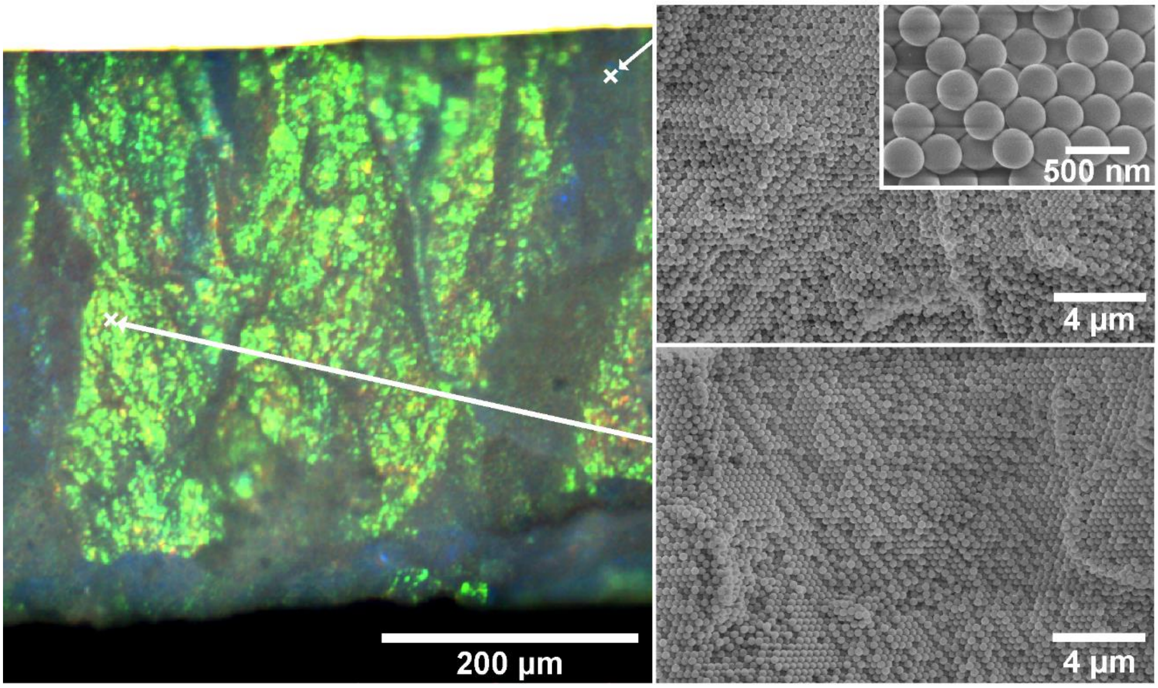

Figure 1. Bright field light microscopy image of a side view of PS-366 assembled into a 3D PS colloidal crystal (left). A strong opalescence is visible over the entire sample due to Bragg reflection. Correlated SEM images of the colloidal crystal (right) pointing out the high order of the particles within the crystal.

We fabricated several colloidal crystal monoliths, which possessed an overall film thickness ranging from 579 μm to 951 μm. The uniformity of layer thickness is an important quantity in the characterization by LFA. Based on our fabrication method, the colloidal crystal monolith always exhibits an increase in layer thickness towards the edges of the disk. This is caused by some pinning of the water meniscus at the walls of the PTFE beaker. In order to constrain the thickness variation to a minimum, we performed LFA measurements on a small spot (3 mm diameter) on the monolith. The variation in sample thickness within this area is typically less than 5 % and will therefore amount to an uncertainty in the LFA measurement of less than 10 %.

The principle method of LFA is detailed in Figure S1. The sample has to be coated with a thin layer of graphite spray on both sides (< 15 μm each). The bottom coating absorbs the light pulse and instantaneously converts it into a small increase in temperature, which then diffuses through the colloidal crystal to the colder top surface. The top coating improves the emissivity of the surface and thereby, increases the IR detector signal, which measures the time-dependent temperature increase at the top surface. A typical measurement is shown in Figure S1b along with the fit using a radiation model provided by Linseis. This fit yields the thermal diffusivity α of the colloidal crystal. Using the equation

$$\kappa(T)= \alpha(T)\cdot c_p\,(T)\cdot \varrho(T) \qquad \text{equation (1)}$$

one obtains the thermal conductivity of the sample. The temperature dependent specific heat capacity cp can be measured by DSC using a sapphire standard for calibration. The density ϱ of the colloidal crystal can be measured using a buoyancy balance. The measured value of 750 kgm^{-3} coincides with the theoretically expected value for an fcc crystal with 74 vol% of PS spheres.

As outlined above, for the case of polymer foams, various pathways can transport thermal energy. Due to the small temperature jump caused by the light pulse and the transient manner of the LFA measurement, contributions from thermal radiation are negligible. Gaseous transport can be effectively suppressed by measuring under vacuum conditions. The influence of thermal conduction through the gas phase in this open porous structure will be discussed later. Therefore, the LFA measurement in vacuum solely determines the thermal diffusivity through the polymer particle network.

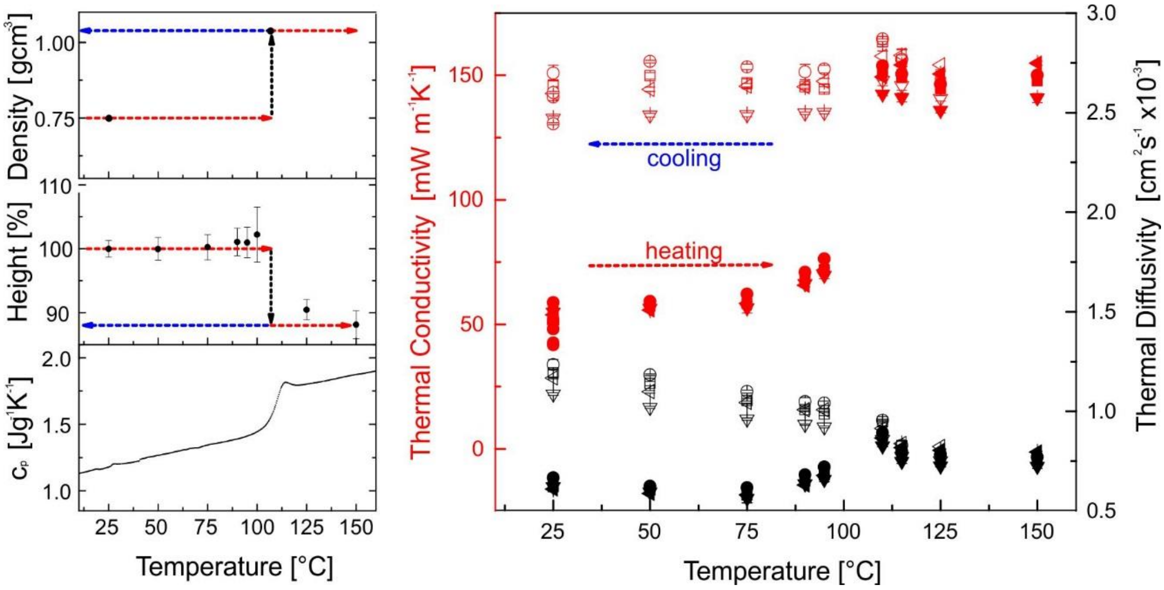

Figure 2. Left panel top: Density of the colloidal crystals determined by the buoyancy balance method, before and after T$_g$ of the PS particles. Left panel middle: Temperature-dependent measurement of the thickness of a colloidal crystal. Left panel bottom: heat capacity of the PS particles determined by DSC. Right: Temperature-dependent thermal diffusivity (black symbols) and thermal conductivity (red symbols) of a PS colloidal crystal determined by LFA in vacuum. A hysteresis between the heating (closed symbols) and the cooling cycle (open symbol) is observed.

Figure 2 summarizes all temperature dependent quantities, which need to be determined in order to measure the thermal transport properties of a colloidal crystal. When heating a PS colloidal crystal up to 150 °C, one quite expectedly losses the crystalline structure. The polymer particles soften beyond their T$_g$ at around 105 °C and start to fuse together. Side-view images (Figure S2) reveal that the particulate structure has been entirely lost, and that a continuous polymer film has been formed. In the molten film image (Figure S2 right), one can very faintly discern the former particle positions. The interstitial space has been filled with polymer, but some captured gas (micro) bubbles could still exist in this continuous polymer film. We measured the density of this molten film and found the density to essentially resemble bulk PS of $\varrho_{molten} = 1039$ kgm^{-3}. The colloidal crystal shrinks during the transition from a particulate to a continuous film. We followed this shrinkage by measuring the film thickness at various temperatures (Figure 2, left panel middle). The monolith thickness remains constant up to ~ 80 °C and slightly increases when approaching the T_g. Beyond the T_g the layer thickness drops significantly from 1094 µm to 964 µm. We found similar layer thickness reductions for all samples, which ranged between 84 % and 89 %. This is important as the layer thickness is an important parameter used during the determination of the thermal diffusivity α. For the sake of simplicity, we analyzed the temperature dependent measurement by a step function. This means during the first heating cycle, we used the thickness of the colloidal crystal at room temperature (Figure 2, red arrows). After crossing the T_g we considered the colloidal crystal to be molten and determined α by inserting the lower layer thickness. As the crystal remains in its filmed state upon cooling (Figure 2, blue arrows) the lower layer thickness is then also used for measurements below T_g.

The resulting thermal diffusivity data can be seen in Figure 2 (right panel, black symbols). Even though the data has been corrected to the reduced layer thickness, a step between the thermal diffusivity before and after the T_g can be observed. The temperature-dependent data presented in Figure 2 are obtained from five individual monoliths. Each data point represents the average of four measurements at the same spot. The deviation from sample to sample increases after the colloidal crystal has undergone film formation (Figure 2 and Figure 3b, open symbols). This can be understood by the fact that the colloidal crystals undergo a major rearrangement beyond T_g with internal stresses and potentially even cracks evolving. These changes cannot be controlled and lead to a spread in the data.

We calculated the thermal conductivity of the colloidal crystal based on α, c_p, and ρ as explained above. Analogously to the step function of the sample thickness, we also considered the density to abruptly change at the T_g and to remain constant during the cooling cycle. The result is given by the red symbols for the heating (solid symbols) and cooling (open symbols) cycle (Figure 2). At first, native colloidal crystals at room temperature demonstrate a very low thermal conductivity of $\kappa_{CC,\ 25\ °C}$ = 51 ± 6 $mWm^{-1}K^{-1}$. While this is higher compared to polymer foams or aerogels, it demonstrates the large influence of constriction and grain boundary thermal resistance to the thermal transport – in a homogenous material of high density ($\rho_{CC,\ PS}$ = 750 kgm^{-3}). Considering a parallel mixing model[28] for the case of our open porous structure, one can deduce that the thermal conductivity of the polystyrene skeleton amounts to $\kappa_{PS\ particulate}$ ≈ 69 $mWm^{-1}K^{-1}$. The influence of interfaces is quite impressively demonstrated by the marked increase in thermal conductivity beyond T_g. While the thermal conductivity remains approximately constant up to 80 °C, as it is expected for amorphous polymers,[29] an almost step-like increase occurs after exceeding the T_g, which reaches up to 148 $mWm^{-1}K^{-1}$ at 150°C. Upon cooling the thermal conductivity decreases slightly to 139 $mWm^{-1}K^{-1}$ at room temperature. A small increase close to T_g is caused by the step in the c_p. These values agree well with typical thermal transport properties of amorphous bulk polymers. From these temperature-dependent measurements one can deduce, that colloidal crystals demonstrate quite unique thermal transport properties. Firstly, even though close to the density of bulk polymers, colloidal crystals possess a very low thermal conductivity, which is on the order of polymer foams. Secondly, a rather small structural change (~15 % decrease in film thickness) is amplified to an almost threefold increase in thermal conductivity.

Figure 3a puts our new findings in relation to other well-characterized polymer classes. Colloidal crystals populate a yet empty area at the bottom right corner of an Ashby plot of density vs. thermal conductivity. It also visualizes the large increase in thermal conductivity upon film formation, which results in bulk polymer thermal conductivity.

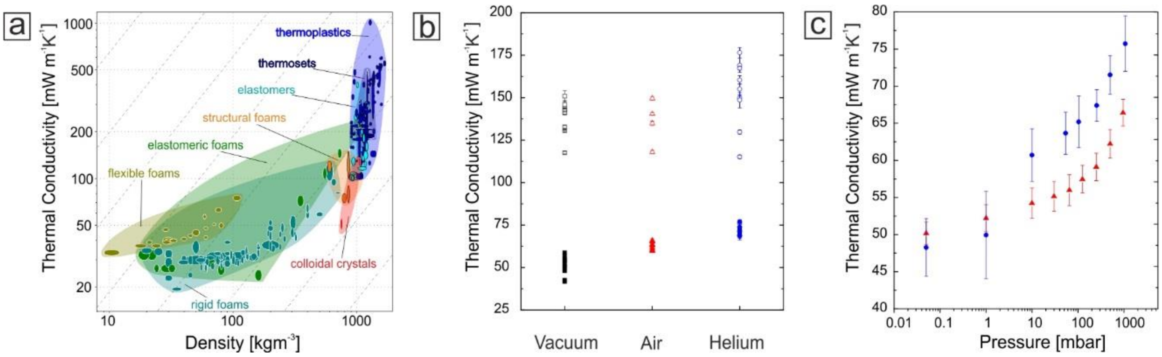

Figure 3. a) Ashby plot of the thermal conductivity of a range of polymer materials versus the density of the material. Colloidal crystals (red) populate an area of low thermal conductivity at comparatively high density, which is not accessible by other polymer materials so far. b) Influence of the environment on the thermal conductivity of a colloidal crystal. Measurements were conducted on the pristine colloidal crystals (solid symbols) in vacuum, air, and helium at 25 °C; film formation was carried out at 150 °C (open symbols). c) Pressure dependence of the thermal conductivity in air (red triangles) and helium (blue circles).

When comparing colloidal crystals to established foam materials or powder beds, one needs to consider their thermal conductivity dependence on the surrounding atmosphere. Polymer foams typically feature closed-cell pores on a length scale of several tens of micrometers. Powder beds comprise a broad range of length scales, depending on the particle size, their shape and surface roughness, but can be considered an open porous structure. Colloidal crystals also represent an open-cell structure, however, with well-defined porosity and a discrete range of void sizes given by the *fcc* symmetry.[30] We measured the effective thermal conductivity in helium and air at standard pressure (Figure 3b). For both, helium and air, a slight increase from 51 mWm^{-1}K^{-1} (vacuum) to 62 ± 2 mWm^{-1}K^{-1} (air) and 72 ± 2 mWm^{-1}K^{-1} (helium) was observed, which can be rationalized by the additional conduction contribution through the gas phase. The small difference in the effective thermal conductivity between the bad thermal conductor air (~ 26 mWm^{-1}K^{-1}) and good thermal conductor helium (~ 150 mWm^{-1}K^{-1}) indicates the influence of the small size of the open porous cells. This is corroborated by Figure 3c, where the pressure dependent thermal conductivity is shown. For the system under consideration here, the open pores can be classified into three categories, referring to octahedral, tetrahedral or connecting voids and amount to ~151 nm, ~83 nm, and ~57 nm, respectively.[30] These are extremely fine pores, which are smaller or on the order of the mean free path of gases such as He, N_2, or O_2. Consequently, the thermal conductivity through the gas phase in the colloidal crystal is greatly reduced for the case of He.[31-32] This is expected due to the Knudsen number Kn > 1 and can also be inferred from Figure 3c, where no saturation even at high pressure was observed. Based on the simple parallel mixing model the He gas conductivity was found to be only ~50 % of its bulk value. Using the same model we find an unreasonably high thermal conductivity of air ~38 $mWm^{-1}K^{-1}$, which could be due to water condensation at the contact points of adjacent spheres at ambient pressure. Upon film formation the thermal conductivity increases as outlined above to 139 ± 10 $mWm^{-1}K^{-1}$ (vacuum). A similar increase is observed for the measurement in air (132 ± 15 $mWm^{-1}K^{-1}$) and He (158 ± 14 $mWm^{-1}K^{-1}$) atmosphere. Expectedly, within the experimental error no difference between the various gases can be observed for these solid films any more.

Conclusion

In summary we characterized the thermal transport properties of a polymer colloidal crystal for the first time. This study adds significantly to the well established field of colloidal assembly structures. Despite their well-defined hierarchical structure only little is known about their thermal conductivity, yet. Our study was based on one particular example of a colloidal crystal consisting of 366 nm poly(styrene) spheres. We identified three major properties of this colloidal crystal:

The thermal conductivity is remarkably low ~ 51 $mWm^{-1}K^{-1}$, particularly in the light of the high density of ~ 750 kgm^{-3}.

Upon crossing the T_g film forming takes place. While the film thickness drops only by about 15 %, the thermal conductivity increases by about 270 %. Thus, colloidal crystals can be regarded as a single use thermal switch – at least in the range of low conducting materials.

Despite the open porous structure, the thermal insulation properties of colloidal crystals depend only slightly on the surrounding atmosphere.

We are convinced that colloidal crystals can serve as a model platform to study thermal transport properties in nanostructured materials with well-defined interfaces and contact points. Future research will be directed towards the influence of size and crosslinking of the colloidal particles to gain further control on the thermal conductivity as well as the switching behavior.

Associate Content

Supporting Information

Illustration of LFA experiment; SEM side-view images of the PS colloidal crystal before, and after melting. This material is available free of charge via the Internet at http://pubs.acs.org-

Corresponding Author

*Markus Retsch. E-mail: markus.retsch@uni-bayreuth.de. Tel.: +49 921 55-2776

Author Contributions

The manuscript was written through contributions of all authors. All authors have given approval to the final version of the manuscript. ‡These authors contributed equally.

Notes

The authors declare no competing financial interests.

Acknowledgement

We acknowledge help with the DSC measurements by Ute Kuhn and Johannes Heigl, and with correlative light and electron microscopy by Beate Förster. Pia Ruckdeschel acknowledges support by the Elite Network Bavaria (ENB). MR acknowledges financial support by the Fonds der Chemischen Industrie. Support was provided by the German Research Foundation (SFB 840). The Lichtenberg program provided by the Volkswagen foundation funded this research.

References

1. Maldovan, M., Sound and Heat Revolutions in Phononics. Nature 2013, 503 (7475), 209-217.
2. Cahill, D. G.; Braun, P. V.; Chen, G.; Clarke, D. R.; Fan, S.; Goodson, K. E.; Keblinski, P.; King, W. P.; Mahan, G. D.; Majumdar, A.; Maris, H. J.; Phillpot, S. R.; Pop, E.; Shi, L., Nanoscale Thermal Transport. Ii. 2003–2012. Appl. Phys. Rev. 2014, 1 (1), 011305.
3. BASF Neopor (R) Thermal Conductivity. http://www.plasticsportal.net/wa/plasticsEU~en_GB/portal/show/content/products/foams/neopor_thermal_conductivity (accessed 08.02.2015).
4. Glicksman, L. R.; Torpey, M.; Marge, A., Means to Improve the Thermal Conductivity of Foam Insulation. J. Cell. Plast. 1992, 28 (6), 571-583.
5. Yagi, S.; Kunii, D., Studies on Effective Thermal Conductivities in Packed Beds. AlChE J. 1957, 3 (3), 373-381.
6. Shapiro, M.; Dudko, V.; Royzen, V.; Krichevets, Y.; Lekhtmakher, S.; Grozubinsky, V.; Shapira, M.; Brill, M., Characterization of Powder Beds by Thermal Conductivity: Effect of Gas Pressure on the Thermal Resistance of Particle Contact Points. Part. Part. Syst. Char. 2004, 21 (4), 268-275.
7. Gusarov, A.; Kovalev, E., Model of Thermal Conductivity in Powder Beds. Phys. Rev. B 2009, 80 (2), 024202.

8. Poulier, C.; Smith, D. S.; Absi, J., Thermal Conductivity of Pressed Powder Compacts: Tin Oxide and Alumina. J. Eur. Ceram. Soc. 2007, 27 (2-3), 475-478.
9. Li, Q.; Jonas, U.; Zhao, X. S.; Kappl, M., The Forces at Work in Colloidal Self-Assembly: A Review on Fundamental Interactions between Colloidal Particles. Asia-Pac. J. Chem. Eng. 2008, 3 (3), 255-268.
10. Xia, Y. N.; Gates, B.; Yin, Y. D.; Lu, Y., Monodispersed Colloidal Spheres: Old Materials with New Applications. Adv. Mater. 2000, 12, 693-713.
11. Stein, A.; Schroden, R. C., Colloidal Crystal Templating of Three-Dimensionally Ordered Macroporous Solids: Materials for Photonics and Beyond. Curr. Opin. Solid State Mater. Sci. 2001, 5 (6), 553-564.
12. Lopez, C., Materials Aspects of Photonic Crystals. Adv. Mater. 2003, 15, 1679-1704.
13. von Freymann, G.; Kitaev, V.; Lotsch, B. V.; Ozin, G. A., Bottom-up Assembly of Photonic Crystals. Chem. Soc. Rev. 2013, 42 (7), 2528.
14. Mishchenko, L.; Hatton, B.; Kolle, M.; Aizenberg, J., Patterning Hierarchy in Direct and Inverse Opal Crystals. Small 2012, 8 (12), 1904-1911.
15. Israelachvili, J., Intermolecular and Surface Forces. 3rd edition ed.; Academic Press: 2010.
16. Li, Q.; Retsch, M.; Wang, J.; Knoll, W.; Jonas, U., Porous Networks through Colloidal Templates. Top. Curr. Chem. 2009, 287, 135-180.
17. Stein, A.; Wilson, B. E.; Rudisill, S. G., Design and Functionality of Colloidal-Crystal-Templated Materials—Chemical Applications of Inverse Opals. Chem. Soc. Rev. 2013, 42 (7), 2763.
18. Arsenault, A.; Fleischhaker, F.; von Freymann, G.; Kitaev, V.; Miguez, H.; Mihi, A.; Tétreault, N.; Vekris, E.; Manners, I.; Aitchison, S.; Perovic, D.; Ozin, G. A., Perfecting Imperfection—Designer Defects in Colloidal Photonic Crystals. Adv. Mater. 2006, 18, 2779-2785.

19. Holtz, J. H.; Asher, S. A., Polymerized Colloidal Crystal Hydrogel Films as Intelligent Chemical Sensing Materials. Nature 1997, 389, 829-832.
20. Rinne, S. A.; García-Santamaría, F.; Braun, P. V., Embedded Cavities and Waveguides in Three-Dimensional Silicon Photonic Crystals. Nat. Photonics 2007, 2 (1), 52-56.
21. Aguirre, C. I.; Reguera, E.; Stein, A., Tunable Colors in Opals and Inverse Opal Photonic Crystals. Adv. Funct. Mater. 2010, 20, 2565-2578.
22. Joannopoulos, J. D.; Villeneuve, P. R.; Fan, S., Photonic Crystals: Putting a New Twist on Light. Nature 1997, 386, 143-149.
23. Cheng, W.; Wang, J.; Jonas, U.; Fytas, G.; Stefanou, N., Observation and Tuning of Hypersonic Bandgaps in Colloidal Crystals. Nat. Mat. 2006, 5 (1), 830-836.
24. Still, T.; Cheng, W.; Retsch, M.; Sainidou, R.; Wang, J.; Jonas, U.; Stefanou, N.; Fytas, G., Simultaneous Occurrence of Structure-Directed and Particle-Resonance-Induced Phononic Gaps in Colloidal Films. Phys. Rev. Lett. 2008, 100 (19), 194301.
25. Larkin, J. M.; McGaughey, A. J. H., Thermal Conductivity Accumulation in Amorphous Silica and Amorphous Silicon. Phys. Rev. B 2014, 89 (14), 144303.
26. Shenogin, S.; Bodapati, A.; Keblinski, P.; McGaughey, A. J. H., Predicting the Thermal Conductivity of Inorganic and Polymeric Glasses: The Role of Anharmonicity. J. Appl. Phys. 2009, 105 (3), 034906.
27. Goodwin, J. W.; Hearn, J.; Ho, C. C.; Ottewill, R. H., Studies on the Preparation and Characterisation of Monodisperse Polystyrene Latices. Colloid. Polym. Sci. 1974, 252, 464-471.
28. Carson, J. K.; Lovatt, S. J.; Tanner, D. J.; Cleland, A. C., Thermal Conductivity Bounds for Isotropic, Porous Materials. Int. J. Heat Mass Transfer 2005, 48 (11), 2150-2158.

29. Henry, A., Thermal Transport in Polymers. In Annual Review of Heat Transfer, Begell House: New York, Connecticut, 2013; Chapter X.
30. Wang, J.; Ahl, S.; Li, Q.; Kreiter, M.; Neumann, T.; Burkert, K.; Knoll, W.; Jonas, U., Structural and Optical Characterization of 3d Binary Colloidal Crystal and Inverse Opal Films Prepared by Direct Co-Deposition. J. Mater. Chem. 2008, 18, 981-988.
31. Knudsen, M., Die Molekulare Wärmeleitung Der Gase Und Der Akkommodationskoeffizient. Ann. Phys. 1911, 339 (4), 593-656.
32. Schiffres, S. N.; Kim, K. H.; Hu, L.; McGaughey, A. J. H.; Islam, M. F.; Malen, J. A., Gas Diffusion, Energy Transport, and Thermal Accommodation in Single-Walled Carbon Nanotube Aerogels. Adv. Funct. Mater. 2012, 22 (24), 5251-5258.

Supporting Information

Polystyrene Colloidal Crystals: Interface Controlled Thermal Conductivity in an Open-Porous Mesoparticle Superstructure

*Fabian A. Nutz, Pia Ruckdeschel, Markus Retsch**

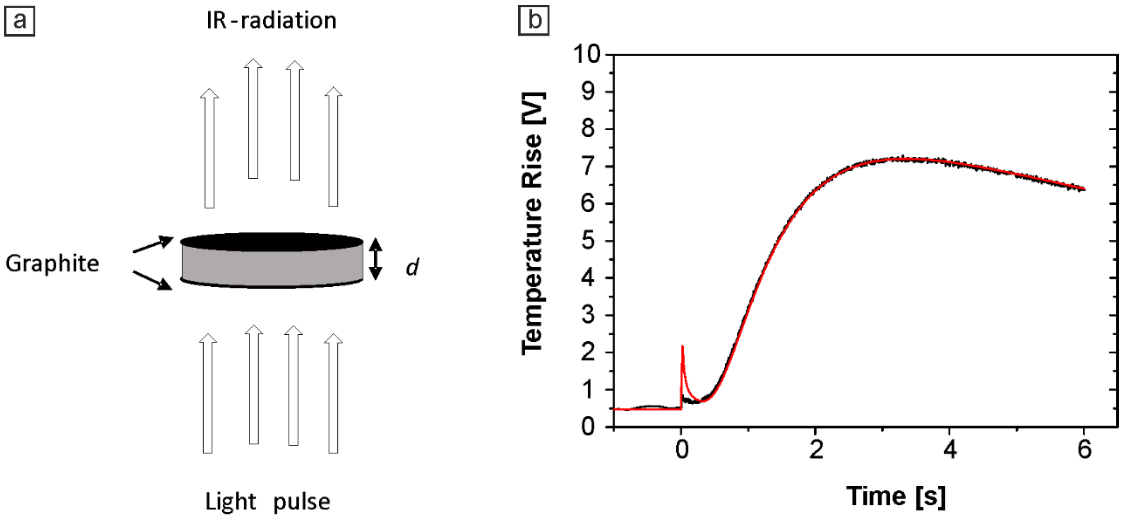

Figure S1. (a) Schematic illustration of a XFA experiment and the sample setup. Experimental data (b, black line) obtained from a single shot XFA measurement of a PS-366-CC at 25°C in vaccum. $t_{1/2}$ is received from the radiation fit function of the experimental data (b, red line).

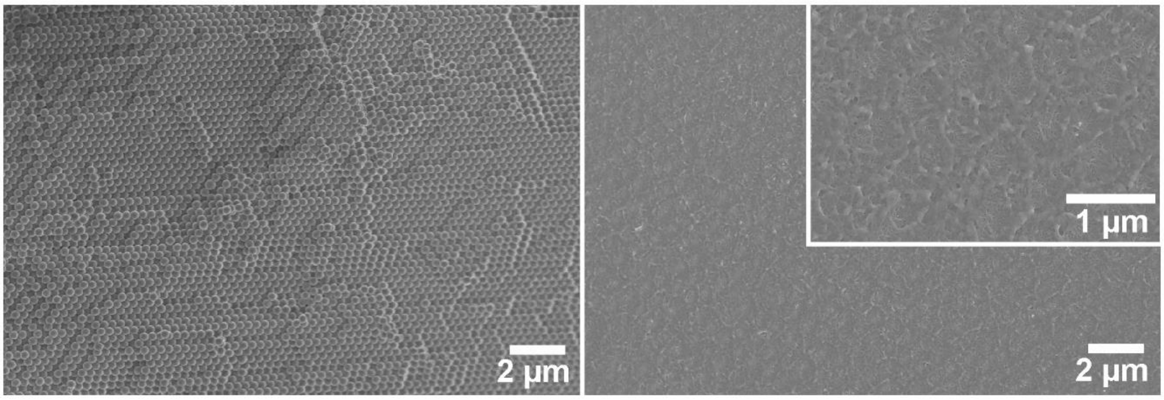

Figure S2. SEM sideview of a PS colloidal crystal before and after exceeding T_g.

4.2 Interfacial- and Volumetric Sensitivity of the Dry Sintering Process of Polymer Colloidal Crystals: A Thermal Transport and Photonic Bandgap Study

Fabian A. Nutz and Markus Retsch

University of Bayreuth, Physical Chemistry 1 – Polymer Systems, Universitaetsstr. 30, 95447 Bayreuth, Germany

Table of Content Figure

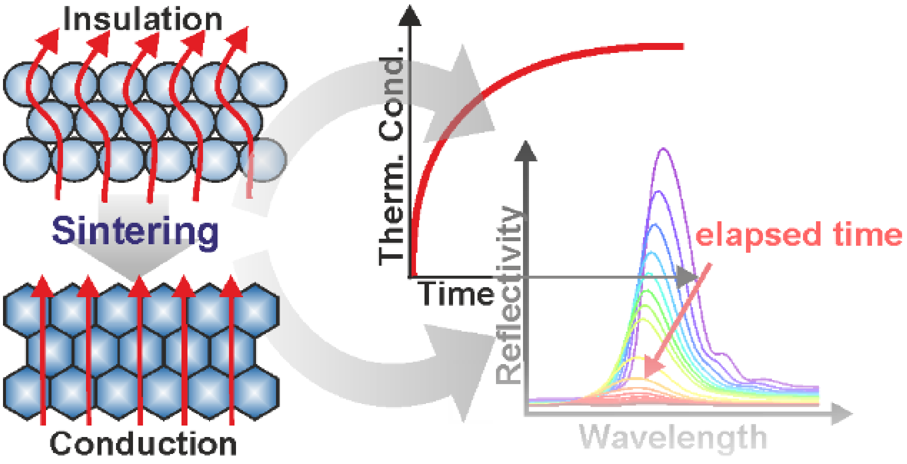

Abstract

We introduce the in-situ characterization of the dry sintering process of face-centre cubic colloidal crystals by two complementary techniques: thermal transport and photonic stopband characterization. Therefore, we employed time dependent isothermal laser flash analysis and specular reflectivity experiments close to the glass transition temperature of the colloidal crystal. Both methods yield distinctly different time constants of the film formation process. This discrepancy can be attributed to a volume- (photonic stopband) and interface-driven (thermal transport) sensitivity of the respective characterization method. Nevertheless, both methods yield comparable apparent activation energies. Finally, we extended the sintering process characterization to further polymer compositions, with vastly different glass transition temperatures. We could show that the film formation rate is governed by the viscoelastic properties of the polymers at the respective annealing temperature.

Introduction

Colloidal crystals are an intensely studied material class in the focus of a wide variety of recent research.[1-6] They are employed in many active research fields such as photonics and phononics,[7-9] lithography,[10] defined particle immobilization[11] and many more.[12] Recently, colloidal crystals have also drawn attention in the field of thermal transport in nanostructured materials.[13, 14] Due to their highly defined structure on the colloidal length scale, they can serve as a model system to get a deeper understanding of thermal transport in porous, particulate matter. Heat flow through a colloidal crystal is extremely sensitive to the size and bonding strength of the interfaces between neighboring particles. This characteristic can be utilized to trace particle dry sintering within polymer colloidal crystals at temperatures above the glass transition T_g of the polymer.

Usually, polymer colloidal crystals are formed of closed packed arrays from monodisperse polymer particles with a diameter ranging from 100-1000 nm. These crystals are predominantly assembled from aqueous particle dispersions. Based on the widespread application of particle dispersions as paints, paper coatings and adhesives, a deep understanding of film formation and particle sintering is necessary, to achieve the desired performance.[15-17] The film formation process of latex dispersions can be generally separated into three stages (see figure S1):[16] In stage I the particles self-assemble during the evaporation of water. If the particles possess a sufficient narrow size distribution, they assemble into a colloidal crystal. Stage II only happens above the minimum film forming temperature (MFT). The MFT is strongly related to the glass transition temperature T_g of the polymer. Exceeding T_g leads to the softening of the particles, allowing them to deform into dodecahedrons, where each facet is in full contact to a facet of the neighboring particles. This results in optically clear polymer films due to the loss of the refractive index contrast within the structure. For most applications, e.g. paints, the MFT is below room temperature, resulting in wet sintering of the particles as the water evaporates. If the particles possess a T_g above room temperature, the polymer is still in its glassy state and deformation of the particles is prevented during water evaporation. Heating the assembly above its T_g leads to dry sintering of the particles.[18-21] The closure of the porosity and the formation of mutual full contact areas is not only driven by the viscosity of the polymer at the specific temperature, but also by the surface tension between the water-polymer or the air polymer interface in the case of wet and dry particle sintering, respectively .[19, 22, 23] Thus, the particle deformation in stage II is additionally size dependent.[24] In stage III, polymer diffusion across the particle-particle interfaces takes place, yielding a continuous polymer film.

During the past decades, a range of methods, such as small angle neutron scattering (SANS),[25-31] direct non-radiative energy transfer (DET),[32-36] small-angle x-ray scattering (SAXS),[21, 37-40] atomic force microscopy (AFM)[19, 41, 42] and solid state NMR[42, 43] haven been established to investigate latex film formation and dry particle sintering. Most of these methods need a quite elaborate experimental setup or a specific labelling with dyes/deuterated compounds of the sample. Some of these methods are furthermore restricted to assemblies comprising a sufficient particle size.

Hence, in this work, we want to contribute to the understanding of the dry sintering process by a novel approach. Therefore, we monitor changes of the thermal transport properties of polymer colloidal crystals by time-dependent laser flash analysis (LFA) for the first time. This method is capable to follow the sintering process in-situ. It can be applied to particles of any size and no labelling of the polymers or the use of deuterated monomers is needed. Our system is based on monodisperse nanoparticles comprising a random copolymer of methyl methacrylate (MMA) and n-butyl acrylate (nBA). As we demonstrated in a recent publication on polystyrene colloidal crystals, the thermal transport in such structures is strongly governed by the small contact points between the particles.[13] These interfaces serve as geometrical constrictions for heat to travel through the material. Therefore, the size of these contact points is crucial for the thermal transport. Beyond the glass transition of the polymer, the polymer chains become mobile. This leads to a strong enlargement of the contact points between the adjacent spheres and thus, to a drastically increase of ~300 % of the thermal conductivity (Scheme 1).

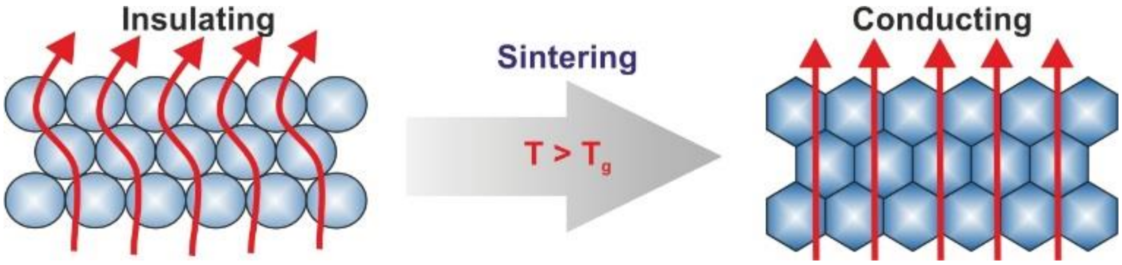

Scheme 1: Schematically illustration of the increasing thermal conductivity during sintering of a polymer colloidal crystal. Due to the small contact points, the crystals is thermally insulating at temperatures below its T_g. By exceeding T_g the particles deform into dodecahedrons with every facet in full contact to the facet of the neighbouring particle. This leads to an increased thermal transport through the structure.

Scheme 1: Schematically illustration of the increasing thermal conductivity during sintering of a polymer colloidal crystal. Due to the small contact points, the crystals is thermally insulating at temperatures below its T_g. By exceeding T_g the particles deform into dodecahedrons with every facet in full contact to the facet of the neighboring particle. This leads to an increased thermal transport through the structure.

We take advantage of this effect and trace the dry sintering of 20 vol%-nBA-co-80 vol% MMA colloidal crystals (T_g ~74 °C) at 70, 75 and 80 °C. The high ordering within the crystals additionally allows following the sintering process by time dependent UV Vis reflectivity measurements, recording the decrease of the Bragg reflection. Whereas LFA is extremely sensitive to changes at the interfaces of the crystal, UV Vis is mainly responding to volume changes, influencing the refractive index contrast. We finally show the sintering process to be independent of the polymer composition, but being mainly governed by the viscoelastic properties of the respective polymer.

Materials and methods

Methyl methacrylate (MMA, 99 %, Aldrich) and n-Butyl acrylate (nBA; ≥ 99 %, Aldrich) were purified by filtration over an alumina column (activated, basic, Brockmann I, Sigma Aldrich) prior to the synthesis. Potassium peroxodisulfate

(KPS, ≤ 99 %, Sigma Aldrich) and 4-styrenesulfonic acid sodium salt hydrate (NaSS, 99 %, Aldrich) were used as received. Throughout the synthesis and purification steps, water was taken from a Millipor Direct Q3UV unit.

Synthesis: Copolymer particles were synthesized by emulsifier free emulsion polymerization according to literature.[44] In a typical synthesis, 240 mL milliQ water and 10 mL of total monomer mixture (8 mL MMA and 2 mL n-BA for 20 %vol nBA-co-80 %vol MMA particles) were charged in a 250 mL 3-neck flask, equipped with a reflux condenser and a gas inlet. The mixture was heated to 80 °C and stirred under a constant argon flow. The mixture was allowed to equilibrate for 15 min. 10 mg of NaSS and 200 mg of KPS were separately dissolved in 5 mL milliQ water each. After equilibration, the aqueous solution of NaSS was added, and the mixture was allowed to further equilibrate for 5 min. The polymerization was started by rapidly adding the KPS solution to the mixture. The reaction was carried out at 80 °C overnight under argon atmosphere. To remove residual educts (nBA, MMA, NaSS, KPS), the particles were dialyzed against milliQ water for 3 days, changing water twice a day. For the synthesized polymers, the molecular weight can be expected to be in the range of 90 to 120 kgmol^{-1}.[45] Calculation of the theoretical glass transition temperature were done by the Fox equation assuming 100 % conversion of the monomers.

Crystal assembly: Colloidal crystals were fabricated by slowly drying a given amount of particle dispersions in a PTFE beaker for several days under ambient conditions. Disk-shaped colloidal crystals with a diameter of ~20 mm were obtained after drying (Figure 1a).

Methods

Dynamic light scattering: The hydrodynamic diameter of the particles and their size distribution were determined by dynamic light scattering (DLS) on dilute aqueous particle dispersions. Measurements were performed on a Malvern Zetasizer with 175° backscattering geometry.

Light microscopy: Bright field light microscopy images onto the edges of split of the colloidal crystals were recorded on a Carl Zeiss Axio Imager.A2m light microscope equipped with an AxioCam Icc 1 camera.

Scanning electron microscopy: Scanning electron microscopy (SEM) was performed on a Zeiss Leo 1530 electron microscope to determine the hard sphere diameter of the particles. Dilute particle dispersions were drop-casted on a silicon wafer and sputtered with 1.3 nm platinum. Additionally, side-view SEM images along the edges of split of the colloidal crystals were recorded to investigate the order of the particles within the interior of the monoliths.

Differential scanning calorimetry: Heat capacity determination was carried out on a TA Instruments Q1000 differential scanning calorimeter according to ASTM E1269. Three individual measurements were performed under a nitrogen flow of 50 mLmin-1 at a heating rate of 20 Kmin^{-1}. Two heating cycles were conducted between –40 °C and 200 °C. The specific heat capacity was evaluated from the second heating cycle. Based on the low weight content of the gas phase within the crystal, only the heat capacity of the polymer is considered in the calculation of the thermal conductivity.

Density determination: The density of the pristine colloidal crystal was determined from the mass and volume of the monolith. The mass was determined by weighting the crystals. The volume was measured on a Keyence V 3100 3D digital macroscope. The density of the molten crystals has been obtained by a buoyancy balance according to Archimedes principle.

Rheology: The storage and loss modulus of the polymers were determined using oscillating rotational rheology with plate to plate geometry at a frequency of 1 rad/s in a temperature range of 25 to 150 °C. Measurements were performed on disk-shaped samples with a diameter of 8 mm. Strain sweeps were performed before the measurements to determine the linear viscoelastic regime of the samples (Figure S5). The samples were prepared by hot-pressing dry nanoparticle powder at 150 °C in a vacuum hot-press, to ensure no enclosure of air bubbles within the samples.

UV-VIS: Temperature-dependent UV-Vis reflectivity measurements were conducted on an Agilent Cary 5000 with Universal Measurement Accessory equipped with a heat stage. UV Vis experiments were carried out on colloidal crystals, dip coated from a 3 wt% particle dispersion on 170 μm glass slides. Reflectivity spectra were recorded from 350-550 nm at an angle of 10° between sample and incident light beam. The range of the detected wavelength is chosen as such to detect Bragg reflection of the colloidal crystals.

Laser flash analysis: Laser flash analysis was performed on a Linseis XFA 500 XenonFlash apparatus equipped with an InSb infrared detector to obtain the thermal diffusivity α of the colloidal crystals. Previous to the measurement the sample surfaces were coated with a 100-200 nm metal layer. The metal layer serves as an optical blocking layer and prevents light transmission through the colloidal crystal. Additionally, the samples were coated with a thin graphite layer (< 15 μm) to ensure a good absorbance at the bottom, and a high emissivity at the top side of the sample. Due to the small thickness of the coating, compared to the sample thickness (~800 μm) the influence of the coating on the measurements is negligible. Measurements were performed in helium atmosphere at a pressure of 950 mbar to ensure a homogenous temperature distribution inside the sample chamber. The raw data was fitted with the radiation fit model provided by the software Aprosoft Laser Flash Evaluation v.1.06. Measurements were performed on at least three samples.

Thickness determination: The thicknesses of the colloidal crystals were determined on a Mitutoyo Litematic VL-50 equipped with a heat stage. The sample thickness was measured before and after each laser flash experiment. For time-dependent thickness determination, a home built heat stage was used to provide a comparable thermal environment to the laser flash measurements.

Results and discussion

Copolymer particles with a diameter of 214 ± 7 nm determined by SEM were synthesized by emulsifier free emulsion polymerization. Colloidal crystals of these particles were self-assembled by drying the dispersion at ambient conditions. Typically, disc shaped free standing colloidal crystals with a thickness of several hundred micrometers and a diameter of ~20 mm were obtained with this method (Figure 1a).

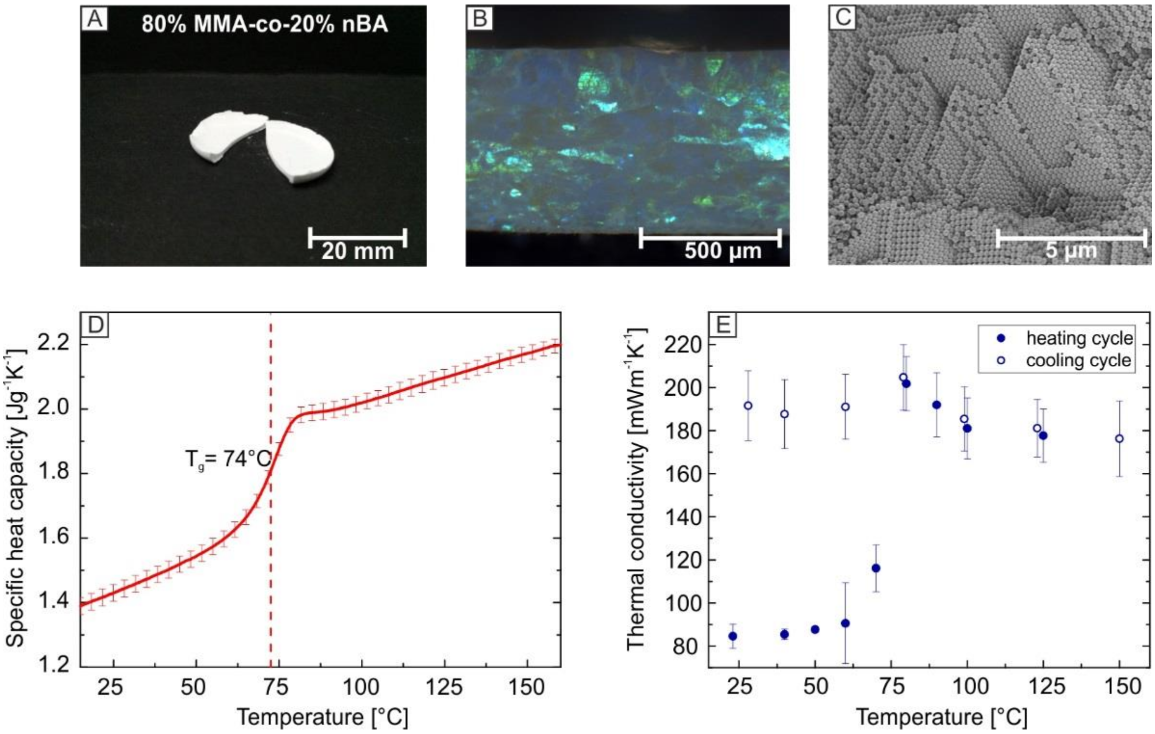

Figure 1. a) Photograph of a free-standing, self-assembled colloidal crystal monolith. b) Side view optical microscopy image along the edge of a split colloidal crystal. The opalescence is indicative of a high crystalline order. c) Side-view SEM image of the interior of the colloidal crystal monolith confirming the long range, crystalline order. d) Temperature dependent heat capacity of 20 vol% nBA-co-80 vol% MMA possessing a glass transition temperature of ~74 °C. e) Temperature dependent thermal conductivity of the colloidal crystal. By exceeding T_g of the polymer a drastic increase of the thermal conductivity is visible.

Optical microscopy side-view images of typically obtained monoliths are shown in Figure 1b. A strong opalescence is visible throughout the entire monolith. This demonstrates the high order of the particles within the crystal on a length scale of several hundred micrometers. SEM confirms the high degree of crystallinity of the crystal (Figure 1c). From optical microscopy and SEM, the samples under investigation can be regarded as fully crystalline. The polymer microstructure, however, is of course in a completely amorphous state due to the atactic polyacrylate backbone.

The temperature dependent heat capacity of the copolymer is displayed in Figure 1d. A glass transition temperature of ~74 °C can be determined (Figure 1d, dashed line). This is in perfect agreement with the prediction of 74 °C, calculated by the Fox equation.

The thermal conductivity of such monoliths was measured by laser flash analysis. A schematic setup of this method and details about the measurement can be found in Figure S2. A typical measurement to obtain the thermal diffusivity is finished after roughly 10 seconds, depending on the thickness of the crystals. The temperature dependent mean thermal conductivity of three individual samples is presented in Figure 1e. 20 vol% nBA-co-80% MMA colloidal crystals show a low thermal conductivity of 84 ± 2 $mWm^{-1}K^{-1}$ at 25°C. By exceeding the T_g of the constituting polymer, the mobility of the polymer chains strongly increases, resulting in a fast sintering of the particles. Consequently, the thermal conductivity of the crystal increases in a step-like, irreversible fashion due to a strong enlargement of the particle-particle interfaces.

To investigate the dry sintering process, this transition is monitored by isothermal, time-resolved LFA and UV-VIS reflectivity measurements at temperatures close to the glass transition temperature. The dry sintering was followed at 70, 75 and 80 °C. For time-dependent laser flash analysis, the changes in sample thickness have to be assessed separately (for details see supporting information, figure S3a). The time dependent behavior of a laser flash raw signal and the intensity of the Bragg peak at 75 °C are displayed in Figure 2a and b.

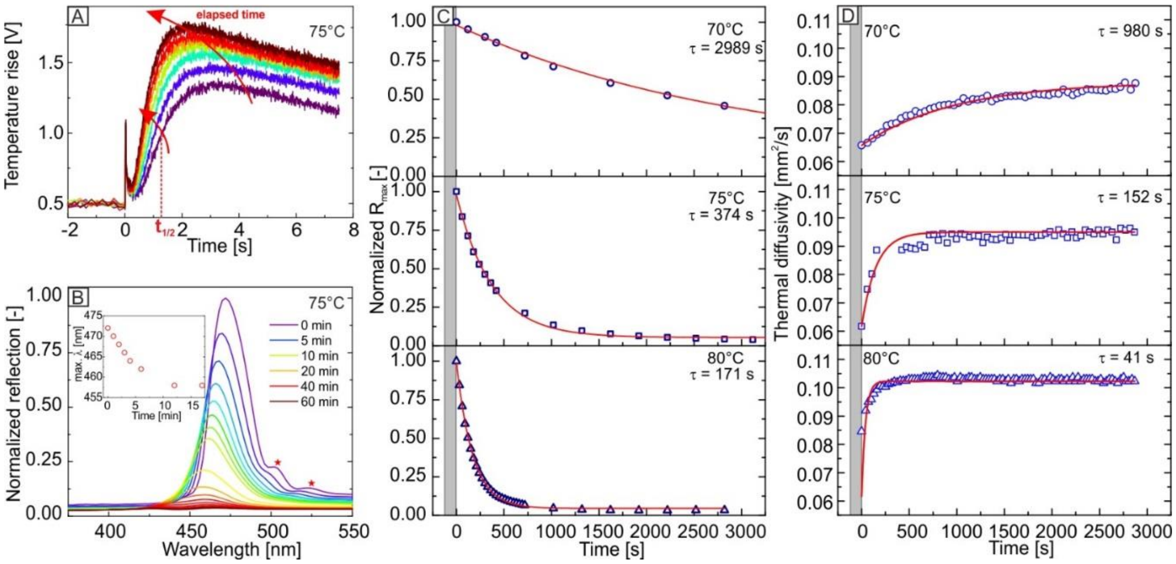

Figure 2. a) Time-dependent XFA raw signal. With elapsing time, the signal intensity is increasing and its maximum is shifted to shorter times caused by the sintering process. b) Decay of the Bragg peak of the colloidal crystal due to the loss of refractive index contrast. Inset: blue shift of the peak maxima based on the shrinking of the unit cell during sintering at 75 °C. c) Time-dependent decrease of the maximum reflectivity at the specified temperature. d) Time dependent increase in thermal diffusivity obtained by laser flash analysis at 70, 75 and 80 °C. From both experiments, τ decreases with increasing temperature.

For both methods a qualitatively comparable behavior could already be deduced by the time dependent laser flash raw signal and the reflectivity spectra. The laser flash raw signal (Figure 2a) increases in signal intensity with elapsing time. This is based on a decrease of crystal thickness due to the loss of porosity during film formation. Moreover, the signal maximum is shifted to shorter times. This time shift arises from an increased thermal transport through the sample due to the enlargement of the particle-particle interfaces. This leads to smaller $t_{1/2}$ values and thus, to an increase of α with elapsing time.

An intense Bragg peak of the neat colloidal crystal with a maximum at a wavelength of 473 nm is visible at the beginning of the experiment (Figure 2b). This maximum corresponds to a colloidal crystal formed by particles with a diameter of 213 nm calculated by Bragg`s law, assuming an *fcc*-symmetry and an effective refractive index of 1.379 for the structure. This is in very good agreement with the experimental particle diameter of 214 ± 7 nm determined by SEM. In addition, the spectra exhibit Fabry-Pérot fringes (Figure 2b, red stars) caused by interference of light waves, reflected at the crystal/air and crystal/substrate interface. This indicates a high order and homogeneity of the sample. With increasing annealing time, the intensity of the Bragg peak decreases. This is caused by the onset of polymer flow into the voids of the crystal. Due to the resulting loss of porosity, the refractive index contrast vanishes, leading to a decreasing Bragg peak intensity. Additionally, a blue shift of the peak\`s maxima is visible in the spectra. The evaluation of blue shift of the peak maxima for UV-Vis experiments at 75 °C is displayed in the inset for Figure 2b, for the first 1000 s. At longer sintering times, the allocation of the peak maxima was not possible due to peak broadening. The blue shift can be ascribed to the deformation of the polymer particles into dodecahedrons during the sintering, leading to an isotropic shrinking of the crystal's unit cell. Therefore, the lattice parameter of the crystal decreases, indicating a blue shift of the spectra.

The time-dependent decay of the maximum intensity of the Bragg peak at 70, 75 and 80 °C are shown Figure 2c. The grey area marks the time needed for thermal equilibration. The isothermal condition was typically reached within 2 minutes. We found the decrease of the Bragg peak intensity to follow a single-exponential behavior (Figure 2c, red lines). The fit function yields a time constant τ, which is utilized to describe the rate of the film formation process at different temperatures. With increasing annealing temperature, the decay rate of the Bragg peak increases. This results in a decrease of the extracted time constants. Noteworthy, the Bragg peak reflectivity of the colloidal crystal vanished almost completely after ~50 minutes for annealing temperatures of 75 °C and 80 °C, whereas a strong reflection remains within the spectra for measurements at 70 °C (Figure 2c). This is based on a preserved crystalline structure within the sample, as shown by SEM side view micrographs in figure S3b of the annealed colloidal crystal. For crystals sintered at 70 °C, it is still possible to deduce the crystalline structure as well as the original, spherical shape of the particles. For samples annealed at 75 °C and 80 °C, one is able to retrace the lattice planes but the interstitial voids between the particles are completely filled with polymer.

The thickness-corrected, time-dependent thermal diffusivity measured at 70, 75 and 80 °C, is displayed in Figure 2d. Within the equilibration period (grey area), it was not possible to perform any measurement. For every time dependent isothermal series, the thermal diffusivity α of the colloidal crystals exhibit a comparable behavior. Whereas α strongly increases in the first minutes of the experiment, it plateaus after a certain period. The obtained thermal diffusivity consequently follows a single exponential behavior for each isothermal condition (Figure 2d, red line). Analogously to the UV-Vis experiment, τ decreases with increasing temperature. This can be ascribed to a higher mobility of the polymer chains at higher temperatures, which results in a faster enlargement of the interparticle contact points and therefore, to a faster increase of the thermal transport through the structure.

The time constants τ from the UV-Vis measurement are significantly higher than the values received from XFA, indicating a slower sintering process, observed by the UV-Vis experiments. We attribute this predominantly to the following reason: The thermal transport properties of the colloidal crystal are mainly driven by the interfaces between the polymer particles. Even small changes at these interfaces by a slight interfacial fusion of the polymer can already lead to a strongly increased thermal diffusivity through the structure. On the contrary, the film formation process monitored by UV-Vis is driven by changes of the volume affecting the porosity of the structure. The polymer has to flow into the voids of the crystal structure to induce a change of the refractive index contrast. In this case, the polymer needs to creep over longer distances and a larger amount of material needs to start moving in order to affect the crystal's reflectivity. It is further important to note that, despite the macroscopic dimensions of the colloidal crystal film, the sintering process happens homogeneously throughout the bulk of the colloidal crystal.

We can use the temperature-dependent rate constants ꩜ to determine an apparent activation energy E_a for the relaxation of the polymer. The Arrhenius plot based on the extracted $1/\tau$ values of both, UV Vis and XFA experiments is displayed in Figure 3a. The values from XFA are systematically located at higher values than the data received from UV-VIS due to the higher interfacial sintering rate. Both data sets show a linear behavior. From the slope of the linear fit (Figure 3a, red lines), E_a can be determined according to the Arrhenius equation. We found E_a from UV Vis and XFA to be almost equal with 268 and 283 kJ/mol, respectively. Therefore, both methods yield a comparable, apparent activation energy for the sintering process, but constitute distinctly different pathways. The interfacial fusion happens about three time faster than the bulk void filling.

The received E_a values are comparably high. This can be ascribed to several reasons. First, the relaxation of the polymer at temperatures near T_g can be understood as a beginning cooperative intermolecular motion. Since the measurements were performed only slightly above T_g, this process might consume high energies due to the beginning entanglement of the nearly glassy polymer chains. Second, the temperature range used for the linear fitting is quite limited, which can lead to an only apparent linear behavior of the data. Third, since the measurements were performed on an amorphous polymer close to T_g, the viscosity might rather follow a Williams-Landel-Ferry behavior than an Arrhenius behavior.

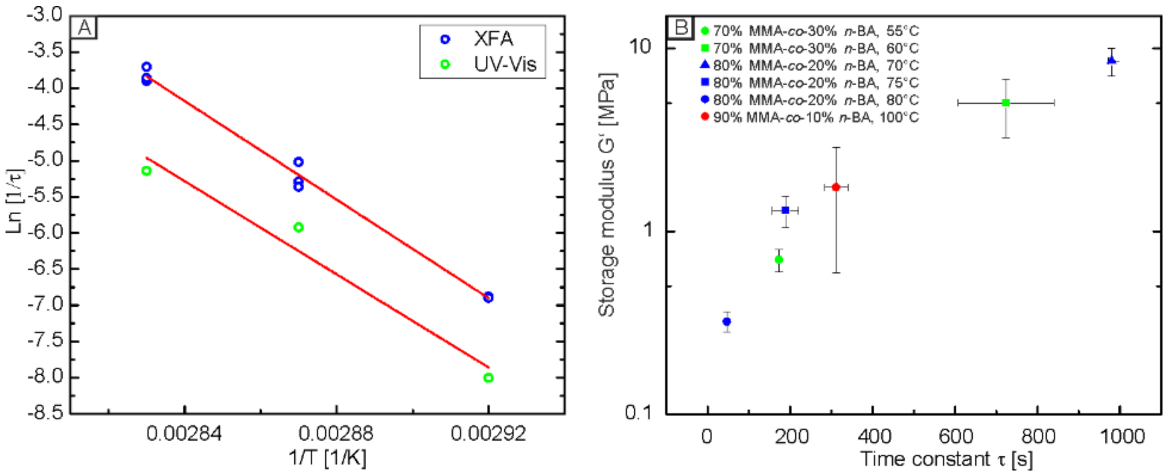

Figure 3: a) Arrhenius plot based on the fitted τ values from time-dependent UV-Vis (green) and XFA (blue) experiments. Whereas the absolute 1/τ values differ between the XFA and UV-Vis experiment, the respective slopes are comparable. b) Correlation between the storage modulus and time constants τ, obtained from laser flash analysis. τ strongly depends on the viscoelastic properties of the polymer rather than its composition.

In a further step, we correlated the results obtained by XFA with the viscoelastic properties of three other nBA-co-MMA colloidal crystals possessing different polymer compositions. By varying the nBA content between 10 to 30 vol% the glass transition can be shifted to lower temperatures, according to the Fox equation. The sintering process should be independent of the actual polymer composition, but it certainly depends on the viscosity of the polymer at a given temperature. Moreover, it depends on the surface tension between the air-polymer interface[22, 23] and consequently on the particle size.[24] The differently composed particles were synthesized such that they all possess an almost equal diameter ranging between 182 nm and 215 nm. Thus, the influence of the surface tension is nearly negligible for the comparison of the sintering process of the differently composed colloidal crystals. Furthermore, based on the emulsion polymerization process used, one can also expect comparable high molecular weights among all polymer compositions.[45]

The temperature dependent storage and loss moduli of the investigated polymers are shown in Figure S5b. All copolymers under investigation show a similar G′ and G′′ temperature dependence, which is typical for amorphous, thermoplastic polymers. Depending on the nBA content of the polymer, the moduli are shifted to lower temperatures. This is in accordance with a decreasing glass transition temperature with increasing nBA content (100 °C, 74 °C, and 52 °C for 10, 20, and 30 vol% nBA, respectively). We then correlate the obtained time constants τ with the temperature dependent storage modulus G′ of the polymer (Figure 3b). A master-curve is obtained for all polymer compositions, where τ only depends on the storage modulus in a monotonic, but non-linear way. Thus, the temperature dependent viscoelastic properties of the constituting polymer can be used to estimate the time needed for the interface- and volume-driven sintering process.

Conclusion

We investigated the dry sintering process of well-ordered colloidal crystals via two label free and size-independent methods. Using UV-Vis spectroscopy to monitor changes in the refractive index environment and laser flash analysis to monitor changes of the thermal diffusivity through such a colloidal ensemble, we were able to follow the film formation in real time. We find a comparable film formation activation barrier for both cases of about 270 kJ/mol. The characteristic film formation rate can be described by a time constant τ. This time constant decreases with increasing temperature relative to the T_g of the polymer under investigation. The time constants obtained from the UV-Vis experiment is systematically higher compared to the XFA analysis, which we attribute to the difference between an interface- and a volume-driven response. Finally, using three different polymer compositions, we were able to show that the film formation rate is only a function of the viscoelastic properties of the polymers forming the particles. We are convinced that the analysis of thermal transport properties will be used in the future for the characterization of other particulate systems, where not only kinetic but also structural information is necessary.

Acknowledgements

The authors thank Ute Kuhn for help with DSC and rheological experiments. This project was funded by the Volkswagen Foundation (Lichtenberg professorship). Additional support was provided by the SFB840.

References

1. K. R. Phillips, G. T. England, S. Sunny, E. Shirman, T. Shirman, N. Vogel and J. Aizenberg, Chem. Soc. Rev., 2016, 45, 281-322.
2. N. Vogel, M. Retsch, C. A. Fustin, A. Del Campo and U. Jonas, Chem. Rev., 2015, 115, 6265-6311.
3. Y. N. Xia, B. Gates, Y. D. Yin and Y. Lu, Adv. Mater., 2000, 12, 693-713.
4. J. F. Galisteo-López, M. Ibisate, R. Sapienza, L. S. Froufe-Pérez, Á. Blanco and C. López, Adv. Mater., 2011, 23, 30-69.
5. A. Stein and R. C. Schroden, Curr. Opin. Solid State Mater. Sci., 2001, 5, 553-564.
6. S. Wong, V. Kitaev and G. A. Ozin, J. Am. Chem. Soc., 2003, 125, 15589-15598.
7. W. Cheng, J. Wang, U. Jonas, G. Fytas and N. Stefanou, Nat. Mater., 2006, 5, 830-836.
8. T. Still, W. Cheng, M. Retsch, R. Sainidou, J. Wang, U. Jonas, N. Stefanou and G. Fytas, Phys. Rev. Lett., 2008, 100.
9. K. Chen, T. Still, S. Schoenholz, K. B. Aptowicz, M. Schindler, A. C. Maggs, A. J. Liu and A. G. Yodh, Phys. Rev. E, 2013, 88, 022315.
10. S.-M. Yang, S. G. Jang, D.-G. Choi, S. Kim and H. K. Yu, Small, 2006, 2, 458-475.
11. C. Stelling, A. Mark, G. Papastavrou and M. Retsch, Nanoscale, 2016, 8, 14556-14564.
12. M. Retsch and U. Jonas, Adv. Funct. Mater., 2013, 23, 5381-5389.
13. F. A. Nutz, P. Ruckdeschel and M. Retsch, J. Colloid. Interf. Sci., 2015, 457, 96-101.

14. P. Ruckdeschel, T. W. Kemnitzer, F. A. Nutz, J. Senker and M. Retsch, Nanoscale, 2015, 7, 10059-10070.
15. P. A. Steward, J. Hearn and M. C. Wilkinson, Adv. Colloid. Interf. Sci., 2000, 86, 195-267.
16. M. A. Winnik, Curr. Op. in. Colloid. In., 1997, 2, 192-199.
17. J. L. Keddie, Mat. Sci. Eng. R., 1997, 21, 101-170.
18. E. Gonzalez, M. Paulis, M. J. Barandiaran and J. L. Keddie, Langmuir, 2013, 29, 2044-2053.
19. R. E. Dillon, L. A. Matheson and E. B. Bradford, J. Colloid Sci., 1951, 6, 108-117.
20. P. Lepoutre and B. Alince, J. Appl. Polym. Sci., 1981, 26, 791-798.
21. X. Chen, S. Fischer, Z. Yi, V. Boyko, A. Terrenoire, F. Reinhold, J. Rieger, X. Li and Y. Men, Langmuir, 2011, 27, 8458-8463.
22. A. F. Routh and W. B. Russel, Langmuir, 1999, 15, 7762-7773.
23. A. F. Routh and W. B. Russel, Ind. Eng. Chem. Res., 2001, 40, 4302-4308.
24. D. P. Jensen and L. W. Morgan, J. Appl. Polym. Sci., 1991, 42, 2845-2849.
25. K. Hahn, G. Ley, H. Schuller and R. Oberthur, Colloid. Polym. Sci., 1986, 264, 1092-1096.
26. J. E. Anderson and J. H. Jou, Macromolecules, 1987, 20, 1544-1549.
27. J. N. Yoo, L. H. Sperling, C. J. Glinka and A. Klein, Macromolecules, 1990, 23, 3962-3967.
28. K. D. Kim, L. H. Sperling, A. Klein and B. Hammouda, Macromolecules, 1994, 27, 6841-6850.
29. K. Hahn, G. Ley and R. Oberthur, Colloid. Polym. Sci., 1988, 266, 631-639.
30. Q. Nawaz and Y. Rharbi, Langmuir, 2010, 26, 1226-1231.
31. Y. Rharbi, F. Boué and Q. Nawaz, Macromolecules, 2013, 46, 7812-7817.
32. O. Pekcan, M. A. Winnik and M. D. Croucher, Macromolecules, 1990, 23, 2673-2678.
33. Y. C. Wang, C. L. Zhao and M. A. Winnik, J. Chem. Phys., 1991, 95, 2143-2153.

34. Y. C. Wang and M. A. Winnik, J. Phys. Chem., 1993, 97, 2507-2515.
35. E. M. Boczar, B. C. Dionne, Z. W. Fu, A. B. Kirk, P. M. Lesko and A. D. Koller, Macromolecules, 1993, 26, 5772-5781.
36. Y. S. Liu, J. R. Feng and M. A. Winnik, J. Chem. Phys., 1994, 101, 9096-9103.
37. W. L. Vos, M. Megens, C. M. vanKats and P. Bosecke, Langmuir, 1997, 13, 6004-6008.
38. N. Dingenouts and M. Ballauff, Langmuir, 1999, 15, 3283-3288.
39. S. Hu, J. Rieger, Z. Yi, J. Zhang, X. Chen, S. V. Roth, R. Gehrke and Y. Men, Langmuir, 2010, 26, 13216-13220.
40. E. A. Sulyanova, A. Shabalin, A. V. Zozulya, J. M. Meijer, D. Dzhigaev, O. Gorobtsov, R. P. Kurta, S. Lazarev, U. Lorenz, A. Singer, O. Yefanov, I. Zaluzhnyy, I. Besedin, M. Sprung, A. V. Petukhov and I. A. Vartanyants, Langmuir, 2015, 31, 5274-5283.
41. A. Georgiadis, P. A. Bryant, M. Murray, P. Beharrell and J. L. Keddie, Langmuir, 2011, 27, 2176-2180.
42. X. Qu, Y. Shi, Y. Tang, L. Chen and X. Jin, J. Colloid. Interf. Sci., 2002, 250, 484-491.
43. J. Rottstegge, B. Traub, M. Wilhelm, K. Landfester, C. Heldmann and H. W. Spiess, Macromol. Chem. Phys., 2003, 204, 787-802.
44. R. H. Ottewill and J. N. Shaw, Kolloid Z. Z. Polym., 1967, 215, 161-166.
45. T. Still, M. Retsch, U. Jonas, R. Sainidou, P. Rembert, K. Mpoukouvalas and G. Fytas, Macromolecules, 2010, 43, 3422-3428.

Supporting Information

Interfacial- and Volumetric Sensitivity of the Dry Sintering Process of Polymer Colloidal Crystals: A Thermal Transport and Photonic Bandgap Study

Fabian A. Nutz and Markus Retsch*

Stages of latex film formation

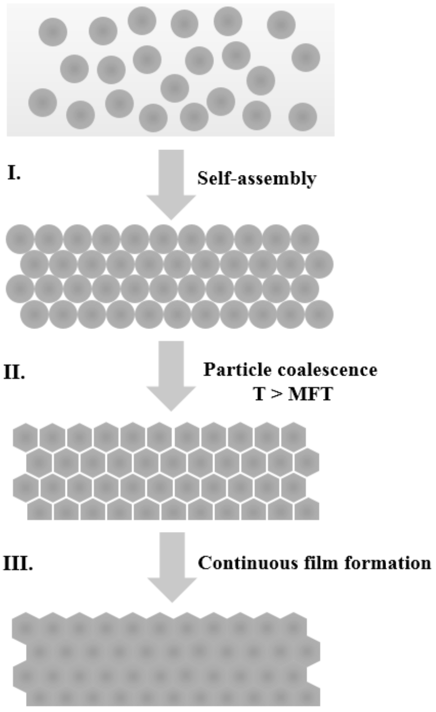

Figure S1: Schematic view on the three stages of the colloidal film formation process. (I.) Self-assembly of the particles; (II.) particle coalescence by exceeding the particles minimum film formation temperature (MFT); (III.) continuous film formation due to interpenetration of the polymer chains across the particle-particle interfaces.

Details on laser flash analysis

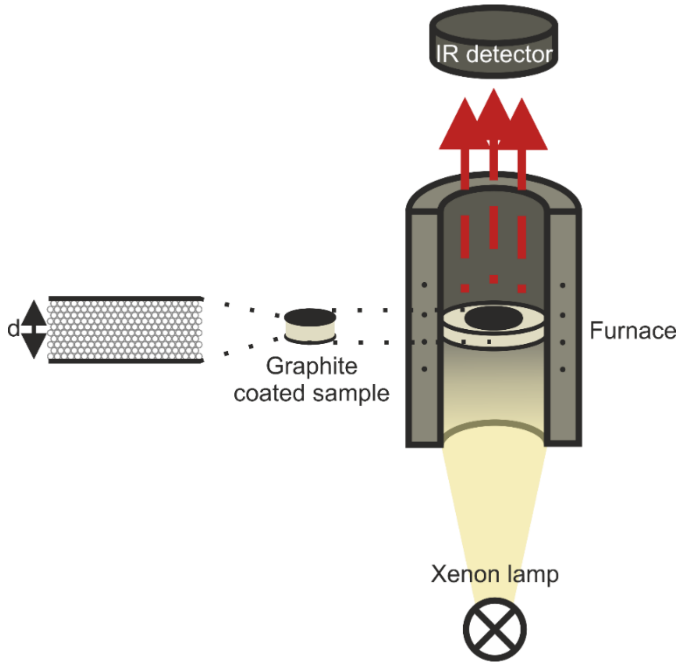

Figure S2: Schematic setup of a Laser flash apparatus.

Measurements were carried out under helium atmosphere to enable a good heat transfer from the oven to the sample. Before the measurement, the top and bottom of the samples were metalized with a 100-200 nm gold or silver layer, which serves as blocking layer for the light pulse. Additionally, both sides were coated with a thin layer of graphite (<20 µm), to ensure a high absorbance of the light pulse at the bottom side and a high IR emission at the top side. The generated heat of the light pulse at the bottom side is transported through the sample and emitted as IR radiation at the top side of the sample. The intensity of the IR signal is then recorded in dependence of time. The raw data is fitted using a radiation fit model provided from Linseis. From laser flash analysis, the sample's thermal diffusivity α is calculated according to equation 1.

$$\alpha = \frac{1.38 \cdot d^2}{t_{1/2}} \tag{1}$$

where d represents the thickness of the sample and $t_{1/2}$ is the time needed to reach half of the maximum temperature rise. The thermal conductivity κ can then be calculated as follows:

$$\kappa(T) = \alpha(T) \cdot c_p(T) \cdot \rho(T) \tag{2}$$

C_p is the specific heat capacity of the sample, which is determined by DSC. ϱ representing the density of the sample. The density of the colloidal crystals and the molten colloidal films is determined by 3D macroscopy and a buoyancy balance, respectively.

The thickness and the density of the crystal will undergo significant changes during film formation (thickness decreases, density increases). However, it is not possible to follow these changes during the laser flash experiment in-situ. Therefore, a step-function behavior was assumed at T_g for the thickness and the density of the crystal by determining both quantities before and after the laser flash experiment.

For time-dependent laser flash analysis the changes in sample thickness have to be considered more precisely. Since it is not possible to follow the decrease in thickness during laser flash analysis *in-situ*, we determined the time-dependent behaviour of the sample thickness at 70, 75, and 80 °C separately (Figure S3A). The crystal thickness was found to follow a single-exponential function. By measuring the sample thickness before and after the experiment it is possible to incorporate this behaviour into the calculations of α according to equation 1 assuming the same exponential behaviour between the measurable initial and final sample thickness within the laser flash experiment.

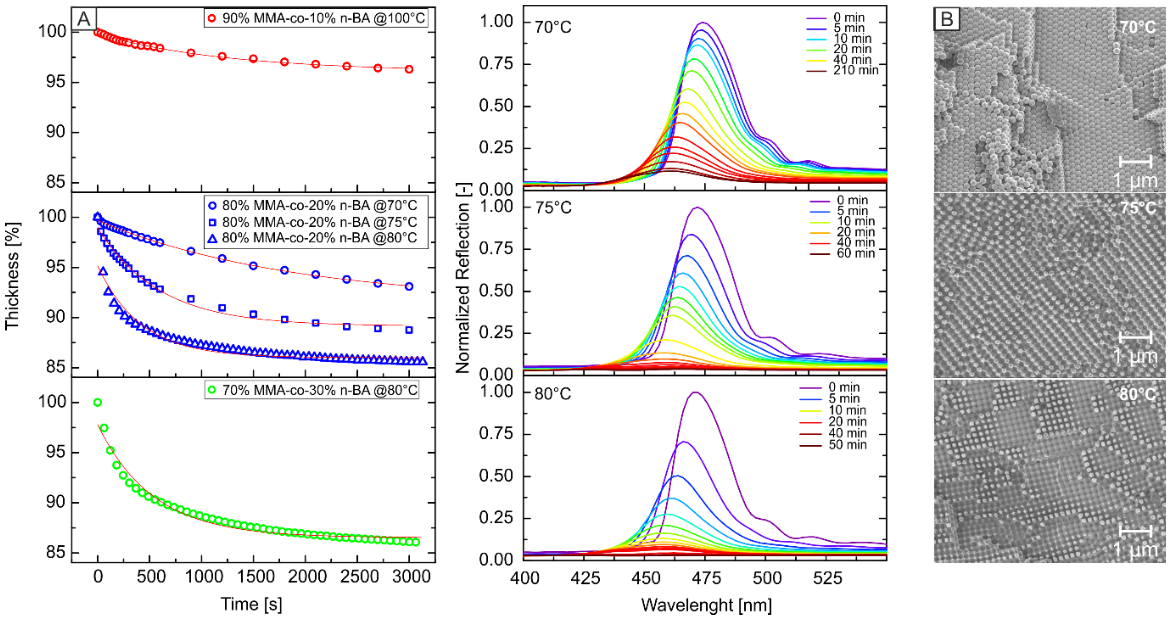

Figure S3: a) Time-dependent decay of the thickness of different colloidal crystals: the thickness reduction can be described by an exponential decay. b) SEM side-view micrographs of 80% MMA-co-20% nBA colloidal crystals annealed for 50 min at the denoted temperature.

The crystal thickness behaves similarly for every temperature under investigation. The thickness decreases faster with increasing temperature due to a higher mobility of the polymer chains at higher temperatures. This leads to a faster softening of the particles, resulting in a faster loss of porosity and thus, to a faster decrease in height of the crystal.

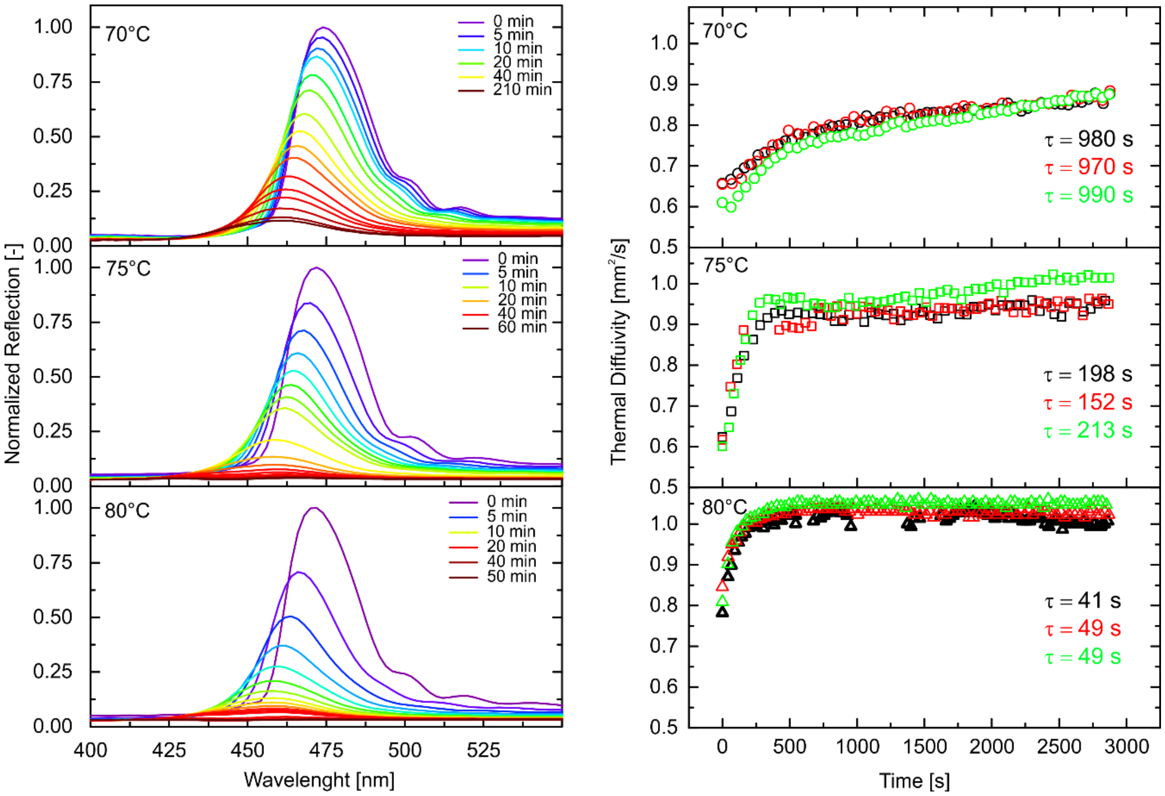

Figure S4: left) Time-dependent UV-Vis of an 80% MMA-co- 20%-nBA colloidal crystal at 70, 75 and 80 °C, respectively. right) Time-dependent laser flash analysis of three individual samples at the specified temperatures.

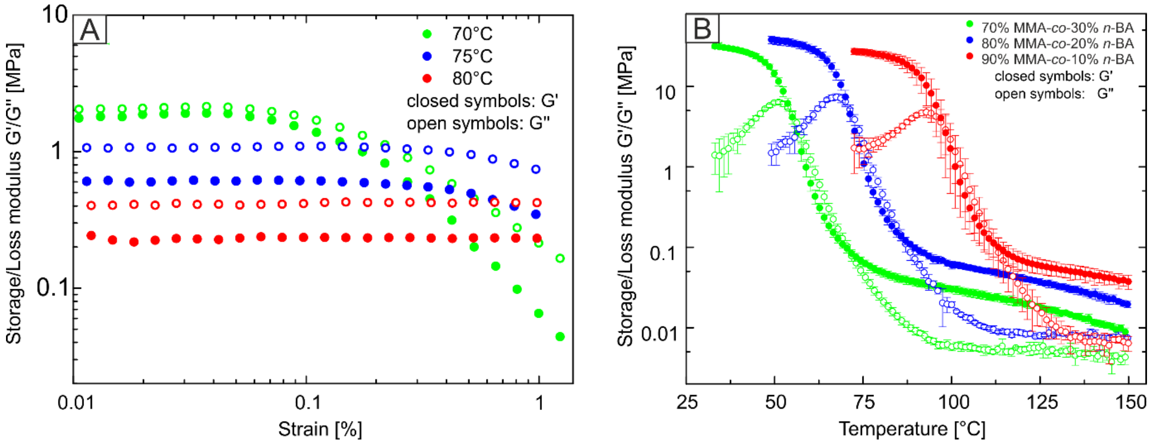

Figure S5: a) strain sweep for 80% MMA-co- 20%-nBA polymer at 70, 75 and 80 °C to determine the viscoelastic regime. b) Temperature-dependent storage/loss modulus of the three different polymers.

4.3 Tailor-Made Temperature-Dependent Thermal Conductivity: The Power of Interparticle Constriction

Fabian A. Nutz and Markus Retsch

University of Bayreuth, Physical Chemistry – Polymer Systems, Universitaetsstr. 30, 95447 Bayreuth, Germany.

Table of Content Figure

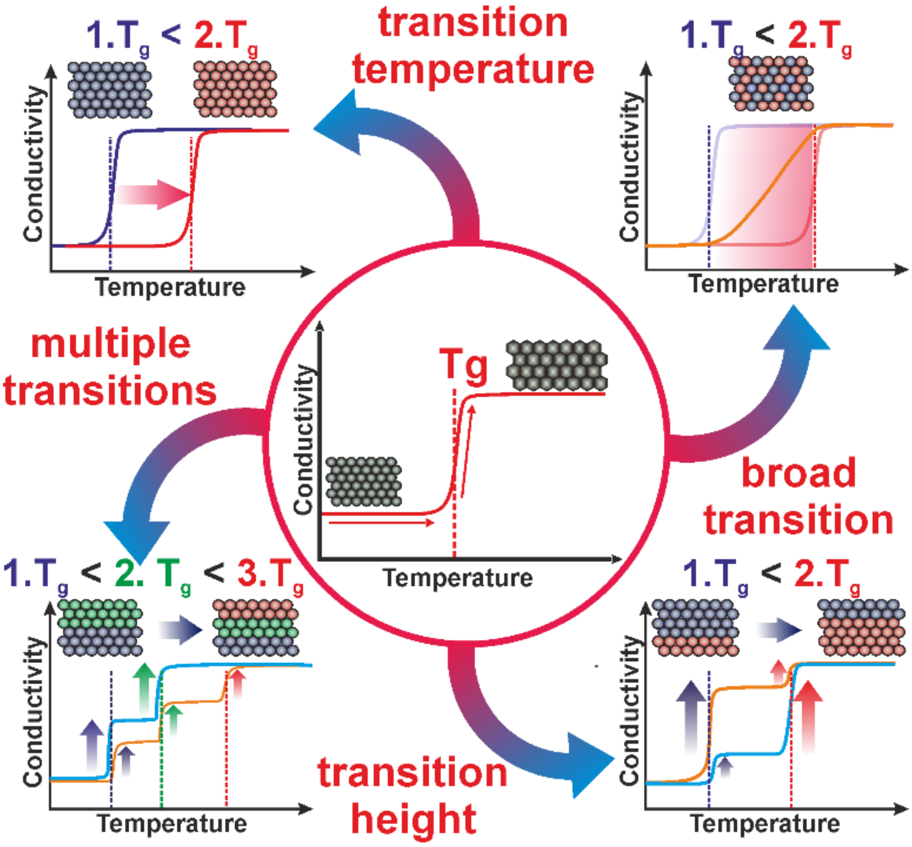

Abstract

Managing heat is a major challenge to meet future demands for a sustainable use of our energy resources. This requires materials, which can be custom-designed to exhibit specific temperature-dependent thermal transport properties to become integrated into thermal switches, transistors, or diodes. Common crystalline and amorphous materials are not suitable, owing to their gradual changes of the temperature dependent thermal conductivity. Here we show how a second-order phase transition fully controls the temperature-dependent thermal transport properties of polymer materials. We demonstrate four major concepts based on a colloidal superstructure: 1) control of transition temperature, 2) width of phase transition regime, 3) multistep transitions, and 4) step height of the transition. Most importantly, this unique control over the thermal conductivity is only governed by the interparticle constriction, the particle composition, and its mesostructure. Our concept is therefore also applicable to a wide variety of other particulate materials.

Introduction

With increasing energy consumption and further miniaturization of electronic devices a need for new, space-saving and functional materials to manage heat arises. Recent examples report on the theory and realization of thermal memory,(1-3) thermal rectification,(4-6) dynamic insulation,(7, 8) phase change materials,(9) thermal cloaking(10) and thermal switching materials.(11) The experimental realization of many of these emerging applications is still a great challenge. One major limiting factor is given by the typical power-law temperature dependence of the thermal conductivity of most materials. For crystalline materials one usually finds a power-law exponent of +3 up to the Debye temperature and a -1 to -3 exponent at higher temperatures.(12) Amorphous materials merely exhibit a monotonic increase across the entire temperature range, combined with commonly one or two plateau regimes.(13) To pave the way towards advanced heat management devices and thermal logic circuits, tailor-made materials with non-power-law but well-controlled temperature dependent properties are needed. E.g. for thermal diodes, non-linearity is required,(12) whereas abrupt changes with a small input of excess heat is necessary for the gate material of thermal transistors.(14) State-of-the-art materials utilize a first-order phase transition either in their homogeneous bulk form(9, 14-17) or in a heterogeneous blend(18-21) to manipulate the temperature dependent thermal transport. In homogeneous bulk materials, the thermal properties are governed by the material composition, rendering it difficult to target a specific application. Composite materials provide a higher degree of flexibility, owing to the selection of certain material combinations.

Quite importantly, the temperature-dependent properties of a material can additionally be strongly influenced by the underlying micro- and nanostructure.(22, 23) A premier example are colloidal crystals, which have received much attention, predominantly within the field of photonics,(24-27) phononics,(25, 28, 29) or as template structures.(30-32) Highly-defined colloidal superstructures are accessible in a simple and scalable way by established fabrication methods.(30-32) Surprisingly, colloidal crystals represent a strongly underexplored field with respect to their thermal transport properties. When going through the second-order phase transition, namely the glass transition temperature of the constituting polymer, the increase in polymer mobility leads to a loss of the particulate nanostructure. Consequently, the thermal conductivity increases sharply.(33) The versatile structural fabrication can be complemented by specific particle design to add further functionality to the colloidal ensemble. This allows to widely program the thermal transport properties to a specific need.

In this work, we demonstrate the vast potential of constriction controlled thermal transport through particulate ensembles. We choose polymer colloidal crystals as a case study to specifically tune the temperature-dependent thermal conductivity.

We emphasize that this tuning is solely based on the geometric constriction. Precisely, the thermal conductivity is governed by the thermally induced changes of the nanosized interparticle contact area between adjacent particles in a close-packed colloidal superstructure. Figure 1 outlines the unique possibilities provided by constriction controlled thermal transport.

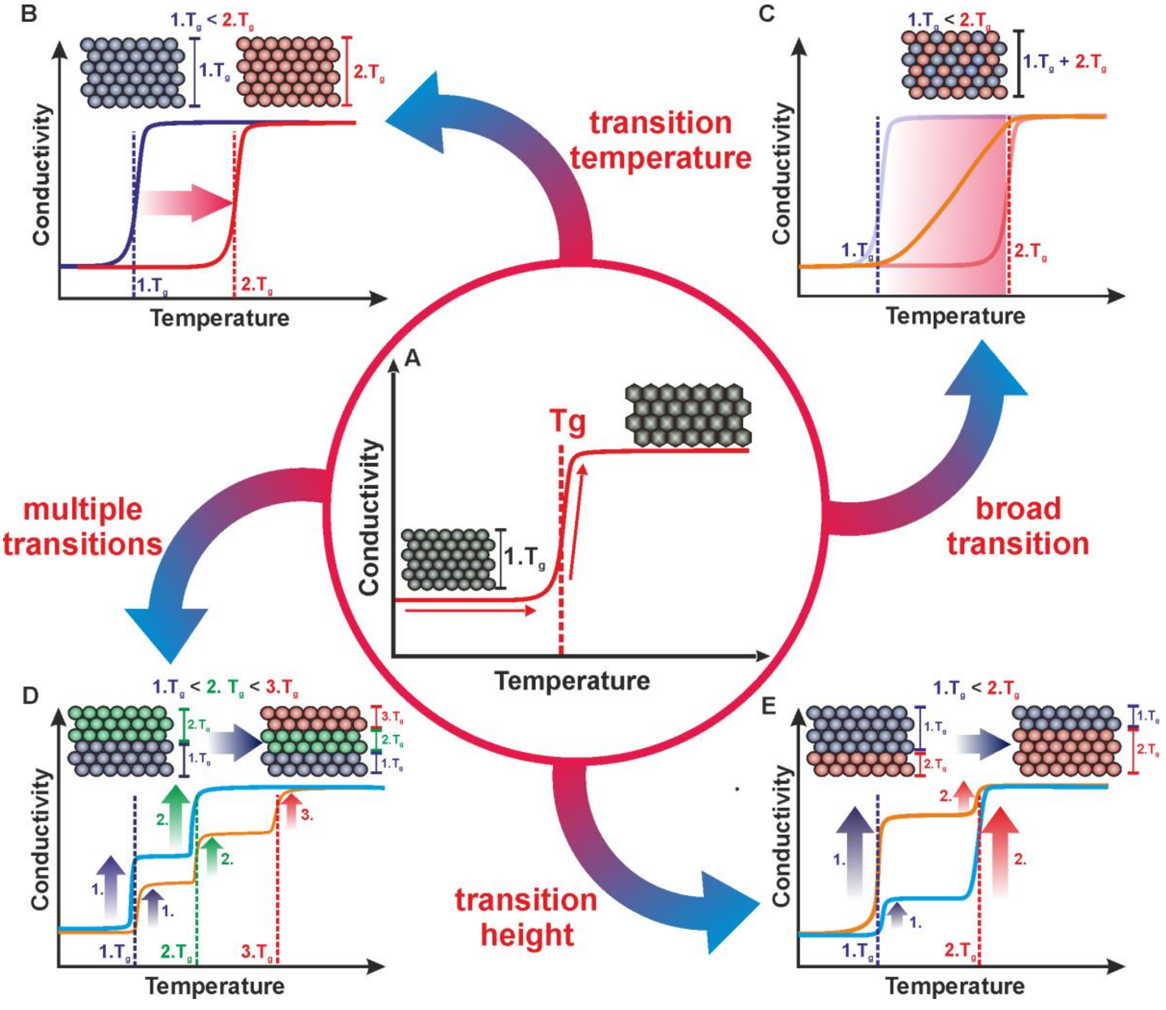

Figure 1: Key aspects for heat management devices and their realization based on constriction controlled thermal transport in colloidal assembly structures. (A) By exceeding T_g, the thermal conductivity irreversibly increases based on the enlargements of contact points during particle sintering. (B) The transition temperature can be tailored by assembling the crystal from particles possessing different T_g. (C) The random co assembly of equal sized particles but different T_g results in a broad transition. (D) Multiple transition steps can be introduced by a discrete layer-by-layer assembly. (E) The height of the transition steps is controllable by the thickness of the respective layer.

We demonstrate four key aspects, which are of paramount importance for future heat management devices, and become accessible for the first time via our concept:

1) Figure 1b: adjustment of the (second-order) phase transition to a desired temperature. 2) Figure 1c: tuning of the phase transition range. 3) Figure 1d: introduction of multiple discrete transition steps. 4) Figure 1e: controlling the degree of transition change.

We show how to program the described transition behavior of these assemblies by adjusting the thermal properties of the polymer particles and by selecting a suitable mesoscopic colloidal crystal architecture. Our system is based on copolymer particles consisting of n-butyl methacrylate (n-BA) and methyl methacrylate (MMA). By adjusting the n-BA content of the particles, it is possible to control the glass transition temperature of the copolymer.(26)

Results

Adjustment of the phase transition to the desired temperature

We start by tailoring the onset transition temperature of the thermally inducible increase of the thermal conductivity. Therefore, highly monodisperse n-BA-co-MMA particles possessing different glass transition temperatures and a nearly equal diameter (182 and 223 nm, Table S1, Set 1) were synthesized. The particle self-assembly typically yields free-stranding disk shaped monoliths with a diameter of ~20 mm and a thickness of several hundred micrometers. Optical and scanning electron microscopy (SEM) images of the split edges of such monoliths are shown in Figure 2a.

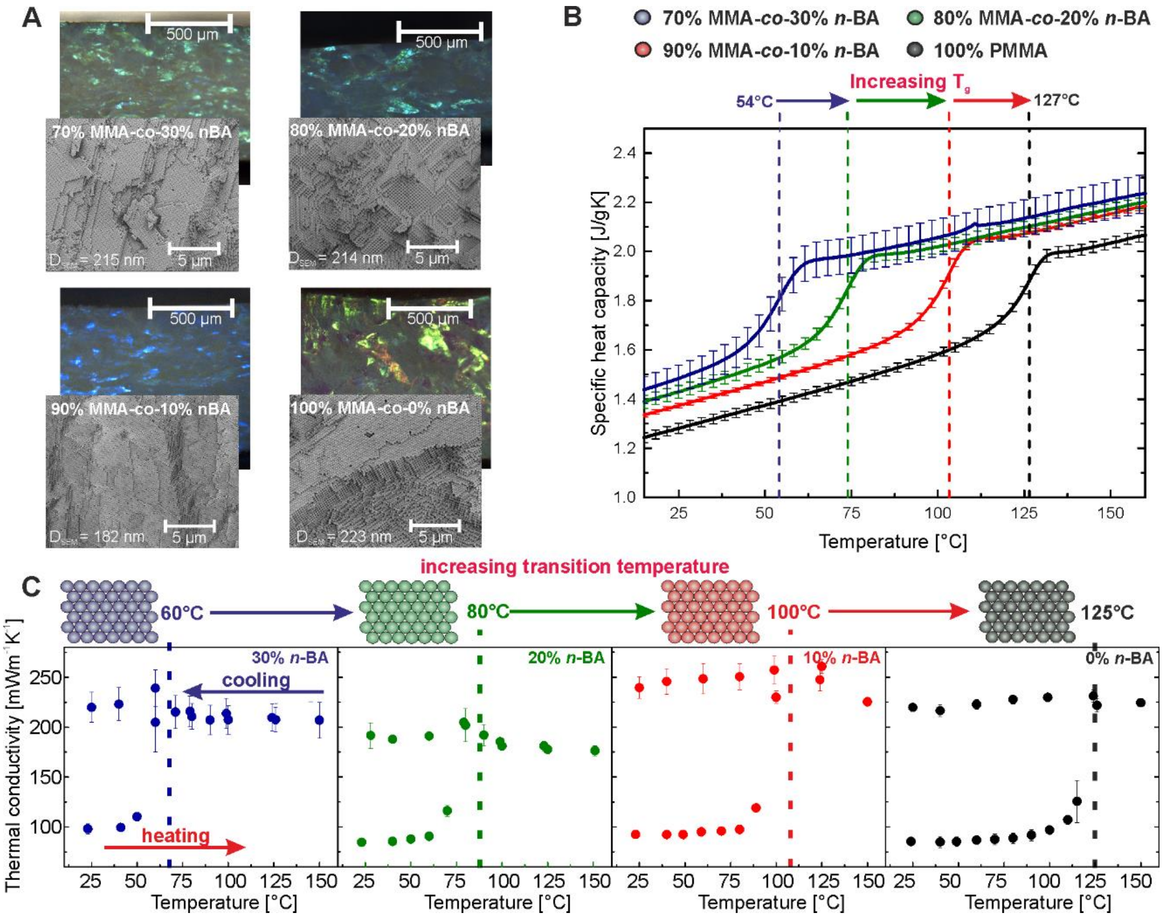

Figure 2: Thermal conductivity of polymer colloidal crystals possessing different T_g. (a) Optical and scanning electron microscopy images of the split edges of the assembled crystals. The strong opalescence indicates a long range crystalline order within the free-standing monoliths. The high crystallinity is confirmed by SEM images, (b) Specific heat capacity of the synthesized copolymer particles. With increasing MMA content, the T_g of the polymer is shifted to higher temperatures. (c) Temperature dependent thermal conductivity of polymer colloidal crystals from particles possessing different T_g (heating and cooling cycle). By adjusting the copolymer composition, it is possible to tailor the transition temperature systematically. Error bars represent the standard deviation derived from three individual measurements.

A strong opalescence is visible throughout the entire monoliths based on Bragg reflection. This indicates a highly crystalline order of the particles within the specimen. Different reflectivity colors within a monolith arise from various crystal planes exposed to the surface. The slightly varying colors between the different monoliths are based on the size dependency of the Bragg reflection. SEM images confirm the optical microscopy impression. The polymer particles arrange into a well-defined, close-packed *fcc* symmetry. Overall, the samples can be regarded as fully crystalline.

Figure 2b shows the temperature dependent heat capacity of the synthesized copolymers with a varying MMA content of 70, 80, 90 and 100 %. The absolute heat capacity increases with increasing n BA content. The systematic shift of the glass transition from 54 °C (70 vol% MMA) to 127 °C (100 % MMA) further proves the successful random copolymerization. In general, copolymers possessing a glass transition temperature between the Tg of pure poly(n BA) (-49 °C) and pure poly(MMA) (125 °C) would accessible via the random copolymerization of the two monomers. This leaves ample degrees of freedom to tailor the temperature response towards specific needs in a broad ambient temperature range.

The thermal conductivity data are summarized in Figure 2c. All samples show a sharp step like increase of the thermal conductivity near the glass transition temperature of the corresponding polymer. At this point, the interparticle contact points enlarge and the porosity within the sample vanishes, resulting in a strongly increased thermal conductivity. The kinetics of this transition have been examined elsewhere.(34) In all cases, a sharp increase in thermal conductivity by at least 200 % could be programmed to a specific temperature, simply by controlling the second-order phase transition of the constituting polymer.

Tuning of the phase transition range

For a seamless adjustment of the thermal conductivity between the pristine (< 100 $\mathrm{mWm^{-1}K^{-1}}$) and the sintered state (> 200 $\mathrm{mWm^{-1}K^{-1}}$) a random co-assembly of two particle types with comparable size can be used (Figure 3a).

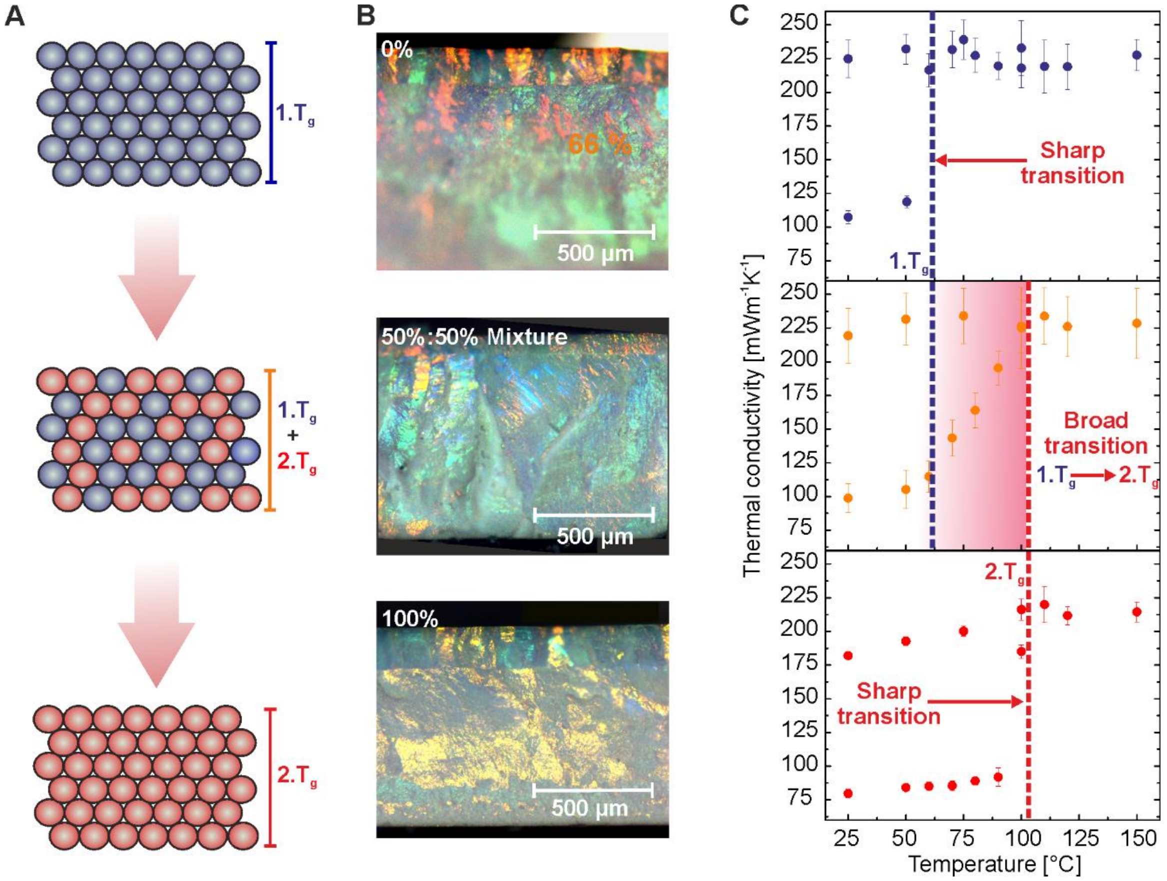

Figure 3: Temperature dependent thermal conductivity of co-assembled polymer colloidal assemblies. (A) Schematic illustration of the composition of a co-ssembled colloidal crystal. The co-assembly leads to structurally homogeneous colloidal crystals due to the comparable particle size. (B) Optical micrographs of the split edges of pure colloidal crystals (Mixing ratios: 0 % and 100 % of T_g = 103 °C particles) in comparison to a co assembled binary crystal (Mixing ratio: 50 %:50 %). (C) Temperature dependent thermal conductivity of the 50 %:50 % colloidal crystal compared to its pure counterparts. The binary colloidal crystal shows a broad transition ranging between the glass transition temperatures (dashed lines) of the pure copolymer particles. Error bars represent the standard deviation derived from three individual measurements. Thermal diffusivity data can be found in Figure S3a.

We demonstrate this capability with a $T_{g,2}$ = 103 °C and $T_{g,1}$ = 61 °C particle with 403 nm and 434 nm diameter, respectively. The indicated particle ratios represent number mixing ratios of the binary particle dispersions. Number and volume ratios can be treated equivalently here, due to the comparable particle size and density. Due to the almost equal size of the particles, the overall crystallinity of the colloidal ensemble is preserved. This can be inferred from the bright opalescent colors in the side-view optical micrographs (Figure 3b).

The initial and final temperature of the transition can be freely chosen based on the T_g of the constituting particles. Whereas the crystals made from only one particle type (Figure 3c blue/red) show the familiar sharp increase in thermal conductivity, the co-assembled colloidal crystal shows a broad, linear increase from the lower to the higher T_g (Figure 3c, orange circles). This trend is also readily confirmed in the thermal diffusivity data (Figure S3). It is therefore inherent to thermal transport changes within the colloidal crystal and does not originate from variations in the density or specific heat capacity used to calculate the thermal conductivity (DSC Data are given in Figure S1). We ascribe this broad transition to the following reason. By exceeding the first T_g, the lower melting particles deform and thereby increase the contact area to the surrounding higher melting particles. Also, clusters and probably percolating trusses of the lower melting component may form at this stage. Still, a skeleton of higher melting particles partially retain the structure and prevents a sharp increase of the thermal conductivity. By further increasing the temperature, the lower melting particles become softer, and the polymer chains become more mobile. This can lead to a further increase of the interparticle contact area and progressively results in a dense film formation. Additionally, the softening of the higher melting particles starts to take place. Ultimately, by exceeding the glass transition temperature of the higher melting particle, the remaining structure vanishes completely, and the bulk thermal conductivity of the polymer film (~ 200 $mWm^{-1}K^{-1)}$ is obtained. Thus, a continuous adjustment of the thermal conductivity is possible via a simple binary colloidal crystal and the gradual loss of the constricting interparticle contact points. Noteworthy, we also prepared binary colloidal crystals with various mixing ratios (Figure S4). These, however, retain a sharp transition feature at the T_g of the majority component. This hints towards the importance of cluster and percolation formation, which we observed for the 50 % : 50 % mixture.

Introduction of multiple discrete transition steps

To program distinct steps into the temperature-dependent thermal conductivity, we fabricated more intricate colloidal superstructures. Therefore, we employed filtration, which easily allows fabricating layered colloidal ensembles. Filtration represents a much faster self-assembly method compared to the evaporation induced self-assembly. This, however, comes at the expense of the long-range crystalline order (Figure S5a). Nevertheless, filtration provides direct access to tailor-made colloidal superstructures in a layer-by-layer fashion. Thus, we fabricated multi layered, free-standing colloidal monoliths in which every layer consisted of particles with a pre-defined T_g. We demonstrate the thermal transport properties of three particles of ~ 500 nm diameter with $T_{g,1} = 61$ °C, $T_{g,2} = 103$ °C, and $T_{g,3} = 124$ °C. This introduces multiple transition steps of the thermal conductivity by a discrete sintering of the individual layers at the respective T_g. The schematic structure for such monoliths is illustrated in Figure 4a.

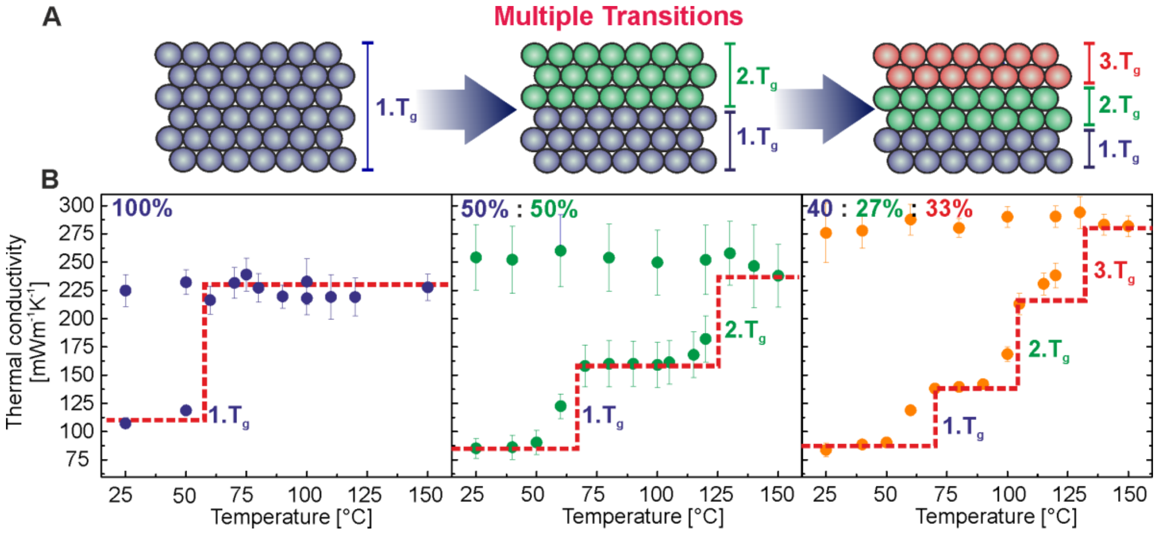

Figure 4: Introduction of multiple step transitions. (A) Schematic illustration of the structure of a colloidal monolith consisting of one, two and three particles layers where each layer possesses a different T_g (blue, green and red). (B) Temperature dependent thermal conductivity of colloidal monoliths consisting of one, two and three particle layers. Based on the discrete layer assembly, multiple step like increases (dashed red lines) at the specific T_g of the copolymer particle are observed. Error bars represent the standard deviation derived from three individual measurements. Thermal diffusivity data can be found in FigureS3a and b.

The temperature dependent thermal conductivity of colloidal assemblies consisting of one, two and three particle layers are illustrated in Figure 4b. In contrast to the randomly mixed binary colloidal crystal discussed above (Figure 3), the discrete layer assembly evokes distinct steps in the thermal conductivity profile. This is based on the sintering of the homogenous, individual layer at its corresponding T_g. The unmolten layers remain in their pristine state. Exceeding the T_g of the remaining layers results in a further, multistep increase of the effective thermal conductivity of the entire ensemble. Conceptually, an arbitrary number of distinct steps could be introduced in this fashion to a particulate material. We demonstrate a three-step material by layering three particle types. The respective transition temperatures coincide with the pre-determined T_g (Figure 4b, orange).

Controlling the degree of transition change

Finally, it is also important to control how much the thermal conductivity will change upon crossing a specific temperature. Building upon our experience of the multilayered structure introduced above, we conceived a suitable colloidal architecture. This is achieved by adjusting the layer thickness of the assembly. The structure of such assemblies is schematically sketched in Figure 5a. Our sample consists of two particles ($T_{g,1} = 61$ °C and $T_{g,2} = 124$ °C).

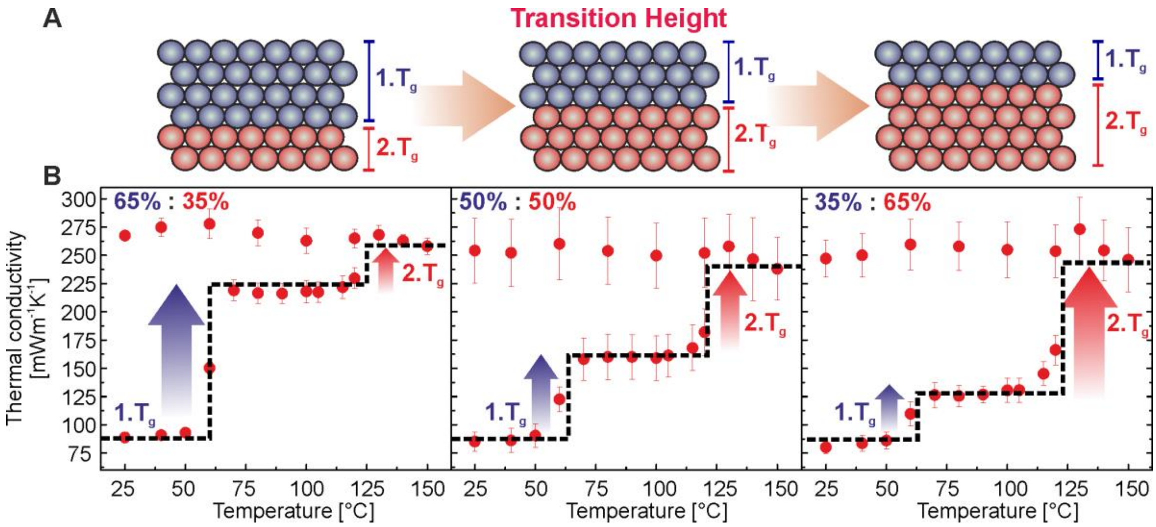

Figure 5: Tuning the transition height. (A) Schematic illustration of the structure of a colloidal monolith with varying layer thickness. The thickness of the red particle layer increase from left to right. (B) Temperature dependent thermal conductivity of different colloidal assemblies with varying particle layer thickness. The thickness of the higher melting layer is increased from left to right, leading to an increasing transition height at the second T_g (red arrow). Error bars represent the standard deviation derived from three individual measurements. Thermal diffusivity data can be found in Figure S3d and e.

Based on the amount of particle dispersion used in the filtration process, it is readily possible to adjust the thicknesses of the different layers within the final assembly. Figure 5b shows the temperature dependent thermal conductivity of three different colloidal assemblies with varying thickness ratios between both particle layers. The layer thickness of the higher melting particle layer increases from left to right.

Whereas a strong increase of the thermal conductivity at the lower glass transition temperature (Figure 5b, left, blue arrow) is visible for monoliths containing only a thin layer of high T_g particles, this behavior reverses for assemblies containing a thick layer of high T_g particles (Figure 5b, right, red arrow). Consequently, this concept allows for a precise adjustment of the target thermal conductivity after exceeding a specific temperature – simply by controlling the relative amount of material changing from the insulating to a more conducting state. Furthermore, this could also be extended to three or more layers.

Finally, we want to demonstrate that the four fundamental concepts outlined so far can be combined with each other. This gives even more degrees of freedom to design any specific temperature-dependent thermal conductivity profile. We therefore, chose a two-layer assembly, combining evaporation induced self-assembly of a random mixture with the filtration aided buildup of a layered structure. A schematic sketch of the intended colloidal architecture is shown in Figure 6, as well as the temperature dependent thermal conductivity of such an assembly. Optical microscopy images of this structure are shown in Figure S5b.

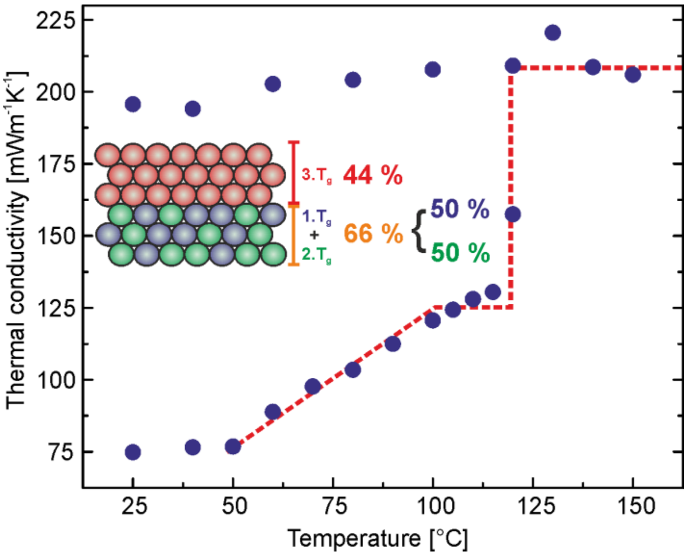

Figure 6: Combining a broad and a step like transition. Temperature dependent thermal conductivity of a two layer colloidal assembly. Whereas the bottom layer is fabricated by evaporation induced self-assembly of two particles possessing different T_g (90 vol%-MMA 2; T_g = 103°C, 70 vol%-MMA 2; T_g = 61 °C), the upper layer consists of only on particle type (100 vol%-MMA 1; T_g = 127 °C). Thermal diffusivity data can be found in Figure S3f.

The bottom layer consists of a crystalline co assembly of two equally sized particles with $T_{g,1}$ = 103 °C and $T_{g,2}$ = 61 °C (equal to the assembly shown in Figure 3c). The top layer comprises only one particle type $T_{g,3}$ = 127 °C and is not crystalline, due to the faster filtration self-assembly process. With this architecture, it is possible to tailor the thermal conductivity to show a broad transition between 60 °C and 100 °C, analogous to Figure 3, and a sharp, step like increase of the thermal conductivity at ~125 °C, similar to Figure 2. The respective step heights are governed by the relative layer thicknesses of the two components.

Discussion

These four concepts show that colloidal assembly structures can control the temperature dependent thermal transport properties with an unprecedented degree of flexibility. This capability becomes even more relevant, since the fabrication method is scalable and can be flexibly adapted to other materials, too. This allows introducing even further functional properties. Furthermore, the constriction controlled thermal transition represents a purely solid state transition, with no liquids involved. Whereas the polymer platform presented here is not allowing for a reversible adjustment of the thermal properties, we are convinced that this concept can be expanded to other material systems, too. These may then provide the required reversibility for future applications. Our findings outline a general approach to specifically tailor the temperature dependent thermal conductivity of a nanostructured material. We want to stress the high relevance of the interparticle contact points, which is the first ingredient to allow for this impressive degree of flexibility. The ability to adjust the onset of the glass transition temperature of the polymer particles by simple chemical synthesis is the second key ingredient. Combining these two parameters in tailor-made colloidal superstructure allowed us to show four key properties, which will be of relevance for future heat management device: 1) adjustable onset temperature, 2) width of transition, 3) multi-step transitions, and 4) height of transition steps. Yet, one also has to consider the current short coming of this simple material composition, namely the irreversibility of changes to the interparticle contact area. Nevertheless, we are convinced that this contribution will motivate more research on the thermal transport through particulate structures. This may very likely lead to the availability of more functional particle compositions, which may circumvent the irreversibility of the polymer particle sintering. Furthermore, these may allow for the introduction of other external stimuli such as pH, solvents, light, electric currents or electric fields to trigger the necessary transition. Considering the inherent and well-known photonic and phononic properties of colloidal crystals and glasses adds even another dimension of functionality, which we did not elaborate on in this contribution. Thus, this concept paves the way towards a genuinely multiphysical and multifunctional heat-management material.

Materials and Methods

Methyl methacrylate (MMA, 99 %, Aldrich) and n-Butyl acrylate (nBA; ≥ 99 %, Aldrich) were purified by filtration over an alumina column (activated, basic, Brockmann I, Sigma Aldrich). Potassium peroxodisulfate (KPS, ≤ 99 %, Sigma Aldrich), 4-styrenesulfonic acid sodium salt hydrate (NaSS, 99%, Aldrich) and acrylic acid (AA, 99 %, Sigma Aldrich) were used as received. Ultrapure water was taken from a Millipore Direct Q3UV unit and was used throughout the entire synthesis.

Particle synthesis. Polymer particles were synthesized by emulsifier free emulsion polymerization.(35, 36) In a typical synthesis 50 mL of the monomer mixture (e.g. 40 mL MMA/ 10 mL nBA for 20 vol% nBA particles) and 450 ml ultrapure water were charged in a 3 necked flask, heated to 75 °C and equilibrated for 15 minutes under a slight argon flow. Subsequently, 2 ml of acrylic acid were added to the mixture followed by a further equilibration step of 5 min. The polymerization was initiated by adding 150 mg KPS, dissolved in 5 ml ultrapure water. The reaction was carried out overnight. For purification, the particles dispersion was dialyzed against ultrapure water for five days, changing water twice a day. The diameters and glass transition temperatures of the synthesized particles are summarized in Table S1. Almost equal-sized particles with varying n BA content have been synthesized (Set 1: ~220 nm and Set 2: ~500 nm).

Crystal assembly. The colloidal crystals were fabricated by evaporations induced self-assembly, by filtration, or by a combination of both techniques. Evaporation induced self-assembly of a given amount of particle dispersion yields disk shaped, highly crystalline colloidal monoliths of a diameter of ~20 mm. Particle assembly by filtration was carried out to fabricate multi-layered, colloidal monoliths by sequential filtration of different particle dispersions. After the filtration of the last layer, the specimens were allowed to dry overnight under ambient conditions.

Dynamic light scattering: Dynamic light scattering was performed on diluted particle dispersions a Malvern Zetasizer with 175° backscattering geometry to obtain the hydrodynamic diameter and the size distribution of the synthesized particles.

Light microscopy: The edges of split colloidal crystals were investigated on a Carl Zeiss Axio Imager.A2m bright field light microscope equipped with an AxioCam Icc 1 camera to study the macroscopic order within the fabricated colloidal monoliths.

Scanning electron microscopy: Scanning electron microscopy (SEM) was performed on a Zeiss Leo 1530 electron microscope to obtain the hard sphere diameter of the particles. Furthermore, SEM images along the edges of split colloidal crystals were obtained to get an idea of the particle ordering within the interior of the monoliths.

Laser flash analysis: Laser flash analysis was conducted on a Linseis XFA 500 XenonFlash apparatus equipped with an InSb infrared detector. The sample surfaces were coated with a thin layer of graphite (<15 μm) on the bottom and top side. The measurements were conducted in helium atmosphere at a pressure of 980 mbar. The measurement was fitted with the radiation fit model provided by the software Aprosoft Laser Flash Evaluation v.1.06. Three measurements were performed at every temperature to obtain a mean thermal diffusivity of every individual sample. For data evaluation, the mean thermal diffusivity of three individual samples was taken into account. Due to the changes in thickness of the sample during sintering, the thickness of the samples has to be corrected accordingly. Further details are provided in the supporting information.

Density determination: The density of the pristine crystals was obtained by determining the mass and volume of the monolith. The mass was obtained by weighting the crystals. The volume was determined on a Keyence V 3100 3D digital macroscope. The density of the molten crystals was measured by a buoyancy balance according to Archimedes principle.

Differential scanning calorimetry: Differential scanning calorimetry was performed on a TA Instruments Q1000 differential scanning calorimeter according to ASTM E1269.

Three individual measurements were performed under a nitrogen flow of 50 mLmin^{-1} at a heating rate of 20 Kmin^{-1}. Two heating cycles were conducted between –40 °C and 200 °C. The specific heat capacity was extracted from the second heating cycle.

References and Notes

1. V. Kubytskyi, S.-A. Biehs, P. Ben-Abdallah, Radiative bistability and thermal memory. Phys. Rev. Lett. 113, 074301 (2014).
2. L. Wang, B. Li, Thermal memory: A storage of phononic information. Phys. Rev. Lett. 101, 267203 (2008).
3. M. Wuttig, N. Yamada, Phase-change materials for rewriteable data storage. Nat. Mater. 6, 824-832 (2007).
4. J. Zhu et al., Temperature-gated thermal rectifier for active heat flow control. Nano Lett. 14, 4867-4872 (2014).
5. G. Wu, B. Li, Thermal rectification in carbon nanotube intramolecular junctions: Molecular dynamics calculations. Phys. Rev. B 76, 085424 (2007).

6. C. W. Chang, D. Okawa, A. Majumdar, A. Zettl, Solid-state thermal rectifier. Science 314, 1121-1124 (2006).
7. M. Liu, Y. Ma, H. Wu, R. Y. Wang, Metal matrix–metal nanoparticle composites with tunable melting temperature and high thermal conductivity for phase-change thermal storage. ACS Nano 9, 1341-1351 (2015).
8. M. Chau et al., Reversible transition between isotropic and anisotropic thermal transport in elastic polyurethane foams. Materials Horizons 4, 236-241 (2017).
9. H.-K. Lyeo et al., Thermal conductivity of phase-change material Ge2Sb2Te5. Appl. Phys. Lett. 89, 151904 (2006).
10. M. Farhat et al., Thermal invisibility based on scattering cancellation and mantle cloaking. Scientific Reports 5, 9876 (2015).
11. M. J. Dicken et al., Frequency tunable near-infrared metamaterials based on vo2 phase transition. Opt. Express 17, 18330-18339 (2009).
12. C. Dames, Solid-state thermal rectification with existing bulk materials. J. Heat Transfer 131, 061301 (2009).
13. S. Kommandur, S. K. Yee, An empirical model to predict temperature-dependent thermal conductivity of amorphous polymers. J. Polym. Sci., Part B: Polym. Phys., 1160–1170 (2017).
14. P. Ben-Abdallah, S.-A. Biehs, Near-field thermal transistor. Phys. Rev. Lett. 112, 044301 (2014).
15. R. G. Moore et al., A surface-tailored, purely electronic, mott metal-to-insulator transition. Science 318, 615-619 (2007).
16. T. Zhang, T. Luo, High-contrast, reversible thermal conductivity regulation utilizing the phase transition of polyethylene nanofibers. ACS Nano 7, 7592-7600 (2013).
17. J. F. Ihlefeld et al., Room-temperature voltage tunable phonon thermal conductivity via reconfigurable interfaces in ferroelectric thin films. Nano Lett. 15, 1791-1795 (2015).

18. R. Chen et al., Controllable thermal rectification realized in binary phase change composites. Scientific Reports 5, 8884 (2015).
19. P. C. Sun et al., Room temperature electrical and thermal switching cnt/hexadecane composites. Adv. Mater. 25, 4938-4943 (2013).
20. R. Zheng, J. Gao, J. Wang, G. Chen, Reversible temperature regulation of electrical and thermal conductivity using liquid–solid phase transitions. Nat. Commun. 2, 289 (2011).
21. Y. Li et al., Temperature-dependent transformation thermotics: From switchable thermal cloaks to macroscopic thermal diodes. Phys. Rev. Lett. 115, 195503 (2015).
22. M. D. Losego, I. P. Blitz, R. A. Vaia, D. G. Cahill, P. V. Braun, Ultralow thermal conductivity in organoclay nanolaminates synthesized via simple self-assembly. Nano Lett. 13, 2215-2219 (2013).
23. W.-L. Ong, S. M. Rupich, D. V. Talapin, A. J. H. McGaughey, J. A. Malen, Surface chemistry mediates thermal transport in three-dimensional nanocrystal arrays. Nat. Mater. 12, 410-415 (2013).
24. T. Still, W. Cheng, M. Retsch, U. Jonas, G. Fytas, Colloidal systems: A promising material class for tailoring sound propagation at high frequencies. J. Phys.: Condens. Matter 20, 404203 (2008).
25. T. Still et al., Simultaneous occurrence of structure-directed and particle-resonance-induced phononic gaps in colloidal films. Phys. Rev. Lett. 100, 194301 (2008).
26. T. Still et al., Vibrational eigenfrequencies and mechanical properties of mesoscopic copolymer latex particles. Macromolecules 43, 3422-3428 (2010).
27. S. G. J. John D. Joannopoulos, Joshua N. Winn, Robert D. Meade, Photonic crystals: Molding the flow of light. (Princeton University Press, 2008).
28. W. Cheng, J. Wang, U. Jonas, G. Fytas, N. Stefanou, Observation and tuning of hypersonic bandgaps in colloidal crystals. Nat. Mater. 5, 830-836 (2006).

29. E. Alonso-Redondo et al., A new class of tunable hypersonic phononic crystals based on polymer-tethered colloids. Nat. Commun. 6, 8309 (2015).
30. K. R. Phillips et al., A colloidoscope of colloid-based porous materials and their uses. Chem. Soc. Rev. 45, 281-322 (2016).
31. N. Vogel, M. Retsch, C. A. Fustin, A. Del Campo, U. Jonas, Advances in colloidal assembly: The design of structure and hierarchy in two and three dimensions. Chem. Rev. 115, 6265-6311 (2015).
32. M. Retsch et al., Fabrication of large-area, transferable colloidal monolayers utilizing self-assembly at the air/water interface. Macromol. Chem. Phys. 210, 230-241 (2009).
33. F. A. Nutz, P. Ruckdeschel, M. Retsch, Polystyrene colloidal crystals: Interface controlled thermal conductivity in an open-porous mesoparticle superstructure. J. Colloid. Interf. Sci. 457, 96-101 (2015).
34. F. A. Nutz, M. Retsch, Interfacial and volumetric sensitivity of the dry sintering process of polymer colloidal crystals: A thermal transport and photonic bandgap study. Phys. Chem. Chem. Phys. 19, 16124-16130 (2017).
35. J. W. Goodwin, J. Hearn, C. C. Ho, R. H. Ottewill, Studies on the preparation and characterisation of monodisperse polystyrene latices. Colloid. Polym. Sci. 252, 464-471 (1974).
36. R. H. Ottewill, J. N. Shaw, Studies on the preparation and characterization of monodisperse polystyrene latices. Kolloid Z. Z. Polym. 215, 161-166 (1967).
37. L. Dusza, Combined solution of the simultaneous heat loss and finite pulse corrections with the laser flash method. High Temperatures - High Pressures 27, 467-473 (1995).
38. W. J. Parker, R. J. Jenkins, C. P. Butler, G. L. Abbott, Flash method of determining thermal diffusivity, heat capacity, and thermal conductivity. J. Appl. Phys. 32, 1679-1684 (1961).

Acknowledgments

The authors thank Ute Kuhn for help with DSC experiments. We also thank Sabrina Thomae who was involved in the sample preparation and the first experiments of this work.

Funding: This project was funded by the Volkswagen Foundation (Lichtenberg professorship). Additional support was provided by the SFB840.

Author contributions

M.R. supervised this work. F.A.N designed and performed the experiments. F.A.N evaluated the data and wrote the manuscript under the guidance of M.R.

Competing interests

The authors declare no competing financial interests

Supporting Information

Tailor Made Temperature Dependent Thermal Conductivity: The Power of Interparticle Constriction

Fabian A. Nutz and Markus Retsch

Table S1: Hydrodynamic diameter, PDI, hard sphere diameter and T_g of particles employed in this study

	d_h (DLS) nm	PDI (DLS) nm	d (SEM) nm	T_g °C
100% MMA-1	258	0.008	223 ± 8	127
100% MMA-2	495	0.034	427 ± 18	124
10 vol% nBA-co-90 vol% MMA-1	212	0.039	182 ± 11	103
10 vol% nBA-co-90 vol% MMA-2	493	0.022	403 ± 13	103
20 vol% nBA-co-80 vol% MMA-1	239	0.008	214 ± 7	74
20 vol% nBA-co-80 vol% MMA-2	517	0.020	421 ± 9	80
20 vol% nBA-co-80 vol% MMA-3	370	0.024	339 ± 7	75
30 vol% nBA-co-70 vol% MMA-1	236	0.029	215 ± 7	54
30 vol% nBA-co-70 vol% MMA-2	499	0.058	434 ± 12	61

Laser flash Analysis (LFA)

Laser Flash Analysis (LFA) was measured on colloidal monoliths possessing a thickness of several hundred micrometers. The monoliths were coated with a thin graphite layer on the bottom a top side before the measurement. The coating ensures a sufficient IR absorption and emission. A xenon lamp emits a light pulse onto the sample. The thermal energy of the light pulse is absorbed at the bottom graphite layer and travels through the specimen. The thermal energy is then emitted from the top side. This temperature rise is recorded in dependence of the elapsed time since the light pulse by a fast mid-infrared detector. A numerical fitting procedure provided by the commercial software package Aprosoft Laser Flash Evaluation v1.06 based on the one-dimensional temperature diffusion equation was used to determine the thermal diffusivity α.(37) For this, accurate knowledge of the sample thickness is a prerequisite, as the thickness strongly influences half-rise time as given by:

$$\alpha = \frac{1.38 \cdot d^2}{\pi^2 \cdot t_{\frac{1}{2}}}$$

$t_{1/2}$ represents the time need for the half maximum temperature rise at the top surface.(38) The thermal conductivity κ of the sample is calculated by

$$\kappa(T) = \alpha(T) \cdot c_p(T) \cdot \rho(T)$$

with the specific heat capacity c_p and the density ρ.

The temperature dependent specific heat of the investigated polymers are displayed in Figure S1.

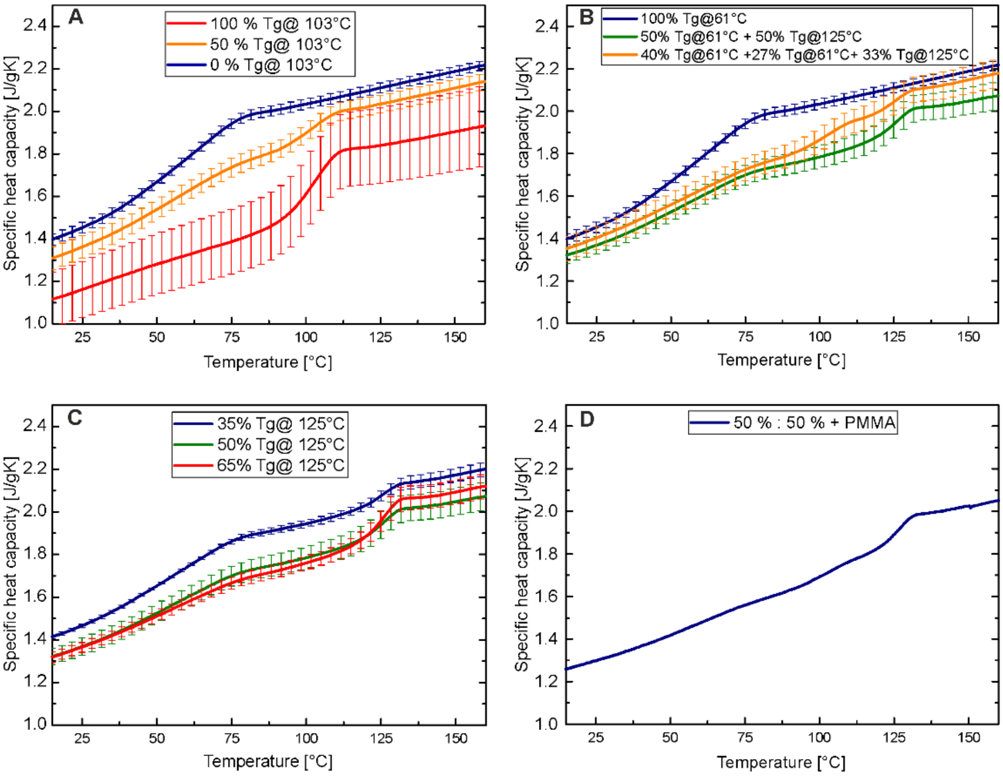

Figure S1: Temperature dependent specific heat capacity of the investigated samples. (A) broad transition (see Figure 3); (B) multiple transitions (see Figure 4); (C) transition height (see Figure 5); (D) combination of broad and step like transition (see Figure 6). Error bars are standard deviations based on three individual measurements of the polymers.

Thickness and density assumptions for LFA evaluation

Due to experimental limits, it is not possible to follow changes of the sample thickness d in-situ during the LFA measurement. Since α is proportional to d^2 and the polymer colloidal crystals decrease their thickness during the sintering process, it is necessary to pre-determine the temperature dependent thickness behavior of the investigated samples to obtain accurate values for α, as well as changes in density based on the loss of porosity. The assumptions made for the differently assembled specimens are elucidated in the following.

Single T_g colloidal monoliths (Figure 2): The thickness and density of the colloidal monoliths was measured before and after the temperature dependent LFA experiment. Since these crystals show a sharp increase of its thermal conductivities at T_g, a step function has been applied to the temperature dependent thickness and density behavior.(33) This was done by using the thickness/density measured before the LFA experiment until T_g, and the thickness/density values measured after the LFA experiment after exceeding T_g for calculations of α and κ.

Co-assembled colloidal crystals (broad transition, Figure 3): The initial and final thickness and density were determined before and after the LFA measurement. To determine the temperature dependent thickness/density behavior, several co assembled colloidal crystals were annealed at various temperatures for 30 min. The thickness and density of the co-assembled crystals were measured after the annealing step. The relative loss in thickness and the temperature-dependent density are shown in Figure S2.

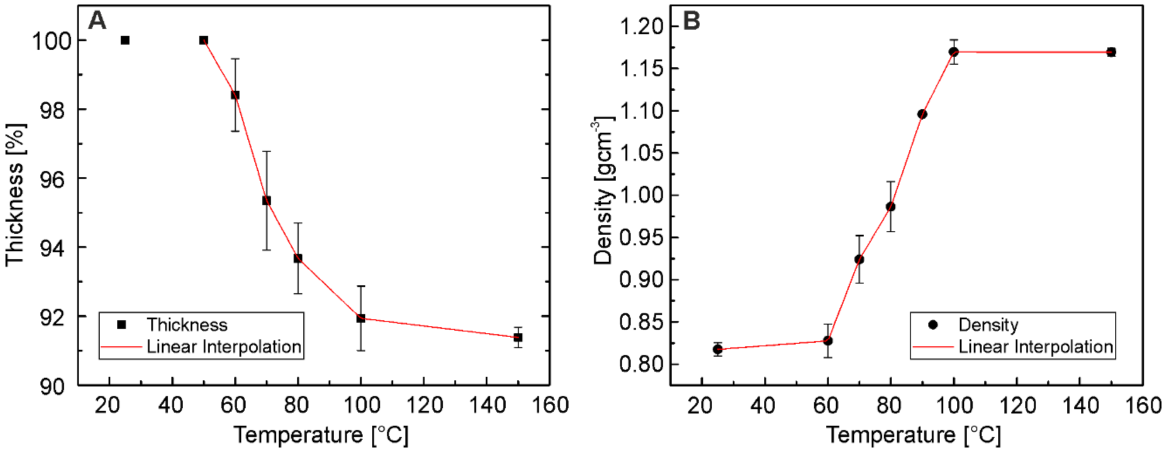

Figure S2: Temperature dependent behavior of thickness (A) and density (B) for co assembled colloidal crystals. The linear interpolation is displayed as a red line. While the thickness decreases during heating, the density increases. Error bars result from three individual measurements.

The temperature dependent thickness and density profile were then adapted for the calculations of α and κ.

Multi-layered colloidal monoliths (multiple steps): The thickness and density of the colloidal monoliths were measured before and after the temperature dependent LFA experiment. The thickness/density was assumed to decrease/increase in a step like manner at the specific T_g, corresponding to the relative amounts of particle dispersion used for each layer.

The combination of a broad transition followed by a step like increase: A linear decrease/increase of the thickness/density to 50 % of the overall decrease/increase has been assumed for the broad transition until the glass transition temperature of the higher melting particle within the co-assembly layer. Additionally, a decreasing/increasing step function was applied for the thickness and density at the T_g of the upper PMMA particle layer.

Thickness-corrected thermal diffusivity

To ensure that the presented trends do not arise from density or specific heat corrections, the thickness corrected thermal diffusivity obtained from the XFA experiment are displayed in Figure S3. Without thickness correction, the steps and transitions would be even more pronounced.

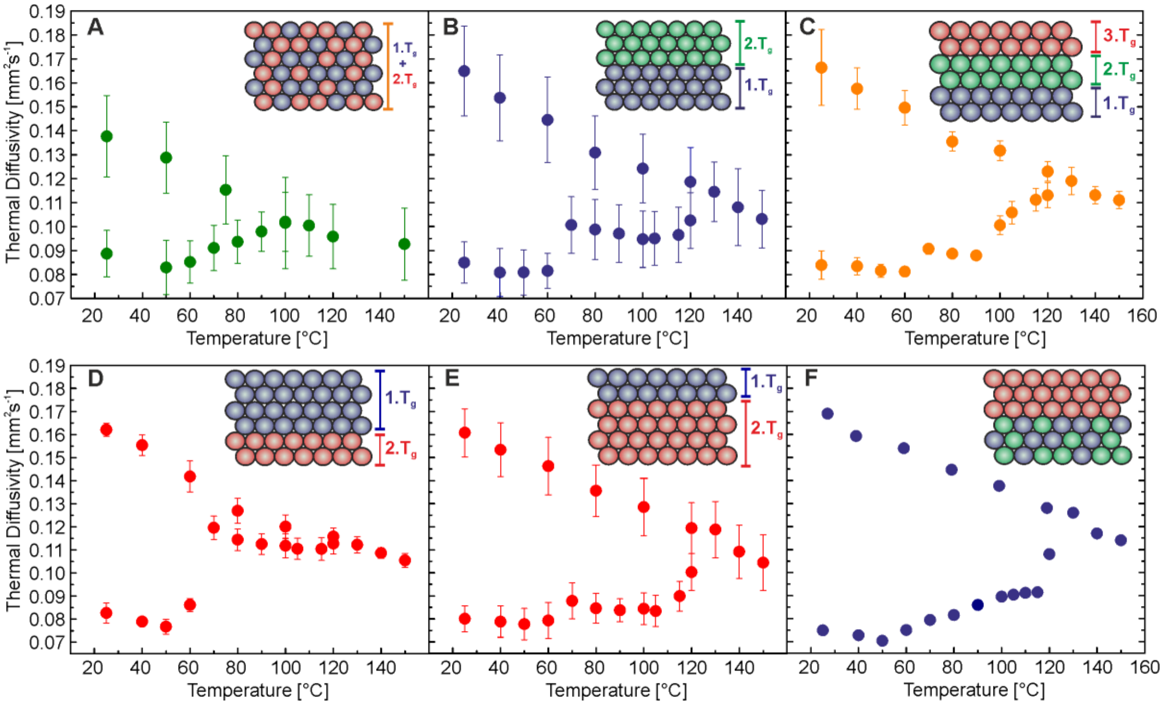

Figure S3: Temperature-dependent and thickness corrected thermal diffusivity of the measured colloidal specimens. The structure is indicated by the schemes within the graphs. (A) broad transition; (B) two step and (C) three step transition; tuning the transition height (D) 65 % : 35 % and (e) 35 % : 65 %; (F) Combination of broad and sharp transition. Error bars arise from three individual measurements.

Thermal conductivity of co-assembled colloidal crystals

Although 50 %:50 % co assembled colloidal crystals do show a broad transition between both T_g of the particles used for the assembly, this behavior has not been observed for other mixtures. The temperature dependent thermal conductivity of a 75 %:25 % and 25 %:75 % mixture are illustrated in Figure S4.

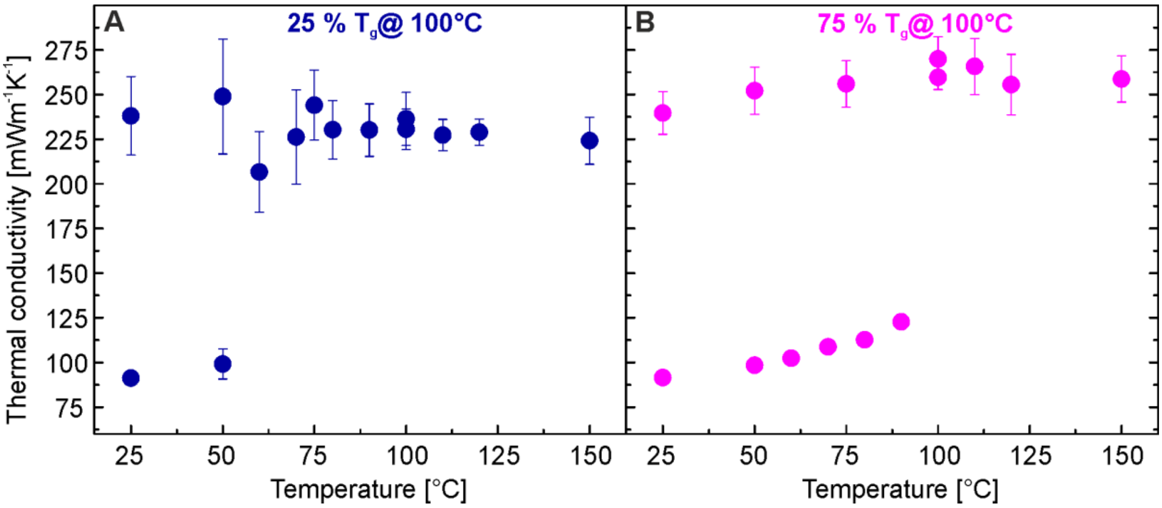

Figure S4: Temperature-dependent thermal conductivity of co assembled colloidal crystals from two particles possessing a T_g of ~61 °C and ~103 °C. Only a step like increase is visible for compositions of (A) 25 %:75 % and (B) 75 %:25 %. Error bars arise from three individual measurements.

Only a step-like increase of the thermal conductivity of these assemblies is visible at the correspond T_g of the majority polymer particle.

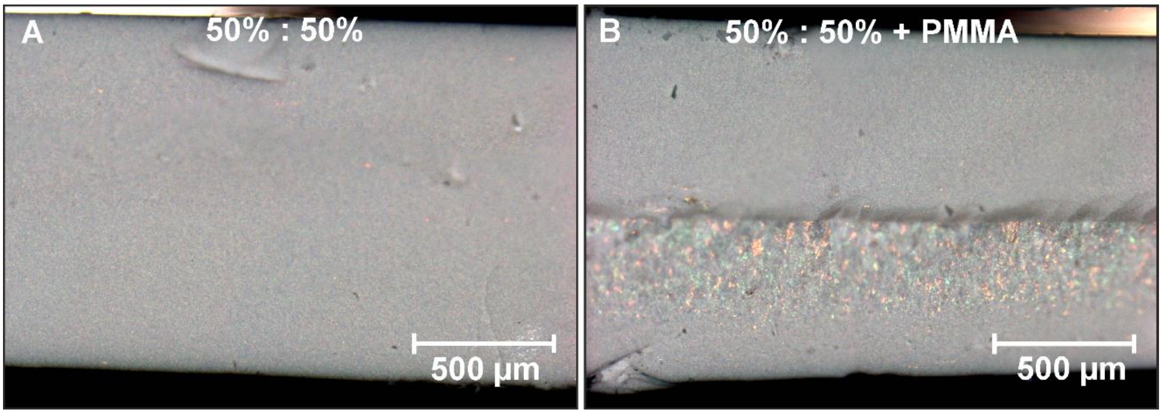

Figure S5: Optical micrographs of a two layer colloidal monolith) made by filtration, and a two layer monolith fabricated by a combination of evaporation induced self-assembly and filtration. (A) Only weak opalescence is visible throughout the entire monolith based on the fast sample preparation which prevents the particles from large area crystallization. (B) Based on the evaporation induced co assembly of the bottom layer, this layer shows opalescence colours due to Bragg reflection, whereas the upper layer fabricated by filtration does not.

4.4 Constricted Thermal Conductivity through Dense Particle Packings with Optimum Disorder

Fabian A. Nutz, Alexandra Philipp, Martin Dulle, Markus Retsch

Prof. Dr. Markus Retsch, Fabian A. Nutz, Alexandra Philipp
University of Bayreuth, Physical Chemistry – Polymer Systems, Universitaetsstr. 30, 95447 Bayreuth, Germany
Dr. Martin Dulle
JCNS-1/ICS-1: Neutron Scattering, Forschungszentrum Jülich GmbH, Wilhelm-Johnen-Straße, 52428 Jülich

Tabel of content figure

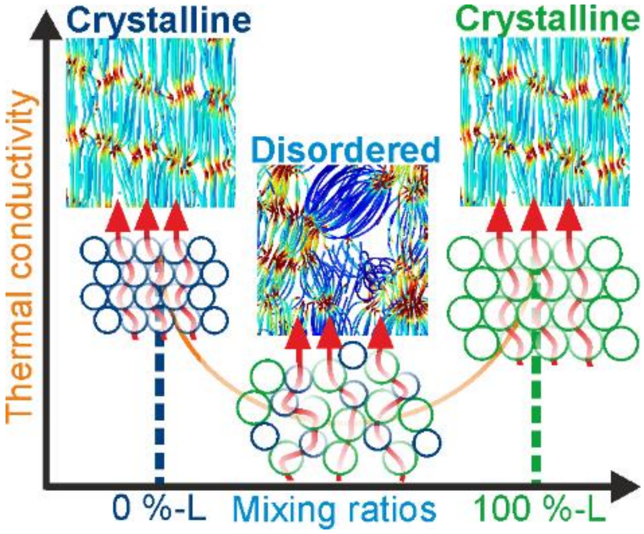

Keywords: colloidal glasses; thermal transport; photonic crystals; next neighbor correlation; amorphous limit

Abstract

Heat transport plays a critical role in modern batteries, electrodes, and capacitors. This is caused by the ongoing miniaturization of such nanotechnological devices, which increases the local power density and hence temperature. Even worse, the introduction of heterostructures and interfaces is often accompanied by a reduction in thermal conductivity – which can ultimately lead to the failure of the entire device. Surprisingly, a fundamental understanding of the governing heat transport processes even in simple systems, such as binary particle mixtures is still missing. This contribution closes this gap and elucidates how strongly the polydispersity of a model particulate system influences the effective thermal conductivity across such a heterogeneous system. In a combined experimental and modelling approach, well-defined mixtures of monodisperse particles with varying size ratios were investigated. The transition from order to disorder can reduce the effective thermal conductivity by as much as ~50 %. This is caused by an increase in the thermal transport path length and is governed by the number of interparticle contact points. These results are of general importance for many particulate and heterostructured materials and will help to conceive improved device layouts with more reliable heat dissipation or conservation properties in the future.

Introduction

Materials with low thermal conductivity are employed in many fields such as clothing, refrigeration, building insulation, or thermoelectrics.[1] Concepts to reduce the thermal conductivity of a given material either target the material composition or its nano-, meso-, or microstructure. Generally, for bulk materials, a high thermal conductivity is found in crystalline solids where phonons are able to transport thermal energy over several hundred nanometers based on a well-defined crystal lattice.[2-5] In contrary, low thermal conductivities are mostly found in disordered, amorphous materials. Based on an increased scattering at the disordered structure, the mean free path of phonons is strongly reduced, resulting in diffusive thermal transport.[6, 7] Allen and Feldman[8, 9] proposed three different vibrational modes, namely diffusons, propagons, and locons, to describe thermal transport in amorphous matter. Increasing phonon scattering in bulk materials, subsequently leads to a reduction in thermal conductivity. In dense materials this can be achieved by layered structures,[10, 11] doping[12, 13] or the embedding of nanoparticles,[14, 15] where particularly crystalline solids are strongly affected. Zhang and Minnich investigated how nanoparticle clusters with a particular size distribution can lower the thermal conductivity in crystalline silicon even below its amorphous limit.[14]

Besides the chemical composition of a certain material, the influence of the overall structure is of high importance, too. The most obvious and well-known structural influence is given by the introduction of porosity. This severely decreases the density of a bulk material and consequently reduces the effective thermal conductivity. Depending on the cell size of the porous material, highly insulating properties are accessible.[16-19] Moreover, classical porous, granular matter becomes increasingly important for a range of applications, which involve heterostructures and interfaces. For instance, thermal management in high-density storage devices such as batteries or supercapacitors is a critical safety concern. [20-22]

Colloidal assembly structures have been proven to be particular suitable to investigate the influence of three-dimensional nanostructuring on the effective thermal transport in granular matter.[23] The thermal conductivity of colloidal crystals is mainly governed by the geometrical constrictions at the interparticle contact points, and the material of the particles itself.[23-25] While most colloidal assembly structures targeted periodically ordered materials, the controlled introduction of disorder also showed to provide fundamental insights, for instance into the physics of phononic bandgaps.[27]

In this work, we provide a conceptual understanding of the influence of structural order on the thermal transport properties in particulate mesostructures. Therefore, binary colloidal assemblies were fabricated from two monodisperse, differently sized polystyrene (PS) particles. These buildings blocks are easily accessible by common polymerization techniques [27, 28] and their self-assembly into superstructures is well established.[29] By mixing two differently sized particles, it is possible to control the structural order of the resulting colloidal assembly. We clarify the underlying effect of the thermal conductivity reduction by finite element modeling combined with molecular dynamic simulations. We further demonstrate how to reduce heat transport in disordered binary assemblies in a rational way.

Binary colloidal assemblies of PS particles possessing a diameter of 243 nm (S) and 306 nm (L) were fabricated by evaporation-induced self-assembly (size ratio ~0.8). For spectroscopic characterization, binary assemblies were additionally immobilized on a glass slide by dip coating of a 3 wt% of aqueous particles dispersions. The mixing ratio ranged from 0 vol%-L to 100 vol%-L. Optical microscopy and scanning electron images of the edges of split monoliths are shown in Figure 1a and b and provide a qualitative expression of how the mixing ratio translates into order and disorder.

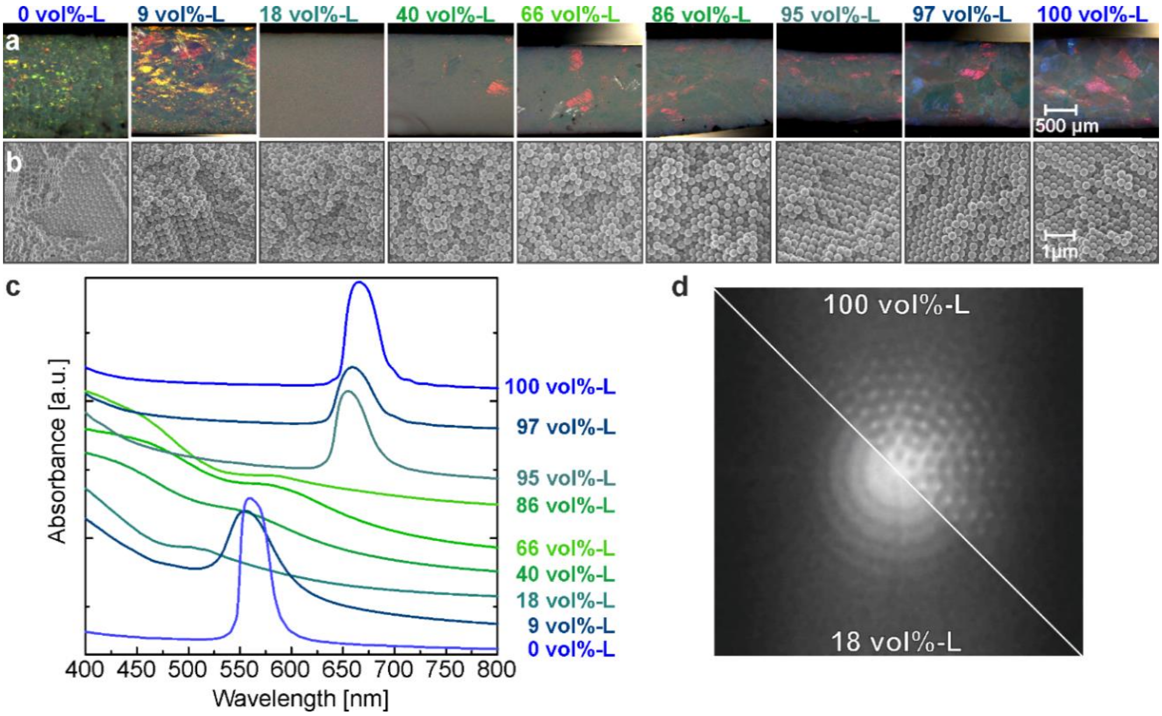

Figure 1. Structural characterization of binary colloidal assemblies. (a) Optical and (b) scanning electron microscopy side view images of the edges of split colloidal monoliths. (c) UV-vis transmission spectra measured on dip-coated assemblies. (d) Fast Fourier transformation (FFT) images from scanning electron micrographs with a mixing ratio of 18 vol%-L compared to a FFT image of 100 vol%-L colloidal crystal.

From optical microscopy (Figure 1a), strong opalescent colors are visible for samples consisting of only one particle type (0 vol%-L and 100 vol%-L) as well as for binary assemblies only containing a small amount of differently sized specimen (9 vol%-L, 95 vol% L, and 97 vol%-L). This is due to Bragg reflection. The difference in color between 0 vol%-L and 100 vol%-L monoliths arises from the size dependence of the Bragg reflectivity. Different colors within one monolith can be attributed to the angle dependence of the Bragg law, based on different crystal planes exposed to the surface.

For other mixing ratios, only weak overall Bragg reflection (66 vol%-L and 86 vol%-L) or almost only diffuse scattering (18 vol%-L and 40 vol%-L) is visible. At these mixing ratios, the polydispersity of the binary particle dispersion prevents large area particle crystallization. Noteworthy, some embedded crystalline regions are observable for several intermediate mixing ratios (40 vol%-L, 66 vol%-L, and

86 vol%-L). This can be explained by the strong tendency of demixing in binary colloidal dispersions.[30-32] The slow self-assembly process (several days) of the dispersion enables the formation of phase separated, multicrystalline, and amorphous areas.

Scanning electron microscopy (SEM) images validate the optical impression (Figure 1b). The pure colloidal crystals feature a high degree of crystalline particle ordering. In contrast, for intermediate mixing ratios, only a random packing of the particles is observed. This is additionally highlighted by fast Fourier transformation (FFT) images of the SEM images illustrated in Figure 1d. Whereas distinct reflexes are visible for 100 vol%-L due to the hexagonal symmetry of the particle lattice, only smeared Debye-Scherrer rings are obtained for 18 vol%-L monoliths. The smearing is based on the disordered mesostructure whereas the observed Debye-Scherrer rings arise from the different particle diameters present within the monoliths.

We further quantify the intrinsic order of the binary colloidal films by UV-vis transmission spectra of dip coated samples, displayed in Figure 1c. A strong Bragg peak is visible for 0 vol%-L colloidal crystals at a wavelength of 559 nm. At small mixing ratios of 9 vol%-L, the Bragg peak broadens and the maxima is less allocable due to the disturbance of the crystal lattice. A further increase of the large particle volume fraction to 18 vol%-L leads to a vanishing of the Bragg peak. For intermediate mixing ratios from 44 vol%-L to 86 vol%-L no distinct Bragg peaks are observable, indicating a randomly packed structure. The Bragg peak of the larger particle species reoccurs at 95 vol%-L and reaches a maximum intensity for 100 vol%-L at a wavelength 667 nm.

Optical microscopy, SEM, and UV-vis characterization prove the highly crystalline nature of the homo-particle ensembles, which define the edges of the mixture phase diagram. The long range order is quickly lost, when mixing two particles with a size ratio of 0.8. Depending on the assembly process a complete suppression of crystallinity can be found (dip-coating) or small, multicrystalline regions caused by demixing prevail (dispersion drying).

Laser flash analysis (LFA) was performed on colloidal monoliths obtained from evaporation induced self-assembly. By determining the sample density and specific heat capacity, it is possible to calculate the specimen's effective thermal conductivity (details see supporting information). The thermal conductivity, normalized to the maximum initial value of the pure colloidal assemblies, as well as the normalized thermal conductivity of intermediate mixing ratios are show in Figure 2a. The color code helps to separate highly ordered samples (blueish) from randomly packed assemblies (greenish) and correspond to the mixing ratios given in Figure 1.

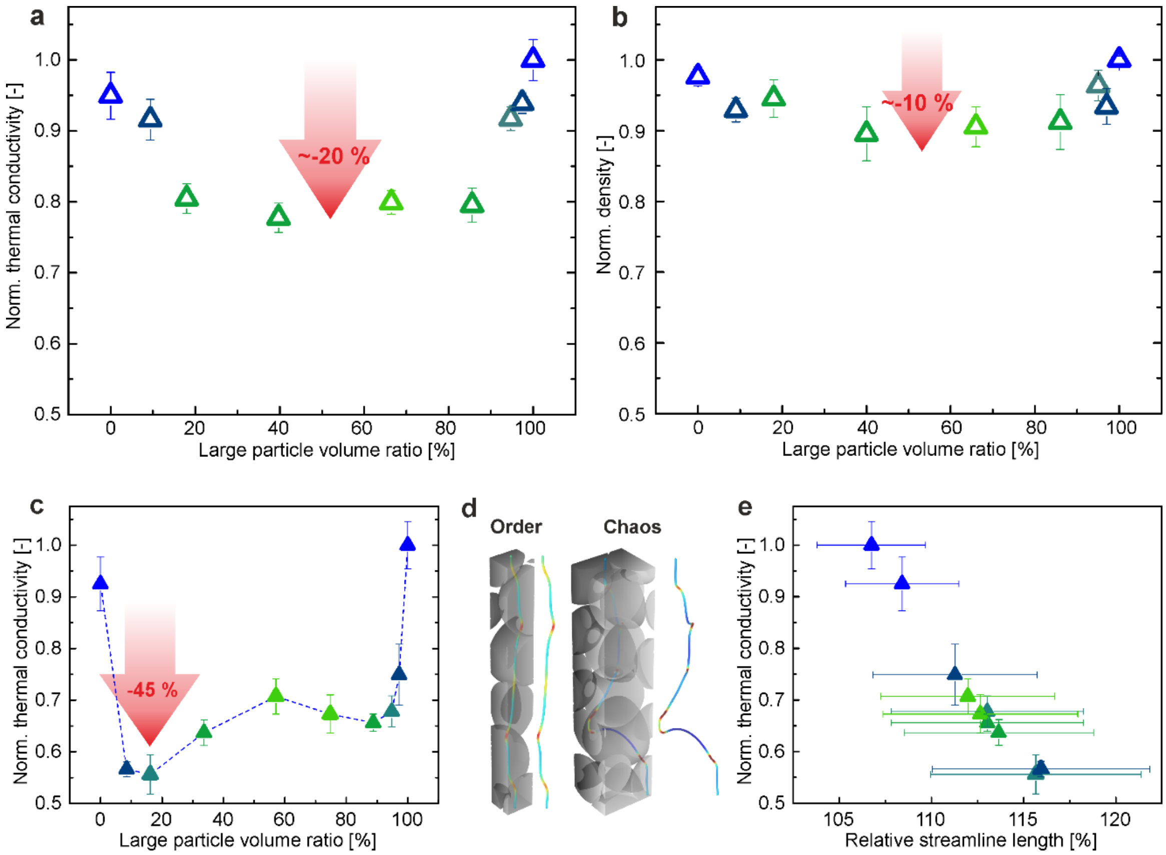

Figure 2. Thermal conductivity of the investigated assemblies with a size ratio of 0.8. Color code indicates ordered (blueish) and disordered assemblies. (a) Normalized thermal conductivity of binary PS colloidal assemblies possessing different mixing ratios. Red arrow indicates the reduction of the thermal conductivity due to the introduced disorder. (b) Normalized density of the colloidal assemblies. (c) Thermal conductivity vs. volume fraction of large particles obtained by FEM. Error bars arise from three individual simulations boxes at three different directions in space. (d) Exemplary streamlines present within a crystalline and a disordered assembly with a size ratio of 0.8 and 16 vol%-L. (e) Thermal conductivity vs. relative streamline length of various size ratios. Error bars arise from three individual simulations boxes at three different directions in space.

Homo-particle colloidal assemblies (mixing ratio 0 vol% L and 100 vol% L) show a thermal conductivity of 73 $mWm^{-1}K^{-1}$ and 77 $mWm^{-1}K^{-1}$ in absolute numbers, respectively. At small mixing ratios of differently sized particles, the thermal conductivity slightly drops to ~0.93 of the initial value. For intermediate mixing ratios, the thermal conductivity drops significantly to ~0.80. This reduction can only partially be explained by the reduced density of the intermediate assemblies as displayed in Figure 2b. The reduction of the density for intermediate mixing ratios originates from the prevented close packing of the particles during assembly. This leads to a space filling which deviates from the maximum of 74 %.

Still, the density only decreases to ~90 % of its initial value. Therefore, an additional effect is present, which is responsible for the overall reduction of the thermal conductivity to 80 %.

To elucidate this additional contribution, we performed finite element modeling (FEM) on binary particle mixtures possessing a size ratio of 0.8. The required virtual assemblies were obtained by molecular dynamic (MD) simulations of the assembly process. Exemplary particle assemblies obtained from MD simulations are shown in Figure S2a. We found highly crystalline particle assemblies at the edges of the mixing diagram. In contrast to our experimental findings, the crystallization process is already fully prevented at very small mixing ratios (Figure S2a, left). This is caused by the lack of demixing or phase separation of the particles due to the short assembly time-scale used for the MD simulation. FFT images of 0 vol%-L and 9 vol%-L assemblies from MD simulation are compared to the experiment in Figure S2a, right. Thus, the fully amorphous structure obtained from the MD simulation can be regarded as an ideally disordered case. Experimentally, some degree of crystallization will be difficult to exclude owing to the long timescale allowed for the self-assembly process. FEM has been done using the software COMSOL Multiphysics®. Details on the modeling are described in the Supporting Information. The calculated thermal conductivity against the volume fraction of large particles is displayed in Figure 2c. Analogous to Figure 2a, the color code indicates ordered (bluish) and disordered assemblies (green). The mixing diagram shows a similar trend for the thermal conductivity as observed for the experiment, with high thermal conductivities for ordered, and a reduced thermal conductivity for disorder assemblies. A minimum thermal conductivity of only 55 % of the initial value is observed at a volume fraction of ~16 vol%-L. This is an almost two fold enhancement of the insulation capability caused by the disordered structure, and it is significantly lower compared to the experimental results. We ascribe this deviation to the structural difference between the MD simulation and the experiment. As outlined before, by MD simulation one can observe a more homogeneous distribution of both particle types within the monolith, leading to a stronger reduction of the thermal conductivity.

To explain the origin of the thermal conductivity reduction beyond the decrease in density, we utilized FEM to analyze the length of the thermal transport pathway through such a particulate assembly structure. This can be done by evaluating the length of heat flux streamlines, which reach from the hot to the cold side of the simulation box. Figure 2d shows two individual cases through an ordered (100 vol%-L) and disordered (~16 vol%-L) particle ensemble. Whereas in the ordered case, a rather straight and unperturbed streamline is obtained, the introduction of disorder strongly bents and perturbes the thermal transport path. The statistic evaluation over the entire simulation box is given in Figure 2e, where we normalized the streamline length on the length of the simulation box. The relative streamline length increases with increasing disorder, which can be inferred from the bluish to greenish color code. One also finds a direct correlation between the streamline length and the thermal conductivity reduction. This finding can be intuitively explained by a sort of effective thermal length, which differs from the plain geometric size of the box. One may draw an analogy to the concept of optical path length in a material, which is governed by its refractive index.

Most interestingly, the FEM simulation finds a strongly asymmetric shape of the thermal conductivity reduction with two minima at moderately high and low mixing ratios, respectively. These are not found in the experiment, presumably due to the presence of mesocrystalline domains, embedded in the amorphous structure. We now want understand the origin of these minima and how the thermal conductivity could be reduced even further. This question could be rephrased to how the thermal streamline lengths can be further increased in such colloidal superstructures. We therefore return to MD simulation and evaluate the local structure around one particle more explicitly. Quite expectedly, when introducing disorder the average number of next neighbors is reduced. For crystalline assemblies, one can find an average number of next neighbors per particles of ~12, based on the face centered cubic symmetry. For all disordered intermediate mixing ratios, the number of next neighbors is reduced to ~10 (Figure S2b). One can imagine that this reduction leads to less pathways for heat to travel through the particle structures and therefore reduces the thermal conductivity of the assemblies. However, we find that the mean number of next neighbor particles merely reaches a broad plateau, and doesn't explain the asymmetric shape shown in Figure 2c. We therefore evaluated the actual number of next neighbor particles explicitly. This is shown in Figure 3, where we present the next neighbor histograms at selected mixing ratios (bottom row). We chose a special illustration, to highlight the structural heterogeneity, when heat travels through such a system. We, therefore, present a projection of all particles with the same number of next neighbors that can be found within the simulated box. The color code indicates particles possessing different numbers of next neighbors from high (blue) to low (red). It therefore provides a direct impression of how many interparticle contact points are available for thermal transport from one particle to the next.

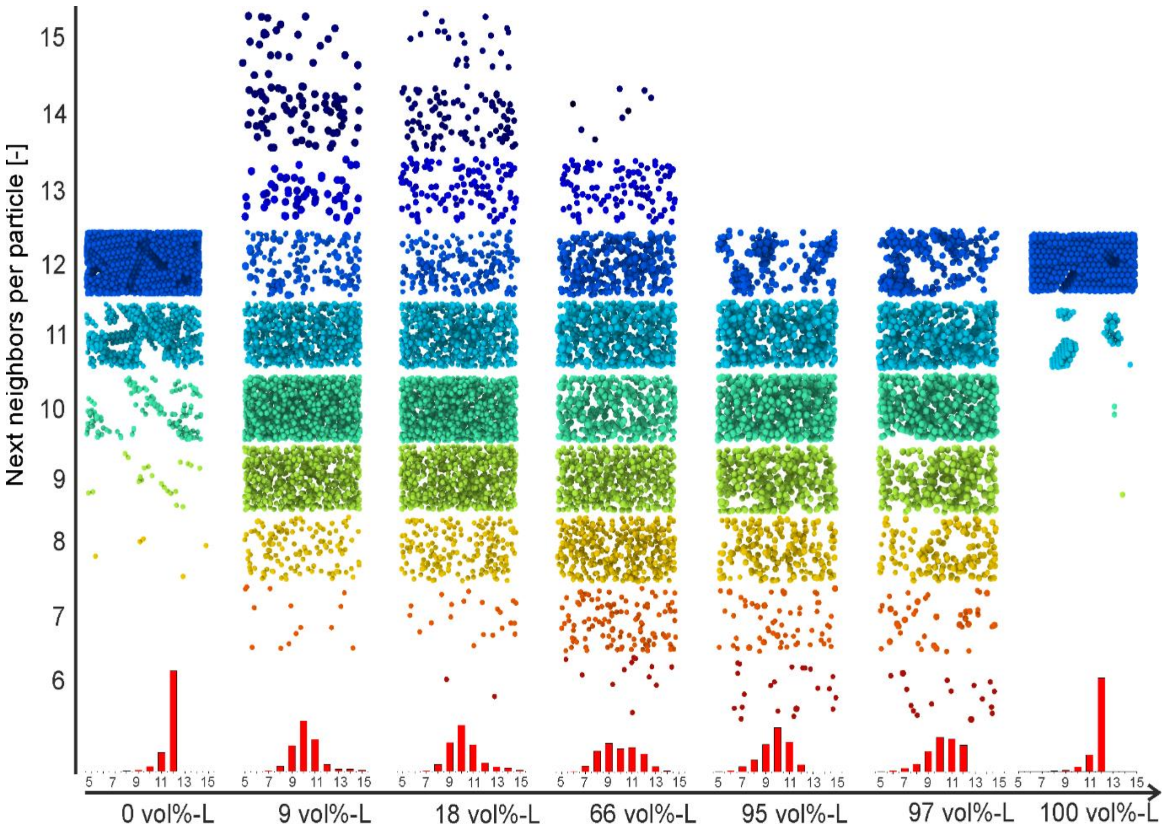

Figure 3. Molecular dynamics simulations of the assembly process of a binary particle mixture. Number of next neighbors per particle against volume fraction of large particles. Size ratio is 0.8. Projection of the assemblies visualize the particles possessing the indicated number of neighbors. Histograms show the relative frequency of particle neighbors per particle present within the different assemblies.

For mixing ratios of 0 vol%-L and 100 vol%-L almost every particle possesses twelve next neighbors. This indicates a nearly fully crystalline face-centered cubic assembly, with few line and point defects being visible. The particle neighbor distribution function quickly broadens at intermediate mixing ratios. Most importantly, this distribution function shows a strongly asymmetric behavior. For mixing ratios of 9 vol%-L to 66 vol%-L, even more than twelve neighbors per particles are present within the assembly, whereas for high mixing ratios, the number of next neighbors is limited to twelve. For a low number of large particles (small mixing ratios), it is possible that one large particle is decorated by a high number of smaller particles. In contrary, for high mixing ratios of large particles, it is geometrically not possible to decorate a small particle with a high number of large particles, since there is simply not sufficient space.

The consequence for the effective thermal length is rather surprising. A reduction of next neighbor contact points indeed leads to a reduction in thermal conductivity. However, even more efficient is the introduction of a large amount of many interparticle contact points, since this leads to an even stronger disturbance of the streamline length due to a geometric extension of the predetermined thermal transport path.

To clarify how this transport pathway is governed by the size mismatch of the two particles, we varied the size ratio of the particles between 0.9 and 0.54 at the mixing ratio around 20 vol%-L, which showed the lowest thermal conductivity. Noteworthy for this data set, the experimental samples were prepared by filtration to speed up the assembly time and therefore obtain particles structure, more comparable to the virtual assemblies. Both, experiment and FEM simulation, show a systematic decrease of the thermal conductivity with a decreasing size ratio from 0.9 to 0.54 (Figure 4d).

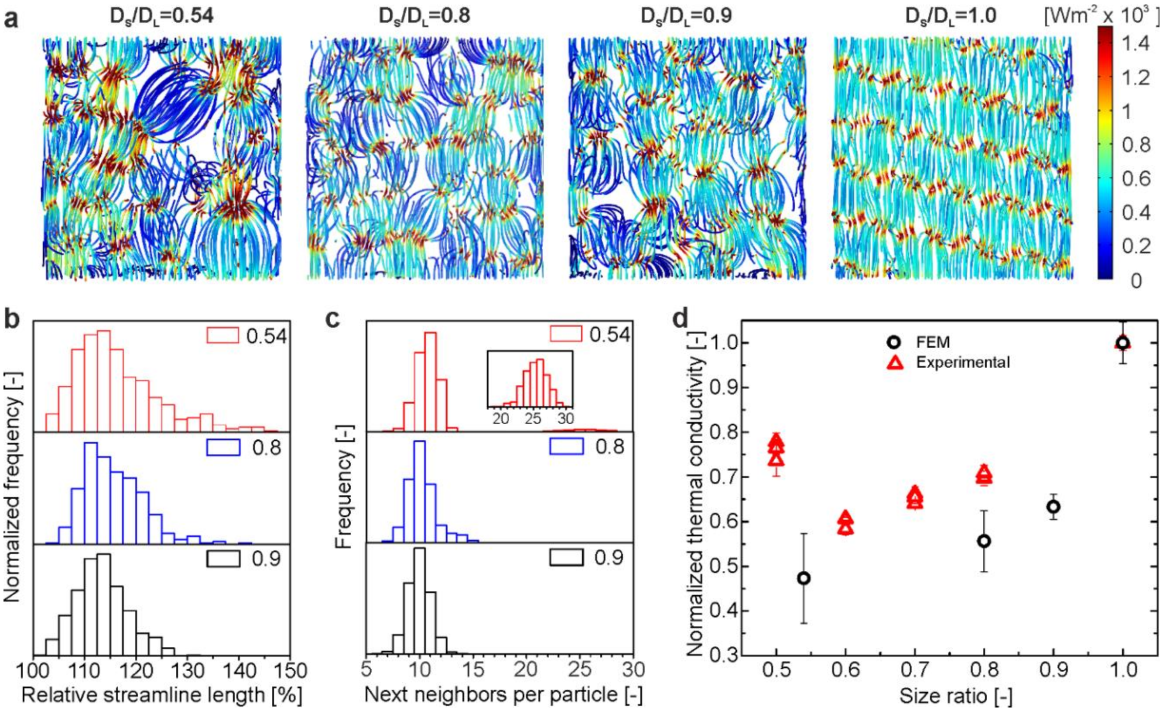

Figure 4. Influence of the size ratio (DS/DL) on the thermal conductivity at ~20 vol% L. (a) Comparison of the heat flux densities of particles assemblies possessing different size ratios. (b) Histograms of the streamline length and (c) next neighbors per particle of the assemblies. (d) Resulting thermal conductivity from FEM compared to experimental data.

The increase of the thermal conductivity for the smallest size ratio (0.54) for the experiment can be explained by an increasing tendency to demix as outlined above. One also needs to take into account that fully crystalline binary assemblies can be obtained for size ratios of <0.41 owing to the octahedral voids in face centered cubic structures, which we approach with this small size ratio.[34]

Figure 4a compares the heat flux density of the particle assemblies from size ratios of 0.54, 0.8, and, 0.9 to the heat flux density of a fully crystalline assembly (size ratio: 1.0). Crystalline assemblies feature uniform and straight streamlines (Figure 4a, 1.0), whereas a decreasing size ratio evokes a high degree of distortion. This is especially obvious for the heat flux density of the size ratio 0.54, where one large particle heavily impedes the heat flux through the entire particle box. The qualitative impression from the heat flux density images is verified by comparing the relative streamline lengths of the different size ratios (Figure 4b). The smaller the size ratio, the higher the number of long streamlines, which can reach up to

140 % relative to the length of the simulation box. This indicates that the less the particle sizes match, the stronger the heat flux is bent along the particle network, leading to an elongation of the thermal transport path.

The higher fraction of long streamlines coincides with a broadening of the next neighbor distribution function with decreasing size ratio (Figure 4c). The broadening increases the number of >10 next neighbors, indicating an increasing decoration of a large particles with small particles. However, due to the small number of large particles at this volume fraction and size ratio combination (about 4 % large particles) this effect is not visible in the average number of neighbors for the whole assembly. Only when looking at the detailed next neighbor histograms the results from the heat flux simulations can be understood (Figure 4c). For a size ratio of 0.54 a second fraction with even 25-30 next neighbors is found. This points to a small amount of large particle clusters, decorated with smaller particles. Overall, the higher mismatch between the two particle sizes led to a thermal conductivity reduction by 40 % (size ratio 0.6) in the experiment and 53 % (size ratio 0.54) in the FEM simulation. We finally also checked, whether 19 vol%-L represents the absolute minimum with respect to the mixing ratio. We, indeed, find the highest fraction of >25 next neighbor particles for this mixing ratio (Figure S4). Higher or lower mixing ratios (± 5 vol%-L) lead rapidly to a reduced number of next neighbors. Therefore, a mixing ratio of 19 vol%-L of large particles is sufficient to strongly reduce the effective thermal transport across a binary particle mixture. Considering number ratios, this is readily achieved by only ~10 %.

Conclusion

In summary, we investigated the influence of order and disorder in particle mixtures on their thermal transport properties. We therefore choose a controlled mixture of binary latex particles as a model system. In a combined approach, which comprised experimental characterization, MD simulation as well as FEM, we were able to relate the observed reduction in thermal conductivity to the local environment of the colloidal particles. Quite surprisingly, the increase of next neighbor contact points at low mixing ratios and at a high size mismatch between the binary spheres, represents the most efficient way to attain a minimum thermal conductivity. The decisive concept is the increase in the effective thermal length, across which the thermal energy needs to be transported. Overall, disorder in a binary colloidal glass can reduce the thermal conductivity by as much as ~50 % compared to its single phase, crystalline counterpart. Our findings are of high importance for heterostructured and particulate materials, for applications were a high insulation, but also a good heat dissipation are paramount. Owing to the diffusive thermal transport in our system, our findings are of conceptual nature and applicable to many other nano-, micro- and macrostructured materials, beyond simple latex beads. Most importantly, we want to stress the relevance of the concept of an effective thermal length, which cannot only be increased by constriction but may be even more strongly affected by additional pathways and detours.

Experimental Section

Details on the particle synthesis, binary colloidal self-assembly methods, and characterization methods, as wells as a detailed description on thermal transport characterization by laser flash analysis, molecular dynamics simulations, and finite element modeling can be found within the Supporting Information.

Supporting Information

Supporting Information is available from the Wiley Online Library or from the author.

Acknowledgements

We thank Ute Kuhn for help with DSC measurements. Tobias Lauster, Julian Sindram, and Dominik Skrybeck are acknowledged for performing firsts UV-Vis and LFA experiments. Bernd Kopera is acknowledged for providing the interface between MD and FEM simulation. Additional support was provided by the SFB840. This work was funded by the Volkswagen foundation through a Lichtenberg professorship.

References

[1] B. Poudel, Q. Hao, Y. Ma, Y. Lan, A. Minnich, B. Yu, X. Yan, D. Wang, A. Muto, D. Vashaee, X. Chen, J. Liu, M. S. Dresselhaus, G. Chen, Z. Ren, Science 2008, 320, 634.

[2] D. G. Cahill, P. V. Braun, G. Chen, D. R. Clarke, S. H. Fan, K. E. Goodson, P. Keblinski, W. P. King, G. D. Mahan, A. Majumdar, H. J. Maris, S. R. Phillpot, E. Pop, L. Shi, Appl. Phys. Rev. 2014, 1, 45.

[3] D. G. Cahill, W. K. Ford, K. E. Goodson, G. D. Mahan, A. Majumdar, H. J. Maris, R. Merlin, Phillpot, S. R., J. Appl. Phys. 2003, 93, 793.

[4] D. G. Cahill, R. O. Pohl, Annu. Rev. Phys. Chem. 1988, 39, 93.

[5] M. Maldovan, Nature 2013, 503, 209.

[6] A. Einstein, Ann. Phys. (Berlin) 1911, 340, 679.

[7] D. G. Cahill, S. K. Watson, R. O. Pohl, Phys. Rev. B 1992, 46, 6131.

[8] P. B. Allen, J. L. Feldman, Phys. Rev. B 1993, 48, 12581.

[9] P. B. Allen, J. L. Feldman, J. Fabian, F. Wooten, Philos. Mag. B 1999, 79, 1715.

[10] C. Chiritescu, D. G. Cahill, N. Nguyen, D. Johnson, A. Bodapati, P. Keblinski, P. Zschack, Science 2007, 315, 351.

[11] M. D. Losego, I. P. Blitz, R. A. Vaia, D. G. Cahill, P. V. Braun, Nano Lett. 2013, 13, 2215.

[12] J. Moon, A. J. Minnich, RSC Advances 2016, 6, 105154.

[13] H. Mizuno, S. Mossa, J. L. Barrat, Sci. Rep. 2015, 5, 14116.

[14] H. Zhang, A. J. Minnich, Sci. Rep. 2015, 5, 8995.

[15] W. Kim, J. Zide, A. Gossard, D. Klenov, S. Stemmer, A. Shakouri, A. Majumdar, Phys. Rev. Lett. 2006, 96, 045901.

[16] B. Notario, J. Pinto, E. Solorzano, J. A. de Saja, M. Dumon, M. A. Rodríguez-Pérez, Polymer 2015, 56, 57.

[17] M. Koebel, A. Rigacci, P. Achard, J. Sol-Gel Sci. Technol. 2012, 63, 315.

[18] X. Lu, M. C. Arduini-Schuster, J. Kuhn, O. Nilsson, J. Fricke, R. W. Pekala, Science 1992, 255, 971.

[19] S. N. Schiffres, K. H. Kim, L. Hu, A. J. H. McGaughey, M. F. Islam, J. A. Malen, Adv. Funct. Mater. 2012, 22, 5251.

[20] Z. Chen, P. C. Hsu, J. Lopez, Y. Z. Li, J. W. F. To, N. Liu, C. Wang, S. C. Andrews, J. Liu, Y. Cui, Z. N. Bao, Nat. Energy 2016, 1, 15009.

[21] C. Sangrós, C. Schilde, A. Kwade, Energy Technol. 2016, 4, 1611.

[22] C. Masarapu, H. F. Zeng, K. H. Hung, B. Wei, ACS Nano 2009, 3, 2199.

[23] F. A. Nutz, M. Retsch, Phys. Chem. Chem. Phys. 2017, 19, 16124.

[24] F. A. Nutz, P. Ruckdeschel, M. Retsch, J. Colloid. Interf. Sci. 2015, 457, 96.

[25] P. Ruckdeschel, T. W. Kemnitzer, F. A. Nutz, J. Senker, M. Retsch, Nanoscale 2015, 7, 10059.

[26] T. Still, W. Cheng, M. Retsch, R. Sainidou, J. Wang, U. Jonas, N. Stefanou, G. Fytas, Phys. Rev. Lett. 2008, 100, 194301.

[27] J. W. Goodwin, J. Hearn, C. C. Ho, R. H. Ottewill, Colloid. Polym. Sci. 1974, 252, 464.

[28] R. H. Ottewill, J. N. Shaw, Kolloid Z. Z. Polym. 1967, 215, 161.

[29] N. Vogel, M. Retsch, C. A. Fustin, A. Del Campo, U. Jonas, Chem. Rev. 2015, 115, 6265.

[30] P. N. Pusey, W. van Megen, Nature 1986, 320, 340.

[31] M. Dijkstra, R. van Roij, R. Evans, Phys. Rev. Lett. 1998, 81, 2268.

[32] A. V. A. Kumar, J. Chem: Phys: 2013, 138, 154903.

[33] J. Wang, S. Ahl, Q. Li, M. Kreiter, T. Neumann, K. Burkert, W. Knoll, U. Jonas, J. Mater. Chem. 2008, 18, 981.

Supporting Information

Constricted Thermal Conductivity through Dense Particle Packings with Optimum Disorder

Fabian A. Nutz, Alexandra Philipp, Martin Dulle, Markus Retsch*

Experimental Section

Materials:

Potassium persulfate (KPS, ≥ 99 % Aldrich), styrene (≥ 99 %, Aldrich) and acrylic acid (99 %, AA, Aldrich) were used as received. Water was taken from a Millipore Direct Q3UV unit for the entire synthesis and purification steps.

Particle Synthesis: In a typical synthesis, a 500 mL three neck flask was charged with 245 mL milliQ water and 30 mL of styrene. The mixture was heat to 75 °C at a stirring speed of 650 rpm and allowed to equilibrate under a slight argon flow for ~15 min. Subsequently, 3 mL of acrylic acid were added, and the mixture was allowed to further equilibrate for ~10 min. To initiate the polymerization, 100 mg KPS, dissolved in 5 mL milliQ water were rapidly added to the mixture. The polymerization was carried out overnight under a slight argon flow. To adjust the size of the particles the amount of acrylic acid has been varied.[1, 2] The reaction was stop by exposing the mixture to ambient atmosphere. The particles were purified by dialysis against milliQ water for five days, changing water twice a day.

Binary colloidal self-assembly: Binary colloidal assemblies were fabricated by evaporation induced self-assembly of a given amount of prior mixed binary particle dispersions in a PTFE beaker. The obtained monoliths generally possess a diameter of ~20 mm and a thickness of several hundred micrometers.

Dip-coating: Samples for UV-vis measurements were prepared on glass slides by dip-coating 3 wt% of binary particle solutions. The glass slides were purified with

Hellmanex solution an ethanol prior to use. Furthermore, the dip-coating process the glass slides were treated with oxygen plasma to ensure a constant wetting of the particle solutions.

Methods:

Dynamic light scattering: Dynamic light scattering measurements were performed on aqueous particle dispersion at a Malvern Zetasizer with 175° backscattering geometry to determine the hydrodynamic diameter of the particles and their size distribution

Light microscopy: Bright field light microscopy side view images of the edges of split of the colloidal assemblies were recorded on a Carl Zeiss Axio Imager.A2m light microscope equipped with an AxioCam Icc 1 camera to get a qualitative impression about the long range ordering of the colloidal particles.

Scanning electron microscopy: To determine the hard sphere diameter of the particles, Scanning electron microscopy (SEM) was performed on a Zeiss Leo 1530 electron microscope. Therefore, dilute particle dispersions were drop-casted on a silicon wafer and sputtered with 1.3 nm platinum. Furthermore, SEM side-view images of the edges of split of the colloidal monoliths were obtained to gain an impression of the order within the interior of the monoliths. Fast Fourier transformation was applied on the recorded images using the FFT function, implemented in the software ImageJ 146.r.

Differential scanning calorimetry: Heat capacity determination was carried out according to ASTM E1269 on a TA Instruments Q1000 differential scanning calorimeter under a nitrogen flow of 50 mLmin^{-1} at a heating rate of 20 Kmin^{-1}. Two heating cycles were conducted between -40 °C and 200 °C. The specific heat capacity was evaluated from the second heating cycle. The mean value from all polystyrene particles under investigation has been used for evaluation (Figure S1).

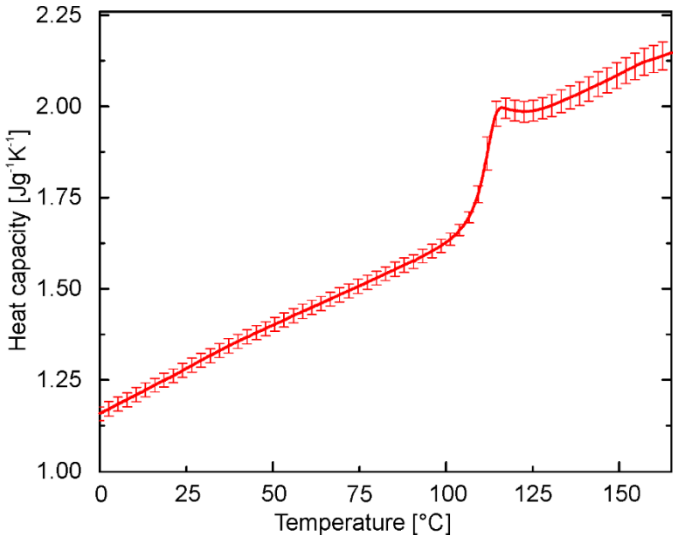

Figure S1. Mean specific heat capacity of the various polystyrene binary assemblies. Error arise from measuring every assembly.

Density determination: The density of the colloidal assemblies was determined by the volume and mass of the samples. The volume was obtained from a Keyence V3100 3D digital macroscope.

Laser flash analysis: Laser flash analysis was performed on a Linseis XFA 500 XenonFlash apparatus equipped with an InSb infrared detector to obtain the thermal diffusivity of the colloidal assemblies. The thickness of the samples were determined on a Mitotoyo Litematic VL 50. Prior to the measurement, the bottom and top side of the samples were coated with a thin layer of black air brush color serving as a blocking layer. Furthermore, the samples were coated with a thin graphite layer (< 15 µm). This enables a good absorbance at the bottom, and high emissivity at the top side of the monoliths. Measurements were performed on at least three individual samples. Experiments were conducted in vacuum atmosphere at a pressure of ~5x10^{-2} mbar to exclude any influence of the ambient atmosphere. The raw data was fitted with the radiation fit model provided by the software Aprosoft Laser Flash Evaluation v.1.06. Measurements were performed on at least three samples.

A xenon lamp emits a light pulse onto the sample. The thermal energy of the light pulse is absorbed at the bottom graphite layer and travels through the specimen.

The thermal energy is then emitted from the top side. This temperature rise is recorded in dependence of the elapsed time since the light pulse by a fast mid-infrared detector. A numerical fitting procedure provided by the commercial software package Aprosoft Laser Flash Evaluation v1.06 based on the one-dimensional temperature diffusion equation was used to determine the thermal diffusivity α.[5] For this, accurate knowledge of the sample thickness is a prerequisite, as the thickness strongly influences half-rise time as given by:

$$\alpha(T) = \frac{1.38 \cdot d^2}{\pi^2 t_{\frac{1}{2}}} \tag{S1}$$

$t_{1/2}$ represents the time needed for the half maximum temperature rise at the top surface.[6] The thermal conductivity κ of the sample is calculated by

$$\kappa(T) = \alpha(T) \cdot c_p(T) \cdot \rho(T) \tag{S2}$$

with the specific heat capacity c_p and the density ϱ.

Molecular dynamics (MD) simulations

All dense colloidal assemblies used in the finite element modeling were obtained using LAMMPS.[3] Visualization was done with Ovito[4] Every simulation consisted of 10000 arbitrarily placed spheres of the desired size and number ratio. The simulation box had periodic boundaries and was elongated in the z-direction at the start. This was done to mimic the evaporation of solvent for the real-world system. Using the NPT barostat we compressed the box first along the z-axis up to a pressure where all axes had a comparable length. After that the box was compressed isometrically to a pressure at which no more compression without overlap of the spheres was possible. We used the colloidal Yukawa potential included in the LAMMPS code with a short range repulsive part.

The analysis of the resulting dense colloidal assemblies was done with a self-written software using C++. The software calculates the radial distribution function (G(r)) for the given set of coordinates and uses the first three peaks to determine the three possible next neighbor distances as well as the next neighbor distance cut off. According to this cut off it counts the neighbors of each individual particle and identifies it as a small or big sphere and therefore enabled us to obtain very detailed information on the local structure around each particle. It also calculates the density as well as the average number of neighbors.

Finite element modeling: Heat transport through colloidal assemblies was simulated using the finite element modeling (FEM) software COMSOL Multiphysics®. For this, the crystalline (0 and 100 % large particles) and amorphous particle structures (size ratios: 0.54, 0.8, and 0.9) obtained from the MD simulations were used. The particle size has been adjusted such that the contact areas between adjacent spheres are comparable to the experimental values. All particles were fused into one object and, thus no thermal resistance between the particles was considered. Due to the limited physical memory (128 GB), the system size has been reduced to a feasible size. Therefore, three cubes with around 100 particles were cut out of each investigated colloidal assemblies. The mesh size was as chosen to ensure mesh size independent results (see Figure S5c). A temperature difference was imposed to two opposite surfaces of the cubes. Since all remaining surfaces were kept thermally insulating, purely one-dimensional thermal transport is obtained. The simulation was conducted along all three directions of the cube (x, y, and z). Using Fourier's law (see Equation S4), the effective thermal conductivity of the assembly is calculated from the computed heat flux, normal to the isothermal faces. Figure S6 demonstrates that three cubes are sufficient to calculate a meaningful average value. Furthermore, heat flux streamlines have been plotted to visualize the heat path length through the different colloidal assemblies. The length of the streamlines (L_{SL}) has been normalized by the total length of the cube (L_C) to calculate the relative streamline length (L_{SL}/L_C in %).

Assembly structures from MD simulation

We chose the colloidal Yukawa potential in LAMMPS[7] because it treats the spheres as impenetrable bodies with a fixed radius which prevents unwanted overlap even at very high pressures. The Yukawa potential was necessary in order to facilitate the formation of the *fcc* phases at the edges of the phase diagram and the real particles also carry a negative net charge. The pairwise interaction is calculated using the formula:

$$E = \frac{A}{\kappa} e^{-\kappa\left(r-(r_i+r_j)\right)}; \quad r < r_c \tag{S3}$$

With κ being the screening length (inverse distance units), r_i and r_j are the radii of the two interacting spheres. The prefactor A has to be specified for each pair type. It is determined from the relationship of the surface charge to surface potential in the presence of an electrolyte. In our case this prefactor is proportional to only the radius of each particle. All other parameter are the same.

We chose a large screening length of 50 which corresponds to 1/50 of the diameter of the large particles in order to hinder crystallization at higher interparticle distances and ensure good mixing of the differently sized particles. As the particles in the experiments are a few hundred nanometers in size this large screening length also approximates the charge interaction distance relative to the particle size. An example of the interaction parameters is given in Table S1.

Table S1. MD simulation interaction parameters for the size ratio 0.54.

Pair style	Screening length	Interaction cutoff (r_c)	A for 1:1	A for 1:2	A for 2:2
Yukawa/colloid	50	1.5	10000	7500	5000

Comparison between MD simulation and experimental colloidal glass fabrication

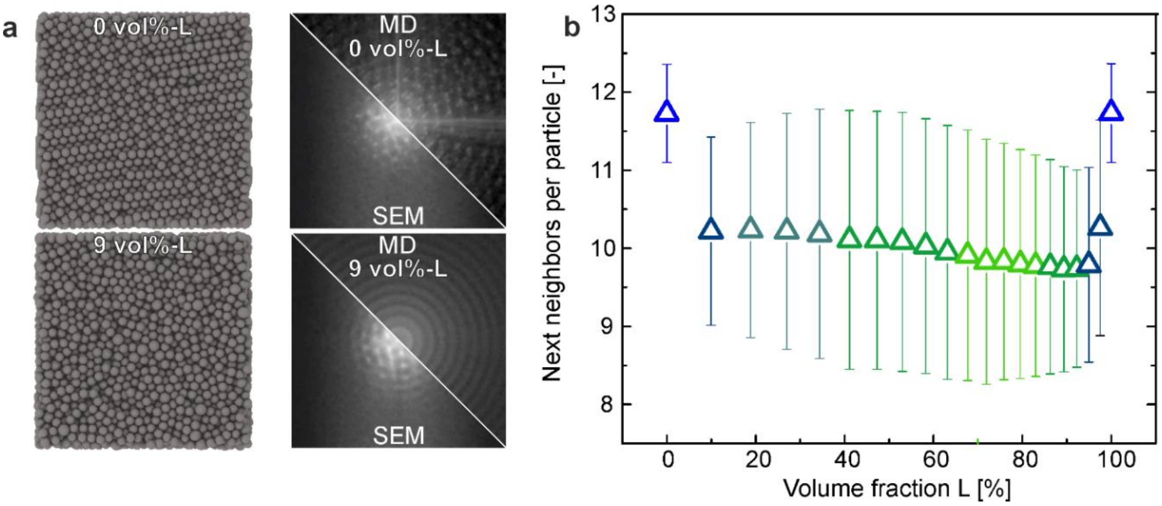

Figure S2. Side views received from MD simulations and number of next neighbors per particles. (a, left) typically obtained particle assemblies from MD studies; (a, right) FFT comparison between experiment and simulation. (b) Average next neighbors per particle vs. volume fraction of large particles. Color code indicates order (blueish) and disordered (greenish) assemblies.

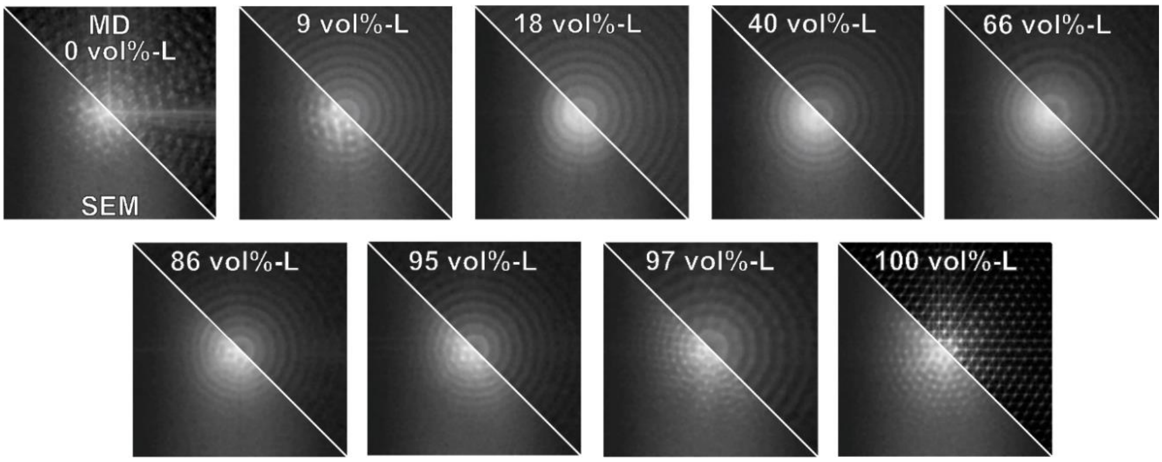

Figure S3. FFT comparison between the particle structures received from MD simulations and SEM side view images. Particularly at low and high mixing ratios a partial crystallinity can be inferred from the experimental SEM images. It indicates an easier colloidal glass formation in the MD simulation compared to the experimental conditions.

Influence of mixing ratio on next neighbor distribution function of size ratio 0.54

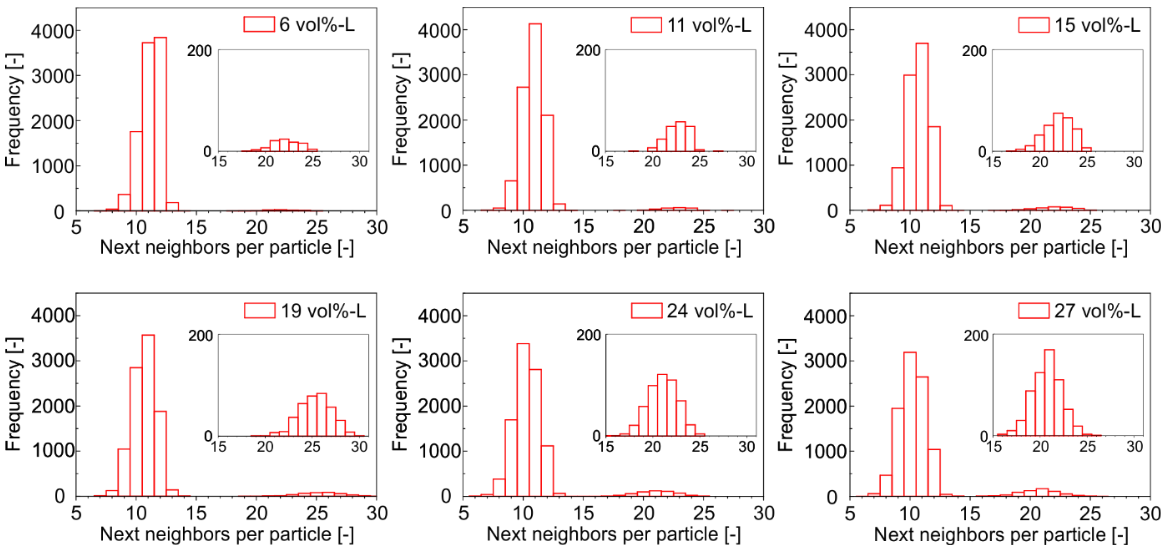

Figure S4. Histograms of the next neigbors per particle for a size ratio of 0.54. Various particle volume ratios close to the minimum thermal conductivity (19 vol%-L) are compared. All assemblies have the same average number of next neigbors (~10-11), but only the assembly with 19 vol%-L shows a second fraction with the highest number of next neighbors (20-30). Thus, this assembly is expected to have the lowest thermal conductivity.

Finite element modeling

Fourier's law is used to calculate the effective thermal conductivity κ_{eff}:

$$\kappa_{eff} = \frac{Q/A}{\Delta T/h} \tag{S4}$$

Q is the heat flow rate normal to the cross-sectional area A of the cube, ΔT the temperature difference, and h the cube length.

Table S2. Specific heat capacity, density, and thermal conductivity of polystyrene used in FEM simulations.

Specific heat capacity **[$Jg^{-1}K^{-1}$]**	**Density** ***[gcm^{-3}]***	**Thermal conductivity** ***[$mWm^{-1}K^{-1}$]***
1.25	1.05	150

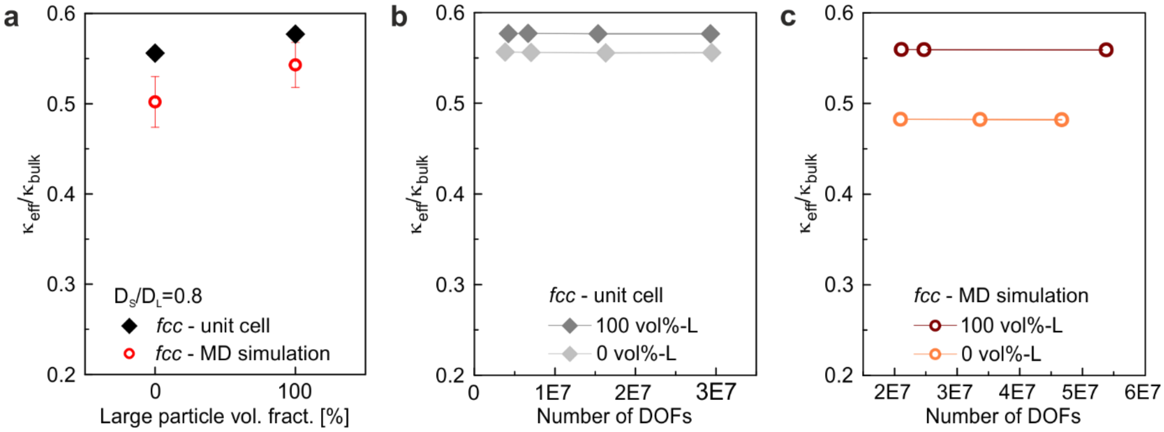

Figure S5. (a) Comparison of the effective thermal conductivity divided by the bulk thermal conductivity of polystyrene obtained for an ideal *fcc* unit cell and the *fcc* structure from MD simulation. The average particle contact area of the *fcc* structure from MD simulation was used to create the unit cell. The slight reduction of the MD simulation compared to the ideal unit cell originates from line and point defects, which are not present in the ideal case. (b, c) The effective thermal conductivity is independent of the number of DOFs and, thus of the mesh size. (c) The data are exemplarily plotted for one position in the *fcc* structure from MD simulation, respectively.

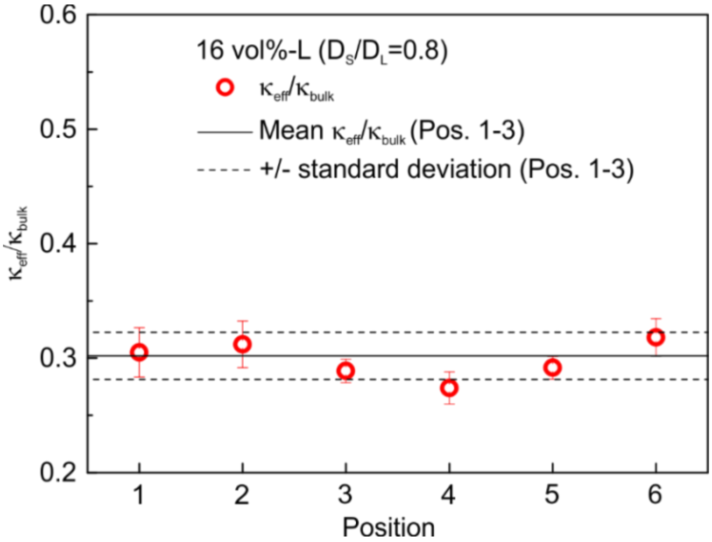

Figure S6. Effective thermal conductivity of the particle assembly with 16 vol% large particles (size ratio 0.8) obtained for six cubes cut out of different positions of the amorphous particle structure (red circles). The error bars arise from the three different simulation directions per cube (x, y, and z). The black solid line represents the mean effective thermal conductivity calculated from the first three values, the dashed line is the corresponding standard deviation. This plot shows that three positions are sufficient to calculate a meaningful average value.

References

[1] J. W. Goodwin, J. Hearn, C. C. Ho, R. H. Ottewill, Colloid. Polym. Sci. 1974, 252, 464.

[2] R. H. Ottewill, J. N. Shaw, Kolloid Z. Z. Polym. 1967, 215, 161.

[3] S. Plimpton, J. Comput. Phys. 1995, 117, 1.

[4] S. Alexander, Modell. Simul. Mater. Sci. Eng. 2010, 18, 015012.

[5] L. Dusza, High Temp. - High Press. 1995, 27, 467.

[6] W. J. Parker, R. J. Jenkins, C. P. Butler, G. L. Abbott, J. Appl. Phys. 1961, 32, 1679.

[7] S. Samueal A, Statistical Thermodynamics of Surfaces, Interfaces, and Membranes, Westview Press, Virgina, US, 2003, 284.

5 Outlook

In summary, the thermal transport properties of polymer colloidal crystals and assemblies have been investigated. Taking advantage of the unique properties of this material class, it has been shown that this material class can either serve as a model system to study fundamental heat transport in a mesoscale system, or can be used a versatile platform to develop novel strategies for the specific design of thermally functional particulate matter. Still, there are some questions, which need to be addressed to get a comprehensive picture of the thermal transport properties of polymer colloidal assemblies. i) The influence of the diameter of the particles forming the assembly is still not clarified. ii) It is unclear how many particle layers are necessary to reach the observed strong insulation behavior of the material. Since the insulation behavior evolves from the colloidal structuring, insulation materials, possessing a strong insulation behavior at very low thicknesses may be achievable. iii) Although the temperature-dependent increase of the thermal conductivity has been exploited to precisely tailor the temperature-dependent increase of the thermal conductivity, this transition is yet irreversible. Spending effort into the right choice of the particle material, e.g. shape-memory compounds, semi-crystalline, cross-linked or stimuli-responsive polymers, may promise to overcome the irreversibility of the transition. Once this is achieved, the presented concepts can be transferred to the fabrication of thermal devices such as switching materials, diodes and rectifiers, made from a colloidally structured, solid-state material. Therefore, the presented results serve as a general basis, wherefrom it is possible to answer fundamental questions of thermal transport further, as well as to improve the development of thermally functional materials.

6 Eidesstattliche Versicherungen und Erklärungen

(§ 5 Nr. 4 PromO)

Hiermit erkläre ich, dass keine Tatsachen vorliegen, die mich nach den gesetzlichen Bestimmungen über die Führung akademischer Grade zur Führung eines Doktorgrades unwürdig erscheinen lassen.

(§ 8 S. 2 Nr. 5 PromO)

Hiermit erkläre ich mich damit einverstanden, dass die elektronische Fassung meiner Dissertation unter Wahrung meiner Urheberrechte und des Datenschutzes einer gesonderten Überprüfung hinsichtlich der eigenständigen Anfertigung der Dissertation unterzogen werden kann.

(§ 8 S. 2 Nr. 7 PromO)

Hiermit erkläre ich eidesstattlich, dass ich die Dissertation selbständig verfasst und keine anderen als die von mir angegebenen Quellen und Hilfsmittel benutzt habe.

(§ 8 S. 2 Nr. 8 PromO)

Ich habe die Dissertation nicht bereits zur Erlangung eines akademischen Grades anderweitig eingereicht und habe auch nicht bereits diese oder eine gleichartige Doktorprüfung endgültig nicht bestanden.

(§ 8 S. 2 Nr. 9 PromO)

Hiermit erkläre ich, dass ich keine Hilfe von gewerblichen Promotionsberatern bzw. -vermittlern in Anspruch genommen habe und auch künftig nicht nehmen werde.

……………………………………………………………..

Ort, Datum, Unterschrift